



MINISTRY OF HIGHER EDUCATION AND SCIENTIFIC
RESEARCH

MOULOUD MAMMERI UNIVERSITY OF TIZI OUZOU

LMD DOCTORAL THESIS

Faculty of Sciences
Physics Department
Specialty: Matter and radiation

Presented by

Mrs. BEN MAMMAR-NABET Rima

Theme

Modification of titanium dioxide nanotubes for environmental and energy applications

In front of the examination jury composed of:

M. Mezeghrane Abdelaziz	Professor	UMMTO	President
Mrs. Hamadou Lamia	Professor	UMMTO	Supervisor
Mrs. Benbrahim Nassima	Professor	UMMTO	Examiner
M. Elkeurti Mohammed	Professor	University of Saida	Examiner
M. Zemouli Mostefa	MCA	University of Saida	Examiner

Defended on, 25/06/2023

ACKNOWLEDGMENT

First and foremost, I would like to praise and thank God, the Almighty, for His showers of blessings throughout my research work, so that I have been finally able to accomplish the thesis successfully.

I would like to show my greatest appreciation to **Mrs. Hamadou-Mezeghrane Lamia**, Prof at UMMTO as the thesis supervisor. I can't thank her enough for her tremendous support, availability and help during these four years of hard work. She always gave me countless opportunities to grow as a researcher and as a good person. I have learned so much from her in both scientific and personal aspects. Without her relevant ideas, hard work, encouragement and guidance this thesis would not have materialized.

I am grateful to all the team members of the Laboratory of Physics and Chemistry of Materials (LPCM), **M. Adkhis Ahmed**, **M. Kadri Abdelaziz**, **Mrs. Benbrahim Nassima**, **Mrs. Melil Baya** and **Mrs. Djouder Lynda** for welcoming and giving me the opportunity to conduct my doctoral research and for all of the resources and support they have provided me.

I would like to extend a special thanks to **M. Boudinar Salem**, (LPCM) director, who went above and beyond to help me with my work, he supported, advised me and found always time to run my samples pass to the SEM. Thank you so much for the pieces of advice that you've always given me.

I am extending my thanks to **M. Merzouk Tahar**, (LPCM) engineer, for his human and professional qualities. He was always ready to help me with an open heart. I thank you a lot for every smiley morning that you've given me.

An enormous appreciation is addressed to jury members who agreed to examine this work: **M. Mezeghrane Abdelaziz**, prof at UMMTO, as the president of the jury. **Mms Ben brahim Nassima**, Prof at UMMTO, **M. Elkeurti Mohammed**, prof at Dr Moulay Taher University of Saida and **M. Zemouli Mostefa**, MCA at Dr Moulay Taher University of Saida, as examiners of this work.

I also address my thanks to **M. Saifi Amirouche** for his help. Thank you so much.

I would also like to thank my colleagues at LPCM: **Rekeb Lydia**, **Idiri Naima**, **Boumati Ryma**, **Madjour Karim**, **Kellou Hamza**, **Lakrouf Islam** for their support during my

research. In particular, I would like to thank my best friend **Outayeb Sonia** for her help, support and for the best moments we spent together. She always found a way to make me happy in my difficult times. Thank you so much to be such a good friend.

I would like to extend my sincere gratitude to my parents in law for their encouragement and support.

I deeply thank my parents, for their unconditional trust, timely encouragement, and endless patience. It was their love that raised me up again when I got weary. I am truly thankful and honored to have you as my parents.

All my gratitude and love to my whole family, Grand-mother, my brothers **Mourad, Bilal**, my sisters **Farida, Noria** and my sister in law **Chafika** for their encouragement.

Thanks to my lovely daughter **Dina**, for being an infinity source of happiness and motivation. Looking at you, growing up every day is the most amazing gift that I have received in my life. Finally, I would like to express my eternal gratitude to my gorgeous, husband **Aziz**. He is the most important part of this accomplishment, with his tireless encouragement, company, and love.

Finally, my thanks go to all the people who have supported me to complete this research work directly or indirectly.

To my dear father and mother

To my loving husband Aziz

To my awesome baby girl Dina

List of publications

Publication in journals

R. Ben Mammam, S. Boudinar, A. Kadri, & L. Hamadou, TiO₂ Nanotubes Synthesis with Dominant {001} Exposed Facets for Efficient Photocatalytic and Photoelectrochemical Water Oxidation Applications, *Journal of The Electrochemical Society*, 168(2021)106501.

R. Ben Mammam, L. Hamadou, S. Boudinar, A. Kadri, Promising Supercapacitive and Photocatalytic Performances of TiO₂ Nanotubes Loaded with Graphene: Insight on the Quantitative Characterisation by EIS. *Journal of The Electrochemical Society*, 169(2022)113503.

R. Ben Mammam, S. Boudinar, L. Hamadou, Mesoporous graphene-based hybrid nanostructures for capacitive energy storage and photocatalytic applications. *Fullerenes, Nanotubes and Carbon Nanostructures*, 31(2023)266-276.

R. Ben Mammam, L. Hamadou, Highly broadband plasmonic modified α -Fe₂O₃/TiO₂ nanotubes for efficient photoelectrochemical water splitting, *Optical materials* (under review).

International conferences

R. Ben Mammam, L. Hamadou (Palladium Doped TiO₂ nanotubes for efficient photocatalytic and photoelectrochemical water splitting applications), DZPOWER 21 international conference 'power and energy engineering' (2021)

R. Ben Mammam, L. Hamadou (Synthesis of Pt/ α -Fe₂O₃/TiNT heterostructure for enhanced photoelectrochemical water splitting and photocatalytic applications), 1st International Conference: Renewable Materials and Energies (IC-RME 2022).

R. Ben Mammam, L. Hamadou (Electrodeposition of Palladium nanoparticles on TiO₂ nanotubes for efficient photocatalytic and photoelectrochemical water oxidation performances), International conference on energy and material sciences (EMS 2022).

R. Ben Mammam, L. Hamadou (TiO₂-Nanotube Formation by Two-Step Anodization for Efficient Photocatalytic application), 4th International Conference on Applied Engineering and Natural Sciences (ICAENS 2022-FREE).

National conferences

R. Ben Mammam, L. Hamadou (Modification of intrinsic properties of TiO₂ nanotubes for hydrogen production) Conference: The first National seminar on green hydrogen for the algerian industrial sector (SNHR-IA'2022).

R. Ben Mammam, L. Hamadou (TiO₂ nanotubes hybridized with graphene for energy storage and photocatalytic applications) Conference: the 1st national symposium of the Algerian Academy of Sciences and Technologies on nanotechnology (2022).

Abbreviations

CB	Conduction Band
CPE	Constant Phase Element
CV	Cyclic Voltammetry
DI	Deionized
DOS	Densities Of States
DRS	Diffuse Reflectance Spectroscopy
EDLC	Electronic Double Layer Capacitor
EDS	Energy-dispersive spectroscopy
EIS	Electrochemical Impedance Spectroscopy
ESR	Equivalent Series Resistances
FTIR	Fourier Transform Infrared Spectrometer
GCD	Galvanostatic Charge-Discharge
LSV	Linear Sweep Voltammetry
LSPR	Localized Surface Plasmons Resonance
MB	Methylene Blue
M-S	Mott-Schottky
NPs	Nanoparticles
OCP	Open Circuit Potential
PC	Photocatalytic
PEC	Photoelectrochemical
PL	Photoluminescence
Pt	Platinum
RHE	Reversible Hydrogen Electrode
SC	Semiconductor
SEM	Scanning Electron Microscopy
SCR	Space Charge Region
SPR	Surface Plasmons Resonance
TiNT	TiO ₂ nanotubes
UV	Ultraviolet
VB	Valence Band
XRD	X-Ray Diffraction

List of Symbols

ϵ	Oxide permittivity
ϵ_0	Vacuum permittivity: 8.85×10^{-12} (en F m ⁻¹)
ϵ_m	Molar extinction
θ_B	Bragg angle
A	Absorbance
Ag/AgCl	Silver chloride electrode ($E^0 = 0.223$ V/ENH at 25 C°)
c	Solution concentration
C_{dl}	Double layer capacitance
C_H	Helmholtz layer capacitance
C_{GC}	Diffuse charge layer capacitance
C_{ss}	Gap states capacitance
C_s	Specific capacitance
C_{SC}	Semiconductor capacitance
e^-	Electron
E	Energy density y (mWh cm ⁻²)
E_c	Conduction band energy
E_F	Fermi level energy
E_g	Band gap energy
E_v	Valence band energy
f	Frequency (Hz)
h^+	Hole
h ν	Photon energy
I_{ph}	Photocurrent (A)
I_0	Incident light intensity
j_{ph}	Photocurrent Density (A cm ⁻²)
l	Optical path length
N_D	Donor density
Nq	Charge density
P	Power density (mWh cm ⁻²)
q	Electron Charge
R_{ct}	Charge transfer resistance
R_s	Solution resistance
U_{FB}	Flatband energy
U	Potential (V)
U_{ph}	Photopotential (V)
Z	Impedance

Table of cotenants

Abbreviations	I
List of symbols.....	II
Introduction.....	1
1. Motivation	2
2. Framework and objective of the thesis.....	3
3. Thesis organization.....	4
References	5

CHAPTER I: Literature and theoretical background

Introduction.....	7
I.1 Properties of TiO ₂ material.....	7
I.1.1 Crystallographic structure.....	7
I.1.2 Electronic structure and optical properties.....	9
I.1.3 Semiconductor (SC) properties.....	10
I.1.3.1 Dark behaviour of the n-type SC/Electrolyte interface.....	10
I.1.3.2 n-type SC/Electrolyte interface under polarization.....	11
I.1.3.3 n-type SC/Electrolyte interface under illumination.....	12
I.2 TiO ₂ material nanostructures.....	13
I.2.1 Drawbacks of TiO ₂ nanostructures.....	13
I.2.2 Improvement of TiNT performance.....	14
I.2.2.1 Cristal facets engineering	15
I.2.2.2 Band gap engineering	15
I.2.2.3 Surface sensitization by plasmonic materials.....	18
I.3 Applications of TiO ₂ nanostructures.....	20
I.3.1 Heterogeneous photocatalysis (Water traitement/depollution).....	21
I.3.2 Photoelectrochemical (PEC) water splitting.....	22
I.3.3 Electrochemical energy storage	23
I.3.3.1 Supercapacitors.....	24
I.3.3.1.1 Type of supercapacitors.....	25
I.3.3.1.2 Electrical Double Layer Capacitors.....	26
I.3.3.1.3 Pseudocapacitors.....	27
I.3.3.1.4 Hybrid supercapacitors.....	28

Conclusion.....	29
References.....	30

CHAPTER II: Materials, equipments and methods

Introduction.....	34
II.1 Fabrication of TiNT.....	34
II.1.1 Growth process of TiNT.....	35
II.2 Characterization methods.....	36
II.2.1 Physical and structural characterization.....	36
II.2.1.1 scanning electron microscopy.....	36
II.2.1.2 X-rays diffraction (XRD).....	37
II.2.1.3 Fourier transform infrared spectrometer.....	38
II.2.1.4 Photoluminescence spectroscopy.....	39
II.2.1.5 UV-Visible spectroscopy and diffuse reflectance spectroscopy.....	40
II.2.2 Electrochemical techniques.....	41
II.2.2.1 Cyclic voltammetry.....	41
II.2.2.2 Chronoamperometry.....	42
II.2.2.3 Linear sweep voltammetry.....	43
II.2.2.4 Electrochemical impedance spectroscopy.....	44
II.2.2.5 Mott-Schottky analysis.....	45
II.3 Methods for supercapacitor evaluation.....	46
II.3.1 CV measurements.....	47
II.3.2 Galvanostatic charge-discharge (GCD) measurements.....	47
II.3.3 EIS measurements.....	49
II.4 Photoelectrochemical measurements.....	50
II.5 Photocatalytic tests.....	50
References.....	51

CHAPTER III: TiO₂ nanotubes synthesis with dominant {001} exposed facets for efficient photocatalytic and photoelectrochemical water oxidation applications

Introduction.....	54
III.1 Two-step anodization TiNT synthesis procedure.....	56
III.1 Morphological and structural analysis.....	57
III.2 Electronic characterization of the materials.....	60

III.3 Optical properties.....	65
III.3.1 Photoluminescence analysis.....	65
III.3.2 Optical bandgap analysis.....	68
III.4 Photoelectrochemical (PEC) measurements.....	69
III.5 Photocatalytic performance.....	73
Conclusion.....	75
References.....	76

CHAPTER IV: Promising supercapacitive and photocatalytic performances of TiO₂ nanotubes loaded with graphene

Introduction.....	80
IV.1 Graphite exfoliation.....	81
IV.2 Graphene/TiNT hybrid system synthesis.....	83
IV.3 Morphological and structural characterizations of Gr/TiNT.....	84
IV.4 Optical characterizations of Gr/TiNT systems.....	87
IV.5 Electrochemical performance of the electrodes for supercapacitor.....	89
IV.5.1 GCD investigation.....	90
IV.5.2 EIS investigation.....	92
IV.5.3 CV analysis.....	100
IV.6 Photocatalytic performance of the electrodes.....	103
Conclusion.....	106
References.....	107

CHAPTER V: Fabrication of α -Fe₂O₃/TiO₂, Pt/TiO₂ and Pt/ α -Fe₂O₃/TiO₂ nanotubes for efficient visible light photoelectrochemical water splitting

Introduction.....	111
V. 1 Synthesis of TiNT based heterojunctions.....	112
V.1.1 Synthesis of α -Fe ₂ O ₃ /TiNT heterostructure.....	112
V.1.2 Synthesis of Pt/TiNT and Pt/ α -Fe ₂ O ₃ /TiNT composites.....	113
V.2 Cyclic voltammetry and current-time transient analysis.....	114
V.3 Morphological and structural characterizations of the systems.....	117
V.4 Optical characterization of the systems.....	120
V.5 Electronic characterization of the composites.....	123
V.6 Photoelectrochemical measurements.....	125

Conclusion.....	134
References.....	135
General conclusion.....	138

Introduction

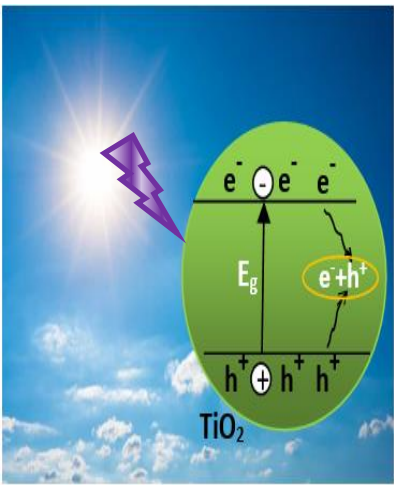


Global Energy needs



TiO₂ Advanced Applications

Drawbacks



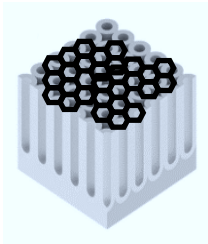
Remediations



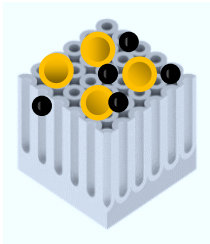
Orientation engineering



Heterojunction engineering



Gr/TiN



Pt/ α Fe₂O₃/TiN

Graphical abstract

1. Motivation

The increasing global energy demand and environmental pollution with the use of fossil fuels resources are the most significant issues facing humanity. Due to the depleting reserves of fossil fuels and increasing environmental pollution, producing more energy using renewable sources is absolutely required. Nowadays, suitable energy storage systems and green energy production are more relevant for environmental protection and fossil fuels replacement than ever. Developing a sustainable and clean energy carrier is a great technological challenge. At present, heterogeneous photocatalysis and photoelectrochemical (PEC) water splitting are considered as the most exciting and promising ways to directly harvest and convert renewable solar energy for generating sustainable green energy and eliminating organic pollutants. However, energy storage has been a serious concern due to the limitations of old-fashioned storage technologies. Devices known as electrochemical storage systems are capable of converting chemical energy into electricity and storing it. Electrochemical capacitors (supercapacitors), fuel cells and batteries could be other subcategories of electrochemical energy storage technologies [1].

Particular attention and considerable efforts have been undertaken in order to develop powerful materials suitable for sustainable applications. Due to their unique characteristics, such as large specific surface area, high chemical stability and relatively large surface area to volume ratio, one-dimensional nanotubular semiconductors promise to significantly improve the efficiency of a wide range of environmental and energy applications. Among the high quality nanotubular materials, titanium dioxide (TiO₂) nanotubes (TiNT) are one of the most attracting materials widely investigated in photocatalytic degradation of pollutants [2], PEC water splitting [3], supercapacitors [4] dye-sensitized solar cells [5], lithium-ion batteries [6] and so on.

However, two major factors limit the efficiency of their potential applications: (i) large band gap of 3.2 eV which makes them active only under UV light irradiation and (ii) fast recombination rate of photo-generated electron-hole pairs. To address these drawbacks, significant efforts have been performed to extend the absorption spectrum and to enhance the separation rate of the photogenerated electron-hole pairs, by modifying their chemical and band structure through doping or bandgap engineering. For this purpose, different approaches have been implemented and a variety of materials have been so introduced. Among these approaches, one can cite: facets surface engineering which consist in the modification of

intrinsic properties of the material [7], coupling with other narrower band gap semiconductors [8, 9], metallic or non-metallic doping [10], decorating with plasmonic nanoparticles [11] and so on.

2. Framework and objective of the thesis

The key objective of this thesis was to design and develop novel and effective strategies for modification of TiNT for energy production and storage applications. With this aim, orientation engineering and heterojunction engineering approaches were used. For the former, three materials have been selected: graphene (Gr), hematite (α -Fe₂O₃) and platinum (Pt).

The specific objectives are listed below:

- Synthesis of TiNT with dominant high energy {001} facets.
- Correlate crystallinity, preferential crystalline orientation, gap states characteristics (density and location) to the photoreactivity performance.
 - Synthesis of high-quality graphene (Gr), i.e. high electrical conductivity, low amount of oxygen-containing functional groups and free metallic and non-metallic impurities by electrochemical exfoliation of pure (P) graphite sheet and 5B pencil cores.
 - Synthesis of Gr/TiNT heterojunction by electrodeposition method.
 - Evaluate the effects of oxygen functional groups in accordance to the parameters derived from the electrochemical impedance spectra, with the aim of providing insight into the effects of oxygen functional groups in the energy storage process of Gt/TiNT system.
 - Evaluate the Gr/TiNT heterojunction performances for supercapacitive and photocatalytic applications.
- Prepare α -Fe₂O₃ particles with controllable size on TiNT by electrodeposition.
- Investigate the effect of α -Fe₂O₃ particle size on the optical and electronic properties of α -Fe₂O₃/TiNT system.
- Evaluate the α -Fe₂O₃/TiNT heterojunction performances for PEC water oxidation reaction.
 - Synthesis of controllable-size Pt particles on TiNT by electrodeposition.
 - Investigate the effect of Pt particle size on the optical and electronic properties of Pt/TiNT system.
 - Evaluate the Pt/TiNT heterojunction performances for PEC water splitting applications.

- Modify TiNT by both α -Fe₂O₃ and Pt nanoparticles, using two-step electrodeposition process, to form Pt/ α -Fe₂O₃/TiNT double-heterojunction for more visible light absorption and more efficient charge separation/transportation.

3. Thesis organization

This thesis is organized into five chapters:

Chapter one consists of a literature review and pertinent background information for this study. This includes a fundamental description of the TiO₂ properties, importantly crystallographic structure, optical and semiconducting ones. Details regarding one-dimensional TiO₂ nanotubes arrays reviewing their drawbacks and remediation are also presented. This chapter concludes by presenting the concept of the relevant applications employed in this work.

Chapter two is devoted to the presentation of the experimental techniques used in the present work for the synthesis and the characterization of the different composites. Particular focus is devoted to the description of the principles of electrodeposition and electrochemical impedance spectroscopy as well as electrochemical methods for evaluating a supercapacitor.

Chapter three investigates the fabrication of TiNT with dominant {001} exposed facets through two-step electrochemical anodization. Electronic properties, including gap states quantification (density and location) of TiNT were determined and correlated to their crystalline orientation. The separation efficiency of photogenerated electrons and holes were investigated using photoluminescence spectra, electrochemical impedance and onset photocurrents.

Chapter four consists of graphene modified TiNT. Modified TiNT were investigated for their supercapacitive and photocatalytic applications. The electrochemical capacitance performances of Gr/TiNT electrodes were examined mainly by EIS.

Chapter five presents the synthesis of α -Fe₂O₃/TiNT, Pt/TiNT and Pt/ α -Fe₂O₃/TiNT heterojunctions and their physico-chemical characterizations. PEC properties were evaluated for hydrogen production.

Finally, we end with a summary of the main findings of this study and suggest some promising future prospects for the continuity of this project.

References

- [1] Q. Dou, H. Park, *Energy & Environmental Materials*, 3(2020)286.
- [2] Y. R. Smith, A. Kar, *Industrial & Engineering Chemistry Research*, 48(2009)10268.
- [3] Z. Zhang, M. F. Hossain, T. Takahashi, *International journal of Hydrogen Energy*, 35(2010)8528.
- [4] B. Chen, J. Hou, K. Lu, *Langmuir*, 29(2013) 5911.
- [5] G. K. Mor, K. Shankar, M. Paulose, O. K.Varghese, C. A. Grimes, *Nano letters*, 6(2006)215.
- [6] J. Xu, C. Jia, B. Cao, W.F. Zhang, *Electrochimica acta*, 52(2007)8044.
- [7] L. Ainouche, L. Hamadou, A. Kadri, N. Benbrahim, D. Bradai, *Solar Energy Materials & Solar Cells*, 151(2016)179.
- [8] L. Rekeb, L. Hamadou, A. Kadri, N. Benbrahim, E. Chainet, *International Journal of Hydrogen Energy*, 44(2019)10541.
- [9] L. Rekeb, L. Hamadou, A. Kadri, N. Benbrahim, *Electrochimica Acta*, 256(2017)162.
- [10] M. M. Momeni, Y. Ghayeb, *Journal of the Electroanalytical Chemistry*, 751(2015)43.
- [11] A. P. Manuel, K. Shankar, *Nanomaterials*, 11(2021)1249.

Chapter I

Literature and theoretical background

Introduction

There is significant and growing interest in TiO₂ and its environmental and energetic applications. This chapter discusses in the first part the general properties of TiO₂, its limitations and gives some of modification methods for improving its electrochemical and photocatalytic performances. The second part introduces the three important applications explored in this thesis. We describe heterogeneous photocatalysis, photoelectrochemical water splitting (Hydrogen production) as well as energy storage in supercapacitors.

I.1 Properties of TiO₂ material

TiO₂ compounds have been extensively discussed in literature ever since Honda and Fujishima discovered titanium dioxide's capacity to function as a photocatalyst in 1972 [1]. TiO₂ with its unique properties, excellent stability, low cost, and excellent biocompatibility is an excellent choice for various applications such as dye sensitized solar cells, batteries, supercapacitors, photocatalysis, sensors and biomedical devices [2]. TiO₂ to be successfully applied in various fields, a fundamental comprehension of its structure and functions is necessary.

I.1.1 Crystallographic structure

TiO₂ is an n-type wide bandgap semiconductor, naturally exists in three common crystalline polymorphs: anatase (tetragonal), rutile (tetragonal) and brookite (orthorhombic), their structures are shown in [figure I.1](#). Both anatase and brookite are meta-stable; they are easily transformed into rutile at a temperature exceeding 450°C, rutile is the most thermodynamically stable [3]. The stability of different phases of TiO₂ depends on the size of the particles, with rutile being the most stable phase for particles larger than 35 nm. In contrast, anatase is the phase that is most stable for nanoparticles smaller than 11 nm and brookite is the best stable phase for nanoparticles with a size range of 11–35 nm. [4]. Besides, rutile is regarded to be more stable with predominant (110) surface, whereas anatase is more stable with (101) surface [5]. For application in charge separation devices, anatase phase is the preferred one due to its larger bandgap and higher conduction band edge [6].

The anatase is tetragonal crystal structure ($a = b = 3.78 \text{ \AA}$, $c = 9.50 \text{ \AA}$), it is described as Ti⁺⁴ ions surrounded by an octahedron of six linked O⁻² ions. The anatase crystals have a truncated pyramid shape with mostly {101} and {001} facets, their equilibrium shape through the Wulff construction is illustrated in [figure I.2](#).

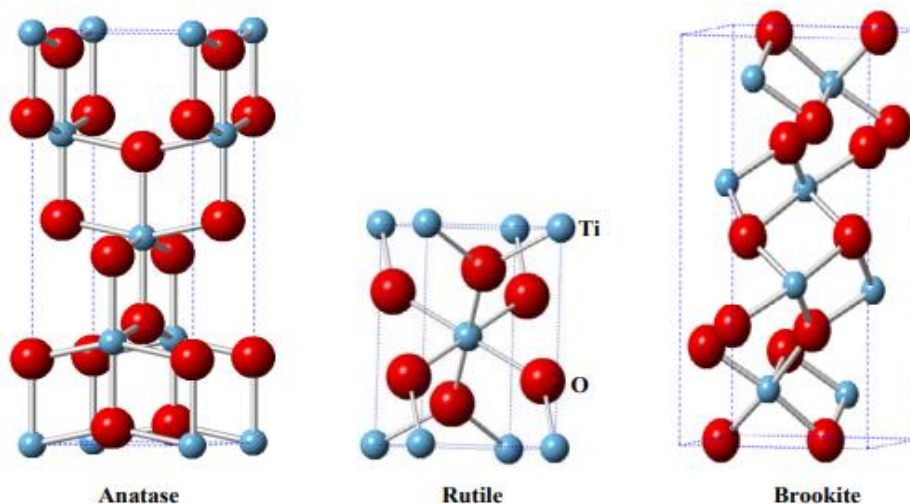


Figure I.1: Crystal structures of (a) anatase, (b) rutile and (c) brookite [7].

The surface energies of the $\{001\}$, $\{010\}$ and $\{101\}$ facets are 0.90 , 0.53 and 0.44 J m^{-2} respectively. The density of under coordinated Ti on each facet has a direct correlation with its surface energy. Only five-fold coordinated Ti (Ti-5c) atoms are present in $\{001\}$ and $\{010\}$ facets, whereas six-fold coordinated Ti (Ti-6c) and five-fold coordinated Ti (Ti-5c) atoms are present in $\{101\}$ facets. Higher-index facets have more complex shapes with more Ti atoms with different coordination numbers. Some properties of the particles like optical, magnetic, and chemical properties are strongly affected by the crystal shape [8] and the type of exposed crystal facets [9].

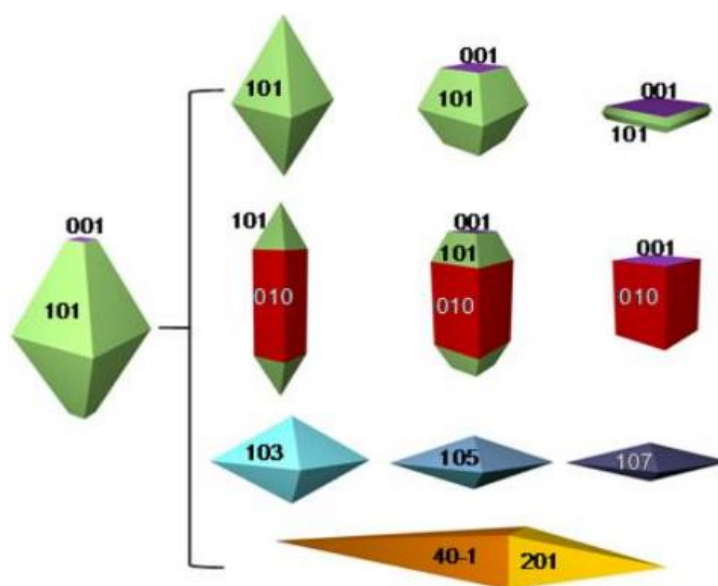


Figure I.2: Equilibrium crystal shape of anatase TiO_2 [10].

I.1.2 Electronic structure and optical properties

From energy view, electrons in crystalline semiconductors have specific energy levels and are prohibited to move around in other parts of the atom. The electronic band structures of the three TiO₂ modifications rutile, anatase and brookite are shown in figure I.3. (a). At absolute zero degree, the highest occupied and lowest unoccupied densities of states (DOSs) are the valence band (VB) and conduction band (CB) respectively, the VB describes a state of electrons tightly bound to the atomic nuclei and the CB reflects the electrons escaped from the materials to move entirely free in crystal lattice. Figure I.3. (b) presents the typical DOS spectra of the three polymorphs of TiO₂ that delineate the valence and conduction bands to be mainly comprised of O 2p and Ti 3d states, respectively.

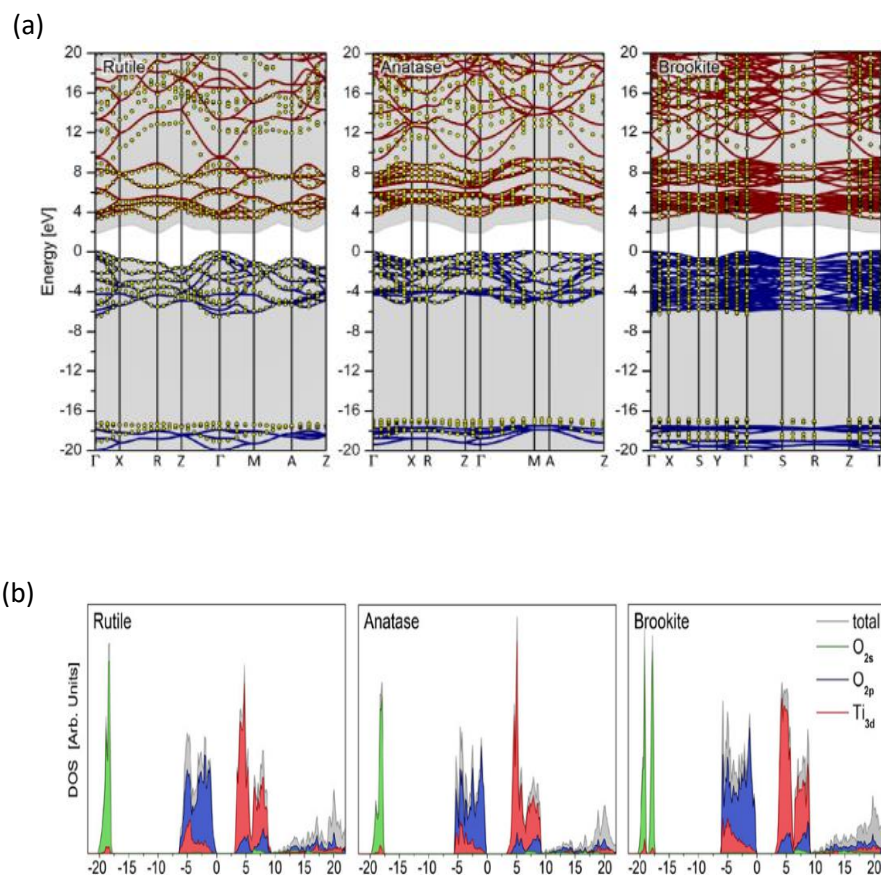


Figure I.3: (a) TiO₂ band structures for the rutile, anatase and brookite polymorphs and (b) Total and partial DOSs of the three polymorphs of TiO₂ [11].

Kapilashrami et al. [11] reported that both rutile and brookite TiO₂ have a direct band gap with $\Gamma \rightarrow \Gamma$ (CB \rightarrow VB) transitions, while anatase TiO₂ has an indirect band gap. The band gaps of TiO₂ phases are 3.0 eV for Rutile, 3.2 eV for anatase and 3.1 eV for brookite, which means that

TiO₂ can absorb photons with wavelength in UV region then electrons in the VB can be excited into CB. This energy separation between the two states defines its sensitivity/responsivity to the solar spectrum [12, 13].

I.1.3 Semiconducting properties

Three kinds of materials can be distinguished according to the energy distance between their valence bands and their conduction bands: insulators, semiconductors and metals. Most of the metal oxides are semiconductors. TiO₂ is an n-type semiconductor (SC), the n-type SC character is explained by the presence of oxygen vacancies, where the charge compensation of those anionic vacancies occurs by the presence of Ti⁺³ ions among the Ti⁺⁴ cations of the TiO₂ lattice [14].

I.1.3.1 Dark behavior of the n-type SC/Electrolyte interface

Given the SC nature of TiO₂, their electronic properties can be examined by capacitance measurements and photoelectrochemical methods. For this purpose, it is essential to investigate the interface between the n-type SC and the electrolyte before and after contacting each other. So, in the following description, only the interface between a n-type SC and electrolyte is considered.

Charge transfer from SC to electrolyte (or vice versa) may take place when the surface of the bulk SC remains in contact with an electrolyte. The electrons keep moving until equilibrium is attained, where the redox potential of the electrolyte equals the Fermi energy of the electrons in the solid. Assuming that there is no ion diffusion through the electrode/electrolyte junction, electrons are the only charges that can move across this interface in both directions. This type of electric transmission results in distinct charge distribution over the contact, known as the space charge layer. The space charge layer is created as a result of the energy band bending. The bending is due to the equilibrium alignment between the semiconductor Fermi level ($E_{F,SC}$) and the energy level of the electrolyte ($E_{F,redox}$). At the interface, a Helmholtz double layer followed by the diffuse Gouy–Chapman layer form due to accumulation of ions near the surface.

At least three forms of band bending might arise on the surface of the SC depending on the relative locations of the Fermi level of the SC and the electrochemical potential of the electrolyte:

(i) When the Fermi level of the SC is equal to the electrochemical potential of the electrolyte ($E_{F,SC} = E_{F,redox}$), no charge transfer would flow through the interface and there is no

excess charge on either side of the junction. This leads to a flat band (FB) condition of the SC (Figure I.4 (a)).

(ii) When $E_{F,SC} < E_{F,redox}$, the electrons accumulate at the SC side then the bands bend down and the accumulation layer is created (Figure I.4 (b)).

(ii) When $E_{F,SC} > E_{F,redox}$, the electrons deplete from the solid into the solution leaving behind a positive excess charge formed by immobile ionized donor states. A depletion layer is formed and the bands bend upward toward the surface (Figure I.4 (c)).

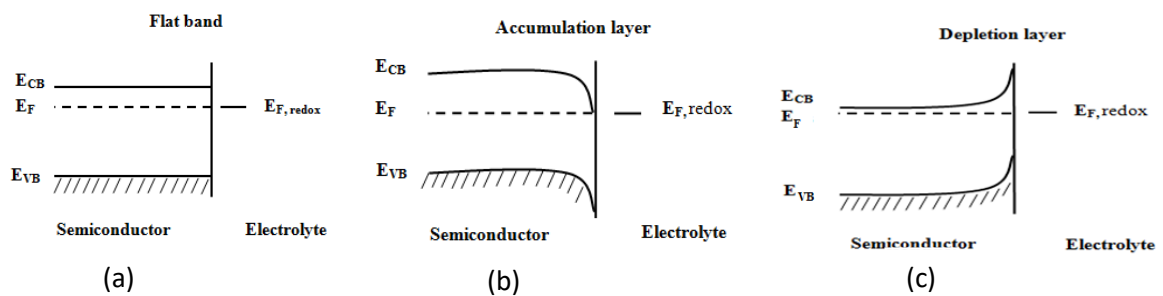


Figure I.4: Different equilibrium situations at the n-SC/Electrolyte interface.

I.1.3.2 n-type SC/Electrolyte interface under polarization

The applied potential gives information on the Fermi level (E_F) relative to the electrochemical potential of the electrolyte ($E_{F, redox}$) [15]. Such information is crucial because the relative difference between the two energy levels affects the degree of band bending: $\Delta E = (U_{FB} - U_{AppI})$ which in turn defines how easily charges can be separated.

When U_{appl} is equal to U_{FB} , this corresponds to the position of the Fermi level in the absence of space charge region (SCR) and thus of the electric field to separate the generated electron-hole pairs (Figure I.5 (a)).

Applying potential (U_{appl}) to the SC electrode changes the previously established equilibrium. For a positive bias, the band bending is upwards. The majority carriers (electrons) migrate towards the bulk, increasing the significance of its SCR which extends further into the bulk. Whereas, the holes diffuse through the interface with the electrolyte (region more depleted of majority charge carriers (Figure I.5 (b)).

Applying a potential more negative than U_{FB} will result in an accumulation of negative charges inside the SCR, modifying the direction of the band bending and the direction of the electric field (Figure I.5 (c)). Under this polarization condition, the n-type semiconductor is considered to be metalized.

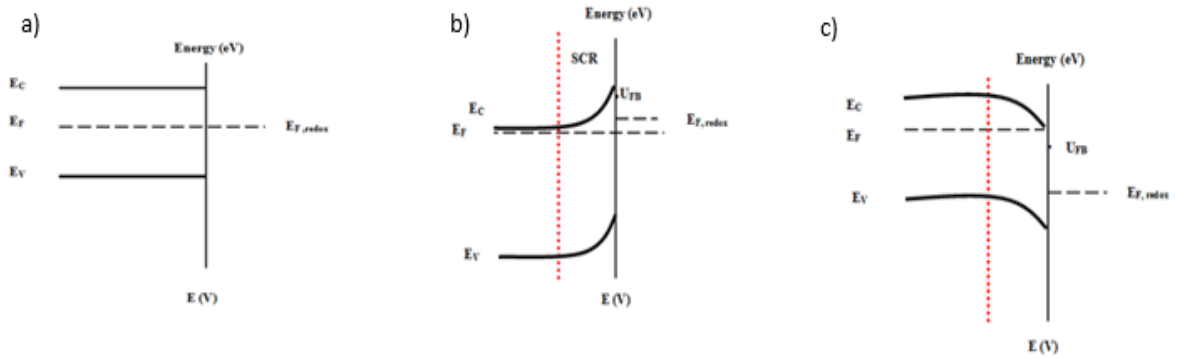


Figure I.5: n-SC/electrolyte interface behavior under voltage
a) $U_{\text{appl}} = U_{\text{FB}}$, b) $U_{\text{appl}} > U_{\text{FB}}$ and c) $U_{\text{appl}} < U_{\text{FB}}$.

I.1.3.3 n-type SC/Electrolyte interface under illumination

The absorption by a SC of photons of energy higher than the SC band gap energy (E_g) results in the generation of electron-hole pairs, the system is then out of equilibrium. The electrons are promoted from the valence band to the conduction band, yielding excess electrons in the CB and excess holes in the VB. The internal electric field within the SCR near the surface, creates an asymmetry within the system that allows the separation of photogenerated electrons and holes. The electric field associated with the band bending causes electrons to drift towards the bulk, whereas holes migrate to the surface of the SC leading to a decrease in the surface electric field. The band bending becomes less important because the electric field is weaker and the Fermi level of the electrons in the SC is modified (creating a quasi-Fermi level $[(E_F^*)_n, (E_F^*)_p]$). As a result, the potential within the SC evolves toward the flat band potential (Figure I.6 (b)).

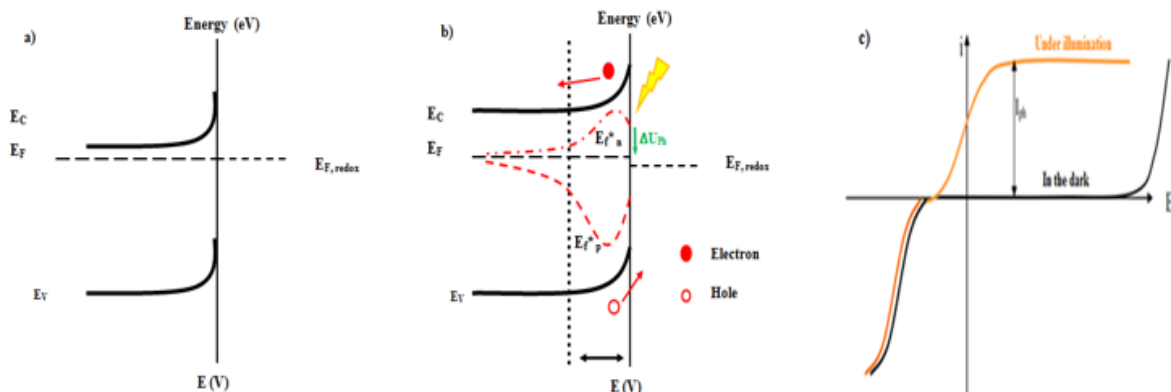


Figure I.6: n-type SC/electrolyte interface: a) in dark, b) under illumination and c) current vs. applied potential evolution in the dark and under illumination.

The difference between the equilibrium potential under illumination and the dark equilibrium potential is called photovoltage (ΔU_{ph}). The excess current compared to the dark situation is called anodic photocurrent (I_{ph}) (Figure I.6 (c)).

I.2 TiO₂ material nanostructures

Materials with carefully controlled nanostructures offer a pathway towards high-rate, high-energy performance through enhancements in kinetic and transport characteristics realized at the nanoscale.

TiO₂ nanostructures in a variety of morphologies such as 0D (quantum dots), 1D (nanowires, nanotubes), 2D (nanosheets, nanoflakes), and 3D (nanoparticles, nanoflowers) have been successfully fabricated using various strategies.

Nanoparticulate TiO₂ structures, providing relatively large specific surface area and good adsorption ability, are suffering from an increased recombination rate of photo-induced (e⁻-h) pairs making them unfavorable for photocatalytic applications [16]. In the other hand, one-dimensional TiO₂ nanotubes (TiNT) have attracted significant attention as an alternative or co-material with other material in environmental and energy storage applications because they naturally provide a superior electron transport pathways for charge transfer, have a highly accessible surface (porous structure) and feature good electrochemical behavior and chemical stability which make them one of the best options for good energy density for supercapacitors and photocatalysis applications [17].

The formation of TiNT was first reported by Hoyer et al. [18] via the template assisted method. Thereafter, various approaches have been developed for the synthesis of TiNT including, vapor deposition, hydrothermal growth, electrochemical anodization and so on. The electrochemical anodization is the most widely utilized synthesis approach [19]. Comparatively to other TiO₂ nanostructures, TiNT are one of the most studied nanostructure materials, owing to their large surface area, chemical stability, relatively high surface-to-volume ratio and vertical tube alignment for one-dimensional electron transport. So, TiNT have particularly attracted increasing attention in solar energy harvesting and conversion [20].

I.2.1 Drawbacks of TiO₂ nanostructures

In contrast to many advantages of TiO₂ cited above, the efficiency of its potential applications is limited by two drawbacks: (i) the band gap of 3.2 eV which allow only the absorption of UV light (wavelength range comprising only a small part of the solar spectrum (4%) as shown in

figure I.7 and (ii) the high recombination rate of electron-hole pairs which yield a limited photoactivity.

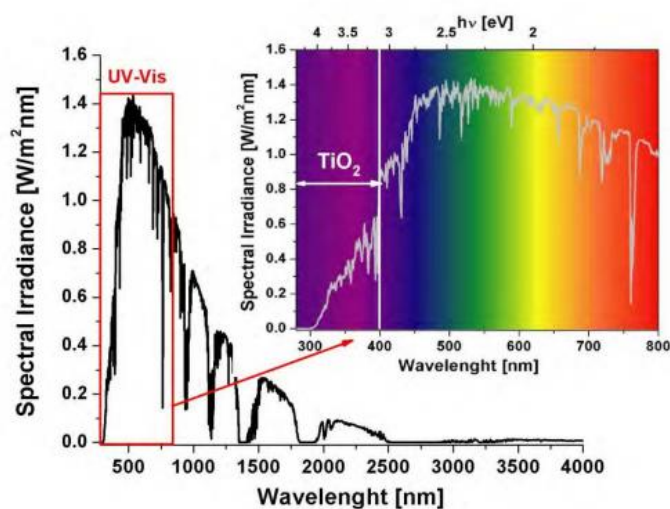


Figure I.7: The solar irradiance vs. wavelength and UV-Vis range of solar spectrum. The absorption range of TiO₂ is also indicated.

Several strategies have been used to increase the photoactivity performance of TiO₂. Much attention has been paid for improving charge carrier separation for an efficient electron transfer mechanism, increasing surface active area for maximal catalytic reaction and increasing light absorption over the whole solar spectrum range.

Common approaches to enhance the performances of TiO₂ include intrinsic measures such as selecting the right physical characteristics including optimizing morphology [21] and optimizing crystal structures (crystal facets) [22]. Other strategies such as bandgap reduction by chemical doping [23], heterojunction formation with other material [24] and decoration with plasmonic materials [25] were also used.

I.2.2 Improvement of TiNT performance

One of the objectives of improving the performance of TiO₂ nanomaterials is to increase their optical activity by shifting the onset of response from the UV to the visible region. There are several ways to achieve this objective, one may cite crystal facets engineering, band gap engineering, heterojunction engineering and so on.

I.2.2.1 Crystal facets engineering

Crystal orientation engineering is a commonly used approach for optimizing the performance of various crystalline catalysts semiconductors due to its pronounced impact on how electrons and holes are separated by surface arrangement. Therefore, it was found that an improved photocatalytic reaction can be realized with facets with a higher fraction of undercoordinated atoms. Thus, the exposure of different crystal planes of anatase may influence the reactivity of TiO₂ crystallites for various applications.

During the crystal growth, anatase with {001} facets which has a high surface energy usually vanished and is replaced or covered by {101} facets with low-energy surface. However, theoretical predictions indicate that {001} facets offer interesting features in a variety of applications because of its high surface energy and unique atomic structure. So, significant efforts were expended in order to experimentally achieve the {001} facets. The most common synthesis methods to control the exposed facets of a single crystal TiO₂ are the hydrothermal and solvothermal methods, by manipulating both the crystal nucleation and growth behaviors [26].

I.2.2.2 Band gap engineering

(a) Doping

Chemical doping is the most effective strategy for overcoming drawbacks of TiO₂ by modifying their electronic structure, through incorporating other electronic active species into the lattice. One may identify:

(i) Non-metal doping

In anionic doping, the O²⁻ ions are replaced by nonmetallic atoms. The most nonmetal doping elements are nitrogen and carbon. Doping TiO₂ with carbon based materials has been extensively investigated and attracted a significant interest due to their specific characteristics, which include abundance, low cost, superior corrosion resistance, high electron conductivity and large specific surface area [27, 28]. Carbon materials in different forms play important roles in both photocatalysis, where they are acting as an adsorbent of pollutant, and electrochemical energy storage. Among the carbon based materials, graphene is the fundamental building of all other dimensional carbon materials (Figure I.8), it is an exceptional material with two-dimensional, single-atomic plane and flat honeycomb structure. Graphene has unique physical and chemical properties including high specific surface area, high chemical

stability and elasticity along with excellent electrical conductivity. These unique properties make it suitable for energy storage and photocatalytic applications [29].

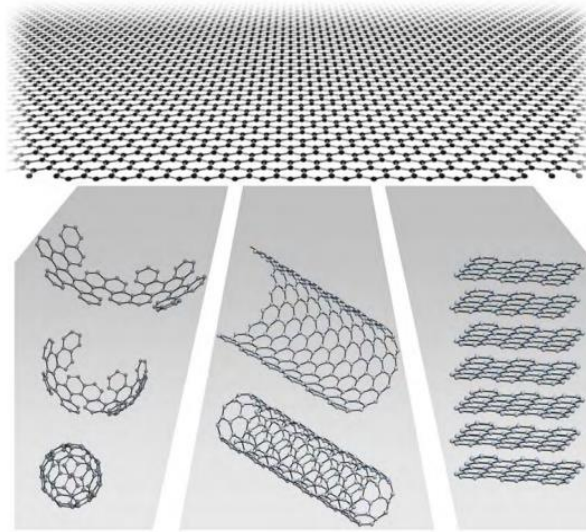


Figure I.8: Single layer graphene, as a parent to other carbonaceous materials: 0D fullerenes, 1D nanotubes and 3D graphite [30].

(ii) Metal doping

Several approaches for TiO₂ modification by metal doping have been proposed in the literature, which cover a wide range of elements, such as Fe, Cu and Mn [31-33]. In the band structure, dopant ions generate valuable energy levels that can be utilized to trap electrons or holes and separate carriers from the bands. Besides, metal doping widens visible light absorption, enhances the conversion efficiency by enhancing the separation rate of photogenerated electrons and holes [23].

(iii) Self-doping

Many studies demonstrated that self-doping may be used for a variety of purposes, including supercapacitors [34], photoanodes in photoelectrochemical water splitting and degradation of contaminants [35].

The defect states can be engendered by activating the TiO₂ semiconductor via self-doping. This phenomenon has been related to oxygen vacancies induced by the reduction of Ti⁺⁴ to Ti⁺³ in the anatase lattice. The presence of defect gap states (Ti⁺³) results in an almost metallic behavior of the material. This provides a significant improvement in PEC and photocatalytic applications [36].

(b) Semiconductor heterojunction

One of the most common strategies to address fast charge recombination and thus increase solar conversion efficiencies is to increase the spatial separation of charge by creating a heterojunction.

A heterojunction can be formed when two different SCs with unequal band structures are put in contact. Depending on their respective band structures, three types of heterojunctions can be formed: (i) those with a straddling gap (type-I), (ii) those with a staggered gap (type-II), and (iii) those with a broken gap (type-III) (see [Figure I.9](#)).

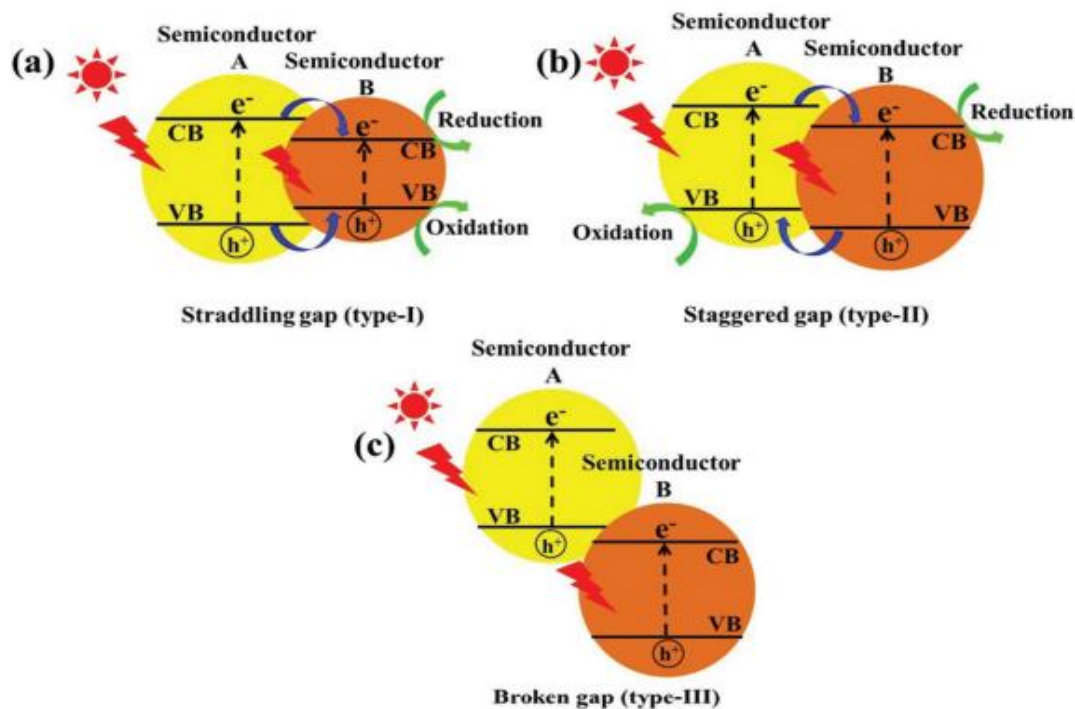


Figure I.9: Schematic representation of three different heterojunctions between two semiconductors [37].

(i) Type-I heterojunction: The conduction and valence bands of the SC_A surround those of the SC_B . In this case, the photogenerated electrons and holes will tend to accumulate in the SC_B . This configuration does not allow charge separation, and may even lead to higher recombination rates.

(ii) Type-II heterojunction: The conduction and valence bands of both SCs are staggered. In this case, the electrons will tend to accumulate towards the SC_B and the holes towards the SC_A . This configuration is ideal and allows to improve the charge separation and thus to decrease the recombination rate.

(iii) Type-III heterojunction: There is no overlap between the bands of the two SCs. So, this kind of heterojunction is considered unsuitable for the migration and separation of electron-hole pairs.

The combination of TiO_2 with other semiconductors, exhibiting narrower band gaps, form a type-II heterojunction. One may cite Cu_2O_3 [38], WO_3 [39], Fe_2O_3 [40] and Bi_2O_3 [41]. These heterojunctions showed a significant improvement in photocatalytic properties of TiO_2 . In fact, under light irradiation, narrower band gap SC inject photogenerated electrons into the conduction band of the larger band gap SC. Whereas, the photogenerated holes migrate to the narrower band gap SC (Figure I.10), resulting in more efficient electron-hole pairs separation and thus good photocatalytic performances.

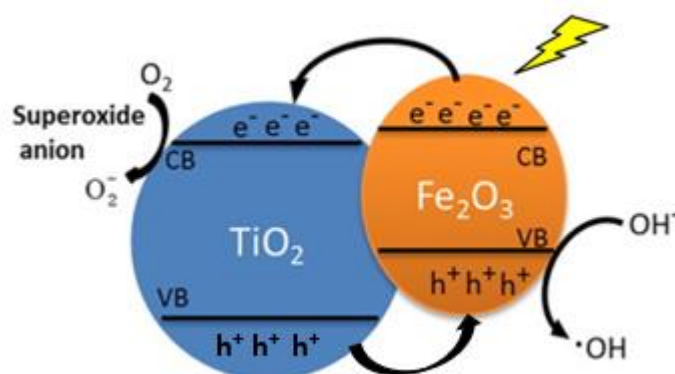


Figure I.10: Photo excited semiconductor heterostructure [42].

II.2.2.3 Surface sensitization by plasmonic materials

Decorating TiO_2 with metallic nanoparticles (NPs) is a common modification method to increase their active area for improving photoactivity performances. In particular, decoration of TiO_2 with noble metal NPs has attracted a lot of attention as it can enhance the separation of the photogenerated electron hole pairs and improve the absorption of a SC in the visible light region. The most common noble metal NPs decorators for TiO_2 photocatalyst are: Au, Pt, Ag and Pd, which may: (i) act as electron traps for facilitating the separation of charge carriers and preventing their recombination, (ii) modify the surface properties of TiO_2 and (iii) extend the absorption spectrum into the visible range through localized surface plasmon resonance (LSPR) effect [43].

LSPR is generated due to the collective oscillations of conduction electrons induced by the electric field of incident visible light photons. Five primary mechanisms have been proposed

to explain the metal SPR-enhanced photoactivities of SCs involving several processes, including: (A) hot electron injection, (B) local electromagnetic field enhancement, (C) dipole-dipole-coupling-enabled resonant energy transfer (so-called plasmon-induced resonant energy transfer), (D) light scattering, and (E) plasmonic heating effect.

Figure I.11 recapitulates the primary mechanisms for LSPR-Enhanced Photoactivity of SCs. Each of these mechanisms has its own advantages and drawbacks. Despite significant advances in the last decade, no clear agreement has been reached on the physics behind those interactions or their actual importance in driving photochemical processes.

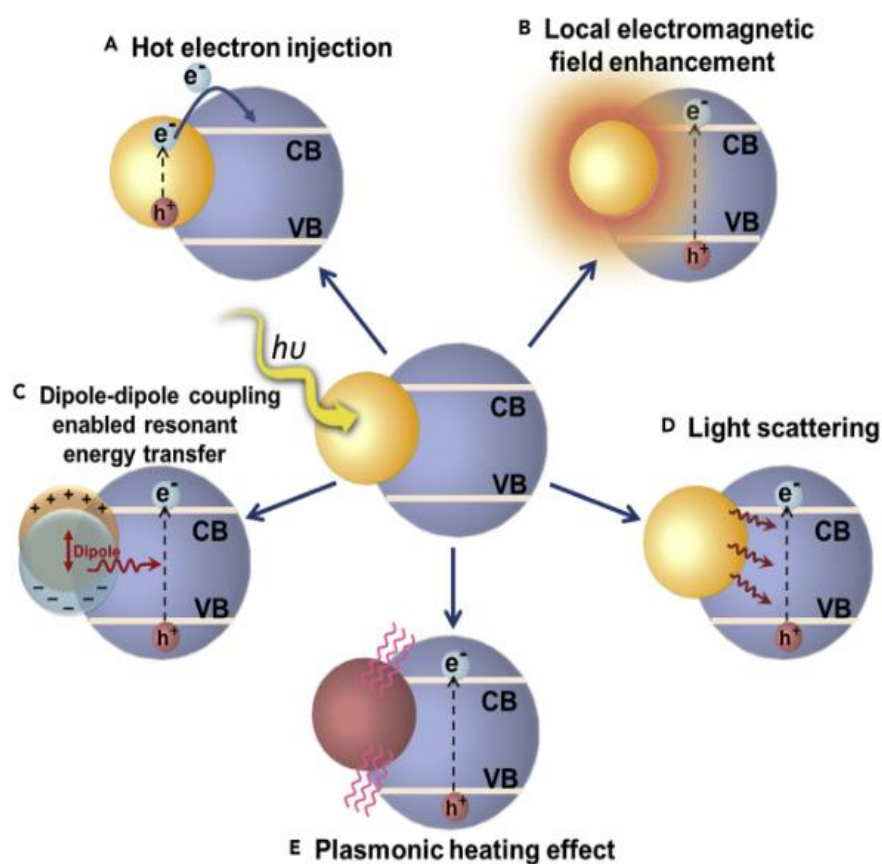


Figure I.11: Diagrams of Different Mechanisms for LSPR-Enhanced Photoactivity of SCs [44].

Mechanisms (A) and (B) are generally the most reported to describe the plasmonic metal/SC coupling, we will then describe them very briefly.

- (A) Hot electron injection: Excited electrons that enter in resonance with the incoming field is composed mostly by charges with low energies (close to the Fermi level of the metal) and a small population of highly energetic ones that can be characterized as hot electrons. Those electrons can be transferred into the SC in the first 100 fs after plasmonic excitation. To achieve

an efficient injection, two important characteristics have to be controlled: a correct band alignment between the Fermi level of the metal and the CB of the SC and the Schottky barrier between the two components. For illustration, Ag plasmonic enhancement of TiO₂ is depicted in [figure I.12](#) below. Ag NPs, as the photosensitizer, were excited under visible light irradiation. Electrons from the LSPR of Ag, possess enough energy to overcome the Schottky barrier formed at the interface and that possibly decreases the recombination rate of photogenerated electron-hole pairs of TiO₂.

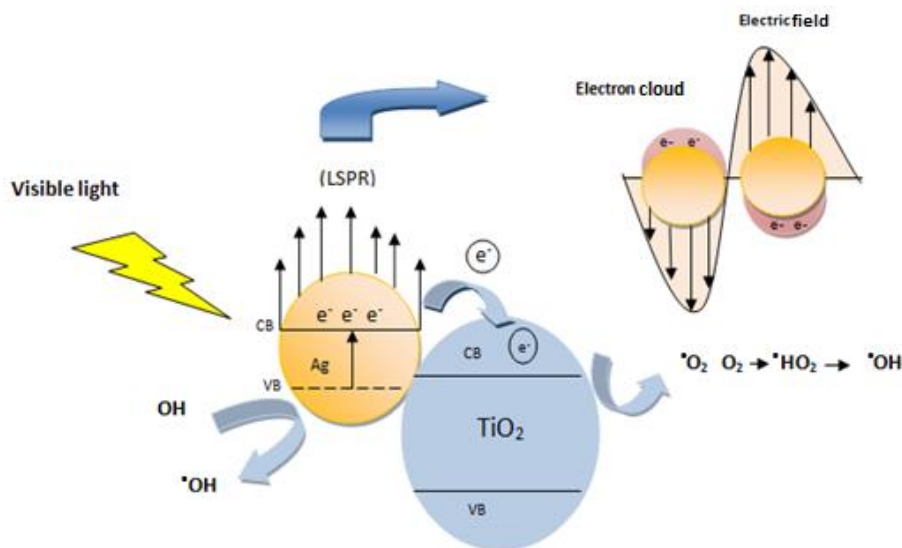


Figure II.12: One of the suggested mechanisms for charge transfer in Ag/TiO₂ heterojunction under visible light irradiation [45].

- (B) Local electromagnetic field enhancement: This process is attained when both the metal and the SC are in close proximity and excited simultaneously. In this situation, the plasmonic NPs act as an antenna focalizing the incident energy in their surroundings, hence increasing the absorption cross-section of the semiconductor.

Note that LSPR effect depends strongly on the shape, size, geometry, specific material of the NPs as well as on the surrounding dielectric environment. An important distinguishing feature of LSPR is that the resonant frequency can be tuned to the desired range by controlling these parameters [46].

I.3 Applications of TiO₂ nanostructures

TiO₂ nanostructures have several advantages making them as the most important existing resources with promising usage in a wide range of fields including:

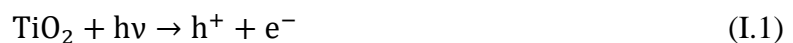
I.3.1 Heterogeneous photocatalysis (Water treatment/depollution)

Photocatalysis is attracting great interest because it has been shown to be effective in degrading a variety of pollutants and harmful substances by photo-oxidation processes, which concentrate on the production of oxidizing species like hydroxyl radicals which are essential for the degradation processes for water treatment technology. Photocatalysis offers a number of benefits including: (i) low-cost, (ii) complete mineralization (total conversion of organic pollutants into CO₂) and (iii) mild operating conditions (atmospheric temperature and pressure) [47].

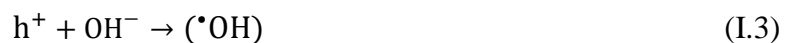
The overall process of photocatalysis was suggested for the first time by Herrmann et al. [48]. It can be decomposed into five independent steps:

1. Transfer of the reactants from the bulk phase to the surface of SC.
2. Adsorption of the reactants.
3. Reaction in the adsorbed phase:
 - i. Absorption of the photon by the catalyst.
 - ii. Formation of electrons (e⁻) and holes (h⁺).
 - iii. Migration of the photogenerated charges to the catalyst surface and induction of oxidation-reduction reactions of photogenerated electrons and holes pairs with adsorbed species.
4. Desorption of the product(s).
5. Removal of the products from the interface region.

The activation of TiO₂ by absorption of a photon, with energy higher than or equal to the band gap, is the first component of step number 3. This will cause an e⁻ to be promoted from the valence band to the conduction band, which will result in the charge separation of electrons and holes through the following equation:

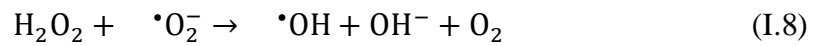


The photogenerated electron-hole pairs participate in many oxidation or reduction processes, the holes react to produce highly reactive hydroxyl radicals (*OH) from a simple oxidation of water or surface hydroxyl ions (OH⁻), according to the following reactions:



These very oxidizing radicals are responsible for the degradation of the pollutant.

The series of chain oxidative–reductive reactions that occur at the photon-activated surface has been broadly proposed [49] as:

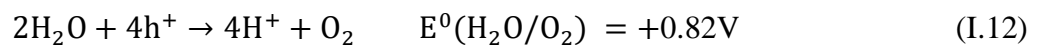
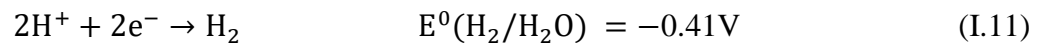


As a result, these different radicals can react with organic substances to generate CO₂ and H₂O. **Figure I.13** depicts the photocatalytic mechanism in the presence of organic pollutant.

I.3.2 Photoelectrochemical (PEC) water splitting

Water splitting into hydrogen and oxygen is a thermodynamically uphill chemical reaction which requires the standard Gibbs free energy change (ΔG°) of 237.141 kJ mol⁻¹ or 1.23 eV. PEC water splitting is a process where water is split into hydrogen and oxygen using an electric current during light irradiation. This was first demonstrated by Honda and Fujishima [1], who used an n-type TiO₂ rutile photoanode and platinum cathode.

Four mechanisms are involved in the PEC water splitting process: (i) photocatalyst absorbs photons with energies higher than its bandgap energy, moving electrons from the valence band into the conduction band, (ii) formation of electron-hole pairs, (iii) charge separation followed by migration of these photogenerated carriers, (iv) hydrogen evolution and oxygen evolution on the two different electrodes, as described by the following equations:



As an example, the working principle of TiNT based PEC cell is shown in **figure I.14**.

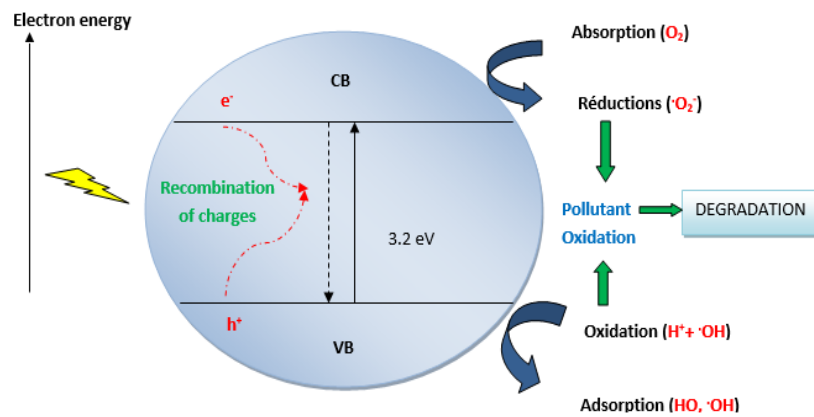


Figure I.13: Photocatalytic process mechanism.

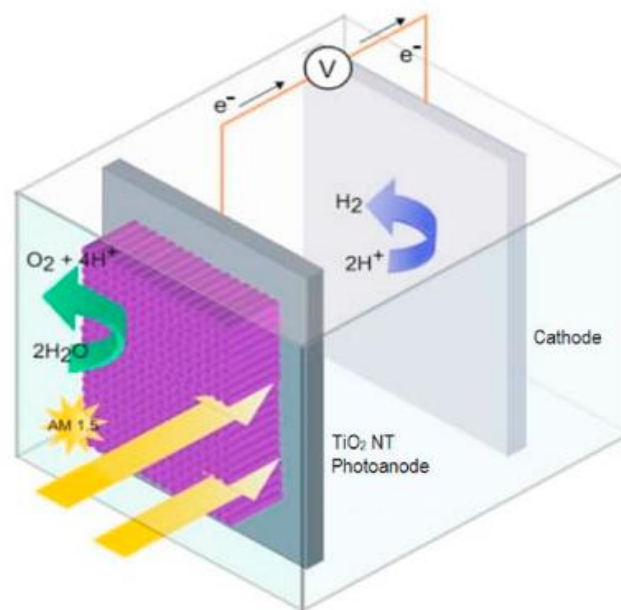


Figure I.14: Fundamental principles of water splitting by photoelectrochemical cell [50].

I.3.3 Electrochemical energy storage

Nowadays, there has been a critical concern with energy storage due to the limitations of old-fashioned storage technologies. Devices known as electrochemical storage systems are capable of converting chemical energy into electricity and storing. Batteries, electrochemical capacitors

(capacitors, supercapacitors) and fuel cells could be other subcategories of electrochemical energy storage technologies.

The difference in energy storage technologies leads to different energy and power capabilities. In general, energy density and power density are the two important parameters for evaluating the performance of energy storage devices. This performance is estimated by Ragone diagram, which represents the relative power densities and energy densities (Figure I.15). The gray lines represent the time necessary to charge or discharge the device compared to the others. It clearly shows that supercapacitors have significant role in terms of high specific power and relatively high specific energy. This indicates that it may be charged or discharged quickly while still retaining an acceptable quantity of energy stored per unit mass.

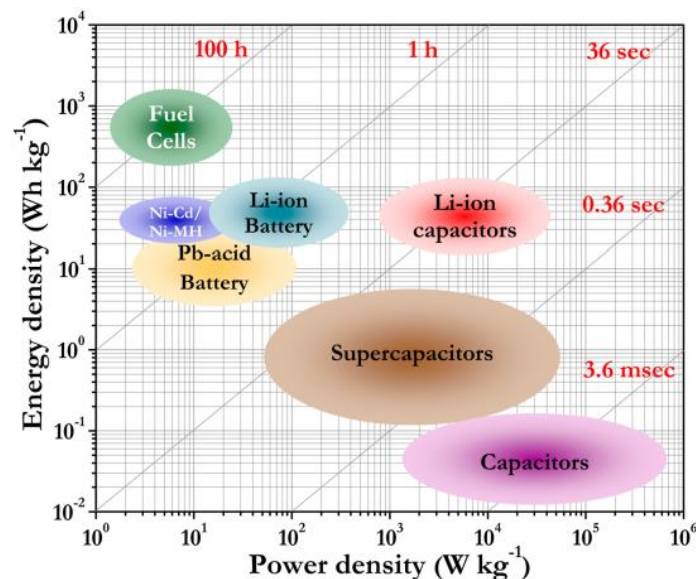


Figure I.15: Ragone diagram that displays the power and energy densities of different energy storage devices [51].

The structure, mechanism, and performance of supercapacitors as an electrochemical energy storage device are described in the following sections to highlight their benefits.

I.3.3.1 Supercapacitors

Supercapacitors or ultracapacitors are energy storage technologies with high capacitance, longer shelf life and cycle life, high power density and short charge discharge times. Supercapacitors can take and deliver a charge more quickly than batteries and they may be fully charged and discharged in few seconds [52].

Supercapacitors store energy directly in the form of an electrostatic charge due to the double layer formation in the electrode/electrolyte interface (Figure I.16) and they use electrodes with higher specific surface area. For that reason, the capacity and energy would be enhanced amazingly. The expensive cost of supercapacitors is a significant barrier to their wide application. To overcome the major obstacles of supercapacitor and to achieve a higher performance, researchers are exploring new materials with low cost and large specific surface area [53-55].

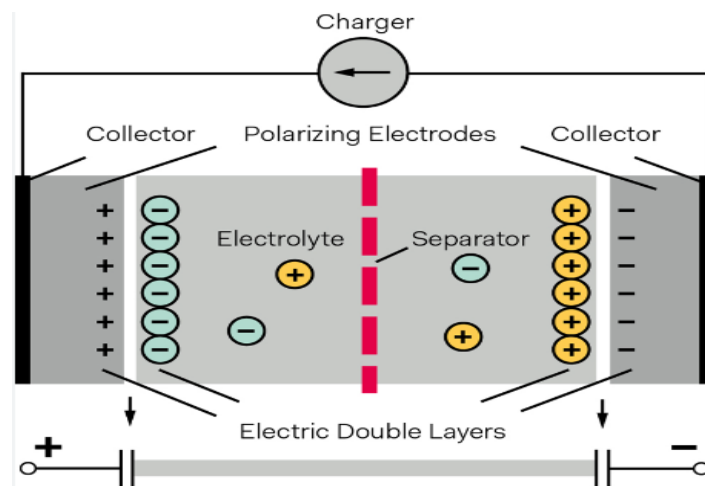


Figure I.16: Supercapacitor cell [56].

I.3.3.1.1 Types of supercapacitors

Three categories of supercapacitors (Figure I.17) may be distinguished based on the energy storing principles: Electric double layer capacitors, pseudocapacitors and hybrid capacitors. Electrical double layer capacitor (EDLC) has the particularity of storing charges electrostatically via the formation of an electric Helmholtz double layer at the interface of the electrode and electrolyte. Whereas pseudocapacitor (or redox supercapacitor) is obtained from the rapid faradic reactions that occur on either the surface or majority of an electrode [57]. Combination of both carbon material and pseudocapacitive additive is called Hybrid supercapacitor. This combination is an effective way to overcome the shortcomings of EDLC and pseudocapacitor devices to achieve efficient supercapacitor performance.

Supercapacitor electrodes made of TiO_2 have mostly been employed as a nanostructured support or current collector when combined with other EDLC material which are known to

have capacitive characteristics. Modified TiO₂ nanomaterials have recently been studied for their potential as supercapacitors [55].

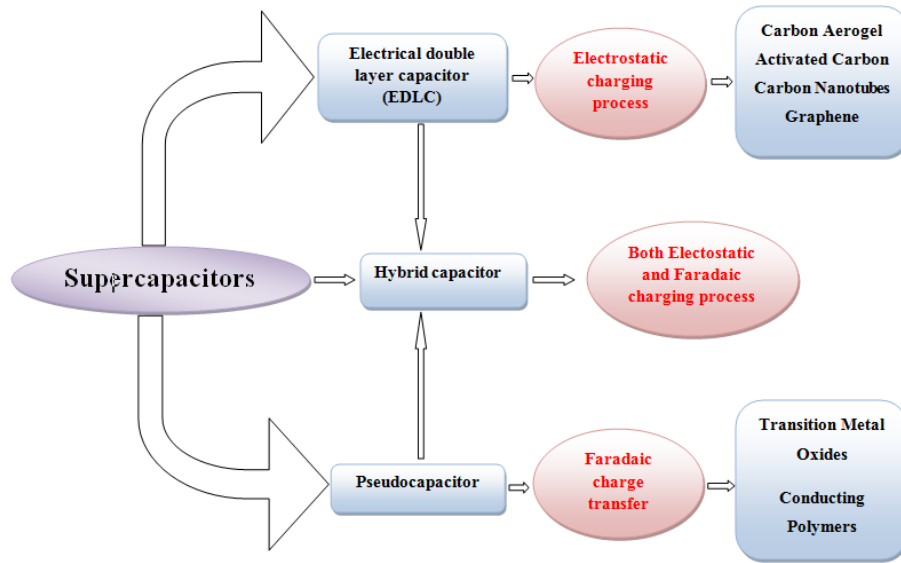


Figure I.17: Classification of supercapacitors

I.3.3.1.2 Electrical Double Layer Capacitors

Supercapacitors based on the electric double layer capacitors or electrostatic supercapacitors can store much more energy because of the very high effective area and the atomic-scale charge separation distances.

The energy storage process of EDLCs takes place at the interface between the electrode surface and the electrolyte. When a voltage is applied across the electrodes, the charge builds up through electrostatic interactions at the contact between the electrode surface and electrolyte, electrons go across an external circuit from the negative electrode to the positive electrode during the charging process. Anions migrate toward the positive electrode in the electrolyte whereas cations move in the other direction. The opposite processes occur during the discharge process. This type of physical ion adsorption is all that occurs in EDLCs; there are no ion exchanges or charge transfers between the electrode and electrolyte associated with non-faradaic processes. Consequently, in EDLCs the charge storage is highly reversible, they may achieve extremely high cycle stability. This kind of supercapacitor is characterized by low capacitance and energy density. The concept of a double layer was first introduced by Helmholtz in 1879 [58]. The Helmholtz model hypothesized that counter-ions form a monolayer near the electrode surface, as illustrated in figure I.18 (a). This structure is comparable to that of a conventional dielectric capacitor with two planar electrodes separated

by a small distance (d). Gouy and Chapman modified the Helmholtz model and proposed the diffuse model of EDLCs. This model accounts for the fact that the ions are mobile in the electrolyte solution under the combined effects of ion diffusion driven by concentration gradients and electromigration driven by the electric potential gradient, i.e., the electric field. This results in the so-called “diffuse layer” illustrated in figure I.18 (b). This model was also modified by Stern who combined the two theories discussed above [59] to explicitly describe two distinct regions, namely (1) the inner region termed the Stern layer, delimited by the inner Helmholtz plane (IHP) and the outer Helmholtz plane (OHP) and (2) the outer region called the diffuse layer, as shown in figure I.18 (c).

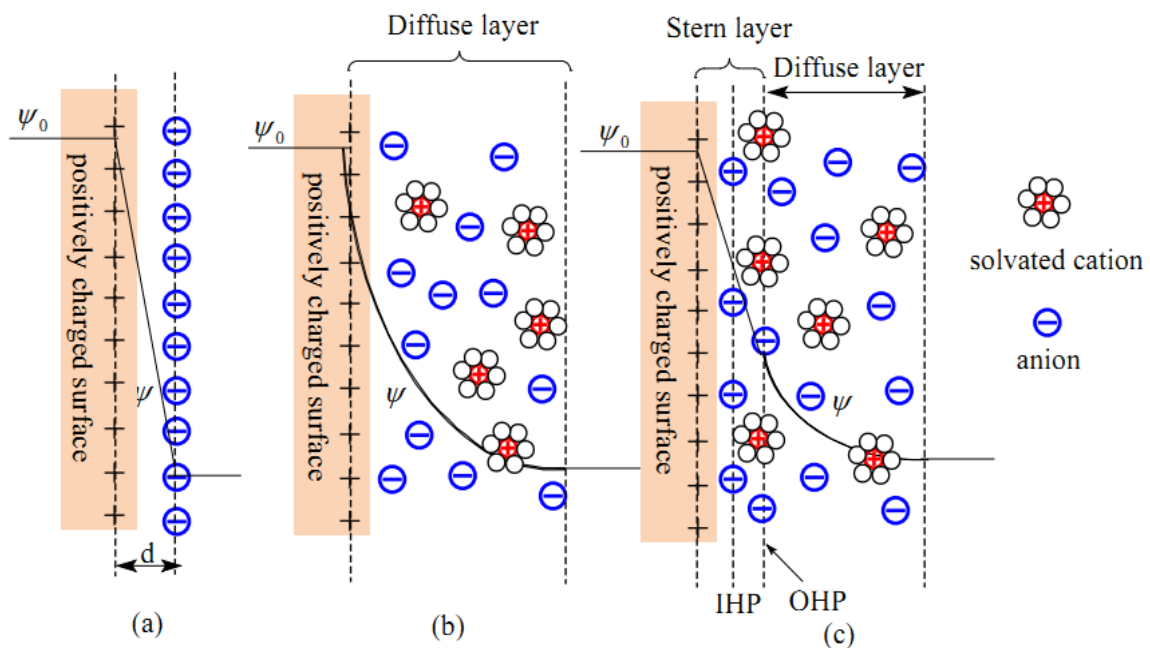


Figure I.18: Schematic representation of electrical double layer structures according to: (a) the Helmholtz model, (b) the Gouy-Chapman model, (c) the Stern model [60]. (ψ_0 is the potential at the electrode surface).

The most frequent electrode materials used in EDLCs are carbon nanotubes, carbon aerogels, and activated carbon [61]. The later are commonly employed in commercial supercapacitors due to their low cost, high surface area (1000–2500 m²/g), widely distributed pore sizes ranging from the micropores to macropores and their availability in different forms.

II.3.3.1.3 Pseudocapacitors

Contrary to EDCLs, pseudocapacitors or faradaic supercapacitors store energy electrochemically by Faradaic reaction at the interface between electrode and electrolyte.

Electrosorption (underpotential deposition), redox reactions (redox pseudocapacitance) and intercalation processes are used to carry out these Faradaic reactions [57].

The electrosorption occurs when metal ions form an adsorbed monolayer on the surface of a different metal above their redox potential. This is the situation of lead deposited on the gold surface. In the system of redox reactions, ions are electrochemically adsorbed onto or close to the surface of electrodes with rapid faradaic charge transfers [62].

The most commonly electrode materials used as pseudocapacitors are based on conducting polymers or metal oxides. Conducting polymers such as polyaniline (PANi), polypyrrole (PPy) and poly (3,4-ethylenedioxythiophene) (PEDOT), with high electrical conductivity, good charge density and low cost are widely used. The charges are stored at the surface and bulk of the electrode by quick and reversible redox processes [63]. Transition metal oxides including ruthenium oxide, iridium oxide, manganese oxide, cobalt oxide, nickel oxide, iron oxide and titanium oxide are promising electrode materials for Faradic supercapacitor devices due to their abundant reserves, environmental friendliness, accessibility, large surface area and high theoretical specific capacitance [64, 65]. However, these transition metal oxides exhibit some drawbacks which limit their applications, such as their low electrical conductivity, unstable volume expansion and slow ion diffusion in the bulk phase [66]. Furthermore, the performance of cycling stability and rate capabilities may significantly be critically affected through many charge-discharge processes during reduction-oxidation reactions which limit the stability of these pseudocapacitors [67].

To overcome their drawbacks, significant efforts have been performed to enhance their electrochemical properties, one may cite: (i) co-existing two different cations in a single crystal structure to improve electrical conductivity and (ii) developing the porosity of metal oxides which plays an important role in providing a large specific surface which hence facilitates the transport of ions in the electrolyte [68].

I.3.3.1.4 Hybrid supercapacitors

The hybrid supercapacitor is a combination of EDLC and pseudocapacitor. The combination of these two storage mechanisms constitutes the energy storage mechanism of hybrid supercapacitors. One-half of the hybrid supercapacitor acts as EDLC while other half behaves as pseudocapacitor. Hybrid supercapacitor has higher working potential and yields higher capacitance which is two to three times more than that of conventional capacitor as well as of

EDLC and pseudocapacitor. They use both Faradaic and non-Faradaic processes to store charge and achieve higher energy and power densities than EDLCs without the tradeoffs in cycle stability and price that have hampered the development of pseudocapacitors. The research has concentrated on two different forms of hybrid capacitors differentiated by their electrode arrangement: (a) asymmetric hybrids and (b) battery-type hybrids [69].

(a) Asymmetric hybrids: The asymmetric hybrid capacitor systems are developed in order to improve energy and power density of electrochemical capacitors. Some of their important characteristics are [70]:

- Configured so that the conducting polymer or metal oxide is utilized as the positive electrode and the carbon material is used as the negative one.
- Elevate the efficiency to some extent and yield elevated power and energy density in addition to improved cycling stability.

(b) Battery-type hybrids: The battery-type hybrids combine a supercapacitor electrode with a battery electrode, so this configuration combines the energy characteristics of batteries with the power, cycle life and recharging times of supercapacitors [69].

Conclusion

In this chapter, we have established the most important properties of TiO_2 . Despite being a material of interest in the most advanced applications involving solar energy, it suffers from low visible absorption and photogenerated carrier recombination. For this purpose, a number of strategies have been reported to shift its absorption towards the visible light and to reduce its photogenerated recombination rate. Among these strategies, heterojunction engineering has been largely been addressed. Improved charge separation and good absorption in the visible range are achieved through the suitable band alignment at interfaces of the two materials. Apart from applications based on solar energy conversion, energy storage via supercapacitors has been addressed. Specifically, EDLCs are supercapacitors that utilize electrostatic charge separation only. The energy storage process is performed at the interface between the electrode surface and the electrolyte. The electrostatic charge transfer is totally reversible, resulting in efficient devices with long lifetimes.

References

- [1] A. Fujishima, K. Honda, *nature*, 238(1972)37.
- [2] C. C. Raj, R.V. Prasanth, *Journal of The Electrochemical Society*, 165(2018)345.
- [3] K.R. Zhu, M.S. Zhang, J.M. Hong, Z. Yin, *Materials Science and Engineering*, 403(2005)87.
- [4] A. Fujishima, X. Zhang, and D.A. Tryk, *TiO₂, Surface Science Reports*, 63(2008)515.
- [5] A.N. Banerjee, *Nanotechnology, science and applications*, 4(2011)35.
- [6] X. Chen and S. S.Mao, *Chemical Reviews*, 107(2007)2891.
- [7] V. Etacheri, C. D. Valentinc, J. Schneider, D. Bahnemann, S.C. Pillai, *Journal of Photochemistry and Photobiology C: Photochemistry Reviews* 25(2015)1.
- [8] J. Pan, G. Liu, G.Q.M. Lu, H.-M. Cheng, *Angewandte Chemie International*, 50(2011) 2133.
- [9] N.M. Dimitrijevic, Z. V. Saponjic, B.M. Rabatic, O.G. Poluektov, T. Rajh, *Journal of Physical Chemistry C*, 111(2007)14597.
- [10] G. Liu, H.G. Yang, J. Pan, Y.Q. Yang, G.Q. (Max) Lu, H.-M. Cheng, *Chemical Reviews*, 114(2014)9559.
- [11] M. Kapilashrami, Y. Zhang, Liu, A. Hagfeldt, J. Guo, *Chemical Reviews*, 114(2014)9662.
- [12] M. Landmann, E. W. G. S. Rauls, W. G. Schmidt, *Journal of Physics: Condensed Matter*, 24(2012)195503
- [13] A. Hagfeldt, G. Boschloo, L. Sun, L. Kloo, and H. Pettersson, *Chemical Reviews*, 110(2010)6595.
- [14] F. Huang, A. Yan, H. Zhao, *Semiconductor Photocatalysis - Materials, Mechanisms and Applications*, (2016)31.
- [15] J. Nowotny, M. Radecka, M. Rekas, *Journal of Physics and Chemistry of Solids*, 58(1997) 927.
- [16] X. Yang, D. Wang, *Semiconductors and Semimetals*, 97(2017)47.
- [17] X. Pan, Y. Zhao, S. Liu, C. L. Korzeniewski, S. Wang, Z. Fan, *ACS Applied Materials & Interfaces*, 4(2012)3944.
- [18] Y. Xie, L. Zhou, C. Huang, H. Huang, and J. Lu, *Electrochimica Acta*, 53(2008)3643.
- [19] P. Roy, S. Berger, P. Schmuki, *Angewandte Chemie International*, 50(2011)2904.
- [20] S. Reghunath, D. Pinheiro, S. D. KR, *Applied Surface Science Advances*, 3(2021)100063.
- [21] N. Lakshminarasimhan, E. Bae, W. Choi, *Journal of Physical Chemistry C*, 111(2007)15244.

- [22] C. Dette, M. PéréOsorio, A. Kley, C. S. Punke, P. Patrick, C. E. Jacobson, P. Giustino, F. Jung, S. J. Kern, K. Nano Letters, 14(2014)6533.
- [23] Nah Y-C, I. Paramasivam, Physical Chemistry Chemical Physics, 11(2010)2698.
- [24] Y. Wang, S. Cao, Y. Huan, T. Nie, Z. Ji, Z. Bai, Applied Surface Science, 526(2020)146700.
- [25] M. Z. Ge, C. Y. Cao, S. H. Li, Y. X. Tang, L.N. Wang, N. Qi, Nanoscale, 8(2016)5226.
- [26] R. Katal, S. Masudy-Panah, M. Tanhaei, M. H. D. A. Farahani, H. Jiangyong,. Chemical Engineering Journal, 384(2020)123384.
- [27] M. Asiltürk and Ş. Şener, Chemical Engineering Journal, 180(2012)354.
- [28] M. Z. Ge, S. H. Li, J. Y. Huang, K. Q. Zhang, S.S. Al-Deyab, Y.K. Lai, Journal of Materials Chemistry A, 3(2015)3491.
- [29] A. Ramadoss, S. J. Kim, Carbon, 63(2013)434.
- [30] A. K. Geim, K. S. Novoselov, 6(2007)183.
- [31] SH. Kim, SY. Choi. Journal Electroanalytical Chemistry. 744(2015)45.
- [32] M. L. Chen, F. J. Zhang, K. Zhang, Z. D. Meng, Chemical Reviews, 34(2010)283.
- [33] W. Zhang, W. D. Zhou, J. H. Wright, Y. N. Kim, D. W. Liu, X. C. Xiao. ACS Applied Materials & Interfaces, 6(2014)7292.
- [34] H. Zhou, Y. Zhang, The Journal of Physical Chemistry C, 118(2014)5626.
- [35] I. Paramasivam, H. Jha, N. Liu, P. Schmuki, small, 8(2012)3073.
- [36] X. Zhang, B. Zhang, D. Huang, H. Yuan, M. Wang, Y. Shen, Carbon, 80(2014)591.
- [37] J. Low, J. Yu, M. Jaroniec, S. Wageh, A. Al-Ghamdi, Advanced materials, 29(2017)1601694.
- [38] L. Rekeb, L. Hamadou, A. Kadri, N. Benbrahim, and E. Chainet, International Journal of Hydrogen Energy, 44(2019)10541.
- [39] I. Paramasivam, Y. C. Nah, C. Das, N. K. Shrestha, P. Schmuki, Chemistry–A European Journal, 16(2010) 8993.
- [40] F. Haitao, S. Shiyu, Y. Xiaohong, W. Li, A. Xizhong, H. Zhang, Y. Dong, Jiang, Yu. Aibing, Powder Technology, 328(2018)389.
- [41] L. Rekeb, L. Hamadou, A. Kadri, and N. Benbrahim, Electrochimica Acta, 256(2017)162.
- [42] A. Umar, M. Abaker, M. Faisal, S.W. Hwang, S. Baskoutas, S.A. Al-Sayari, Nanoscience. Nanotechnology, 11(2011)3474.
- [43] C. H. Lee, S. W. Rhee, H. W. Choi, Nanoscale Research Letters, 7(2012)48.
- [44] N. Zhang, C. Han, X. Fu, Y. J. Xu, Chem, 4(2018)1832.

- [45] K. H. Leong, B. L. Gan, S. Ibrahim, P. Saravanan, *Applied Surface Science*, 319(2014) 128.
- [46] K. Arifin, R.M. Yunus, L.J. Minggu, M. B. Kassim, *International Journal of Hydrogen Energy*, 46(2021)4998.
- [47] A. Mills, R. H. Davies, D. Worsley, *Chemical Society Reviews*, 22(1993)417.
- [48] J. M. Herrmann, *Catal Today* 53(1999)115.
- [49] S. Dong, J. Feng, M. Fan, Y. Pi, L. Hu, X. Han, M. Liu, J. Sun and J. Sun, *Rsc Advances*, 5(2015)14610.
- [50] K. Arifin, R.M. Yunus, L. J. Minggu, M. B. Kassim, *international journal of hydrogen energy* 46(2021)4998.
- [51] V. Aravindan, J. Gnanaraj, Y. S. Lee, S. Madhavi, *Chemecal Reveiws*, 114(2014)11619.
- [52] J. Sung, C. Shin, *Micromachines* 11(2020)1125.
- [53] C. C. Raj, R. Prasanth, *Journal of The Electrochemical Society*, 165(2018)345.
- [54] Y. B. Tan, J. M. Lee. *Journal of Materials Chemistry A*, 1(2013)14814.
- [55] P.Nagaraju, A.Alsalme, A. Alswieleh, R. Jayavel, *Journal of Electroanalytical Chemistry*, 808(2018)90.
- [56] P.L. Fèvre, PRBX, Chief Marketing, *Power Systems Design* (2018).
- [57] V. H. Pham, T.D. Nguyen-Phan, X. Tong, B. Rajagopalan, J. S. Chung, J. H. Dickerson, *Carbon*, 126(2018)135.
- [58] H.V. Helmholtz, *Annals of Physics journal*, 89(1853)353.
- [59] O.Z. Stern, *Electrochem*, 30(1924)508.
- [60] L. L. Zhang and X. S. Zhao, *Chemical Society Reviews*, 38(2009)2520.
- [61] M. Inagaki, H. Konno, O. Tanaike, *Journal of Power Sources*, 195(2010)7880.
- [62] V. Augustyn, P. Simon, B. Dunn, *Energy & Environmental Science*, 7(2014)1597.
- [63] I. Shown, A. Ganguly, L. C. Chen, K. H. Chen, *Energy Science & Engineering*, 3(2015)2.
- [64] C. D. Lokhande, D. P Dubal, O. S. Joo, *Current Applied Physics*, 11(2011)255.
- [65] L. Huang, D. Chen, Y. Ding, S. Feng, Z. Wang and M. Liu, *Nano Letters*, 13(2013)3135.
- [66] C. An, Y. Wang, Y. Huang, Y. Xu, L. Jiao and H. Yuan, *Nano Energy*, 10(2014)125.
- [67] P. Asen, S. Shahrokhian, A. I. zad, *Journal of Electroanalytical Chemistry*, 823(2018)505.
- [68] R. Salunkhe, Y. V. Kaneti, Y. Yamauchi, *ACS nano*, 11(2017)5293.
- [69] J.Cherusseri, D. Pandey, J. Thomas,. *Batteries & Supercaps*, 3(2020)860.
- [70] S. Z Iro, C. Subramani, S.S. Dash, *International Journal of Electrochemical Science*, 11(2016)10628.

Chapter II

Materials, equipments and methods

Introduction

This second chapter describes the experimental methods and characterization techniques used during the course of this thesis. We first present the anodization procedure for the synthesis of TiNT. Next, we report the characterization techniques allowing the determination of the morphological, structural and optical properties of the different developed heterojunctions. The experimental conditions and apparatus used for the photoelectrochemical and photocatalytic measurements are also presented. A particular focus is dedicated to the description of the electrochemical impedance spectroscopy principle and the main ways of evaluating the supercapacitor performance.

Note that the details concerning the preparation of the different heterojunctions can be found in their relevant chapters.

II.1 Fabrication of TiNT

TiNT were fabricated by electrochemical anodization process. The electrochemical anodization experiments were performed in a conventional two-electrode cell, a platinum foil was used as a counter electrode and a titanium sheet (2 mm, 96% purity) served as a working electrode. **Figure II.1** shows the schematic set-up of the anodization process in an electrolyte containing a mixture of organic solvent (ethylene glycol ($C_2H_6O_2$)), distilled water (H_2O) and ammonium fluoride (NH_4F). A direct current power supply was used as the voltage source to drive the anodization. The resulting TiNT at the end of the anodization process are amorphous in nature. As, we are particularly concerned by the anatase structure which is the most thermodynamically stable one and offers several applications, thermal annealing of the as anodized samples in a furnace (NEYTECH QEX) was so carried out at $450^\circ C$ for 3 hours in air.

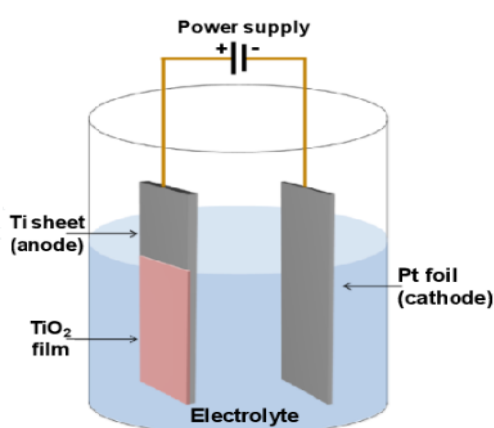


Figure II.1: Schematic set-up of anodization experiments.

II.1.1 Growth process of TiNT

The growth of TiNT by anodization can be governed by two competing reactions: (i) oxide formation at the titanium/oxide interface caused by oxygen anions and (ii) dissolution reaction caused by fluoride ions (F^-) in the electrolyte (Figure II.2). The process can be elucidated simply by the following reactions [1, 2]:

The oxidation (anodic) reaction at Ti/electrolyte interface:



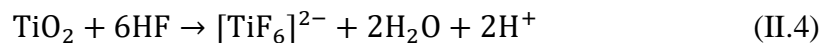
The corresponding cathodic reaction is a reduction of H_2O at the counter electrode:



The formation of titanium oxide layer:



The dissolution of titanium oxide layer:



Reaction (II.3) describes the formation of the TiO_2 compact oxide layer in the absence of hydrofluoric acid (HF). The oxidized metal species (Ti^{4+}) react with O_2^- ions from water to form the oxide layer. The growth of the oxide layer is controlled by the transport of O_2^- and Ti^{4+} ions. As the system is under constant anodization potential, the electric field in the layer is progressively reduced by increasing the thickness of the layer. The compact layer formation process is self-limiting (Figure II.2(a)).

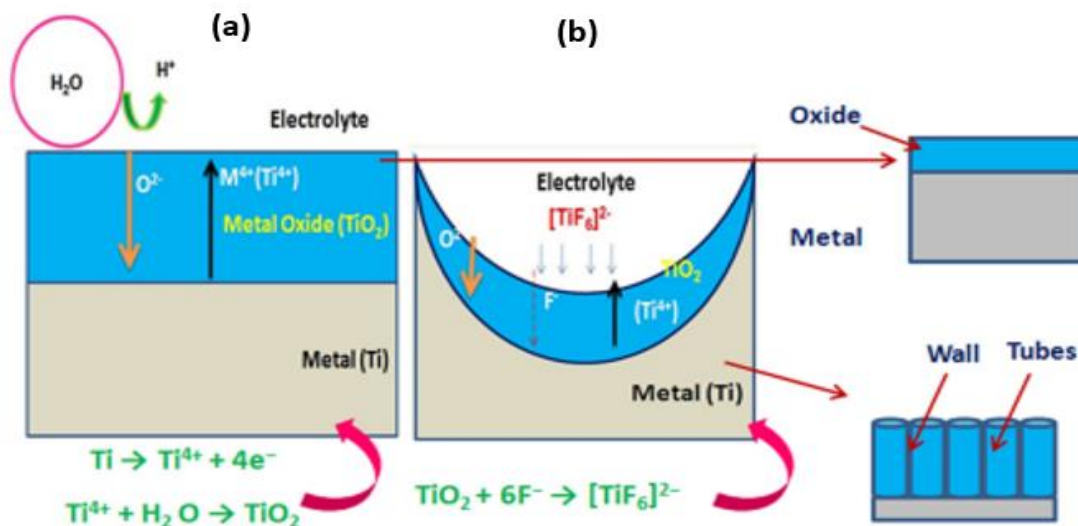


Figure II.2: Schematic illustration of formation mechanism of: (a) TiO_2 compact layer and (b) TiNT [1].

In the presence of F^- ions in the electrolyte, a thin fluorine-rich layer of $[TiF_6]^{2-}$ is formed as a result of the reaction between Ti^{4+} and TiO_2 with F^- through reaction (II.4) in the metal/oxide interface. The fluorine rich layer is prone to chemical dissolution in aqueous electrolyte to form a TiNT layer (Figure II.2 (b)).

In summary, figure II.3 depict the steps formation of TiNT. Stage I: a barrier layer is formed, leading to an exponential decrease of the current. Stage II: the surface begins to be locally dissolved and pores grow randomly, the initiation of pores leads to an increase of the active area and thus of the current. From then on, the pores share equally the available current, which leads to the formation of vertically ordered nanotubes. The III regime is then reached and the current becomes constant. This last phase of anodization is controlled by a diffusion phenomenon; the limiting species being probably $[TiF_6]^{2-}$. More precisely, the stationary regime is established when the growth rate of the oxide (at the metal/oxide interface) is equal to its dissolution rate (at the oxide/electrolyte interface) [2-4].

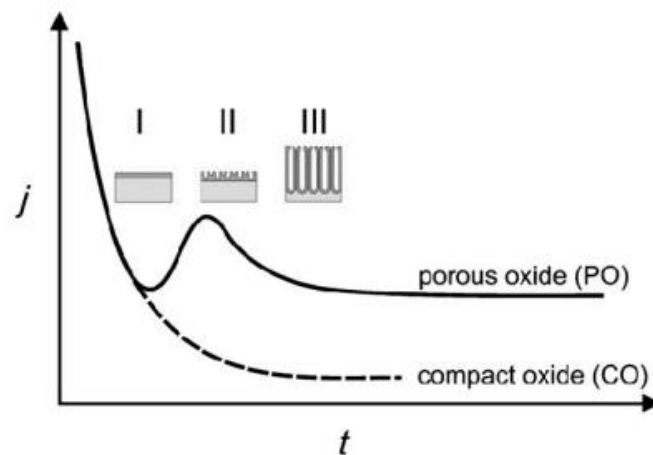


Figure II.3: Typical current–time (j – t) characteristics after a voltage step in the absence (----) and presence (—) of fluoride ions in the electrolyte [5].

II.2 Characterization methods

II.2.1 Physical and structural characterizations

II.2.1.1 Scanning electron microscopy (SEM)

SEM is currently the most used technique for topography at the microscopic scale. The principle of SEM is to scan the surface of the sample by a focused beam of electrons, the electrons interact with atoms of the sample producing secondary and backscattered electrons which can produce high resolution images of the sample surface. The analyzed material must be conductive in order to avoid charge phenomena due to electrons. In the case of non-conductive materials, a metallization can be carried out with the help of carbon or gold.

The combination of a microscope with a microanalyzer allows the detection of X-rays of characteristic wavelengths to establish the X-ray map of the analyzed sample. This is the EDS mode (Energy Dispersive Spectroscopy). This mode establishes a distribution map of the elements present on a selected area. For this study, XL30 ESEM from the Laboratory of Physics and Chemistry of Materials (LPCM), university of Tizi Ouzou, was used for morphological characterizations (Figure II.4).



Figure II.4: SEM photography.

II.2.1.2 X-rays diffraction (XRD)

X-ray diffraction is a powerful nondestructive technique which is used for the characterization of crystalline materials. It provides information on phases, structures, preferred crystal orientations (texture), and other important structural parameters, such as crystallinity and average grain size.

X-rays are electromagnetic waves with wavelength ranging from 0.5 to 50 Å, comparable to the inter-atomic spacing in the crystal. They are directed on a solid material and can interact with the solid and scatter to produce a diffraction pattern. However, the scattered rays will become constructive only at a particular angle when the path difference between the two rays is equal to integer multiples of the wavelength. The necessary condition for this constructive interference is given by the Bragg's law:

$$2d_{hkl}\sin\theta = n\lambda \quad (\text{II.5})$$

where d_{hkl} is the distance between the atomic layers, θ the scattering angle and λ the incident X-ray wavelength. **Figure II.5** shows an illustration of Bragg's law for constructive interference.

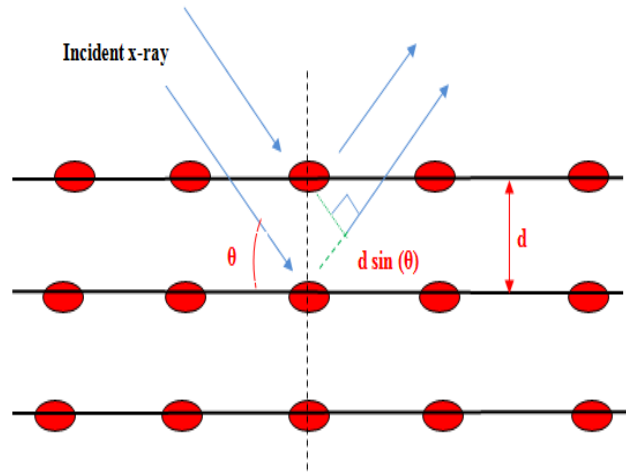


Figure II.5: Illustration of Bragg's law for constructive interference

XRD diagrams can be used to estimate the average crystallite size according to the Scherrer formula, which is given as follows:

$$t = \frac{0.9 \lambda}{\beta \cdot \theta_B} \quad (\text{II.6})$$

where t is the crystallite size, λ the incident X-ray wavelength and θ_B the Bragg angle. Broadening β is calculated by taking the full width half maximum (FWHM) of the diffraction peak corresponding to the plane in the diffraction pattern.

In this work, XRD measurements were carried out using a Rigaku Mini flex-II diffractometer, with $\text{CuK}\alpha$ radiation. The diffractograms were recorded in the 2θ range from 20° to 80° with a step of 0.01° . The obtained XRD peaks were identified using HighScore software.

II.2.1.3 Fourier transform infrared spectrometer

Fourier transform infrared spectrometer (FTIR) is one of the instruments based on infrared spectroscopy which offers various advantages including, high precision, accuracy, speed, enhanced sensitivity, ease of operation, and sample non destructiveness. Basically, an infrared spectrometer exposes the sample to infrared radiation with enough energy to induce the bonds in the molecule to vibrate. Each functional group has a distinctive frequency at which its

constituent bonds vibrate. FTIR spectroscopy can be used as a quantitative analytical technique, as well as to identify bonding processes in solids and on surfaces.

Figure II.6 shows the schematic diagram of FTIR. its principle is summarized as follows:

- An infrared energy beam emitted through a glowing black-body light source.
- The infrared beam is then directed into the interferometer, which generates the interferogram signal.
- After entering the sample compartment, the beam interacts with the sample, either transmitting through it or reflecting off its surface.
- The interference signal is captured as an interferogram, which is then decoded using the Fourier Transform mathematical technique.

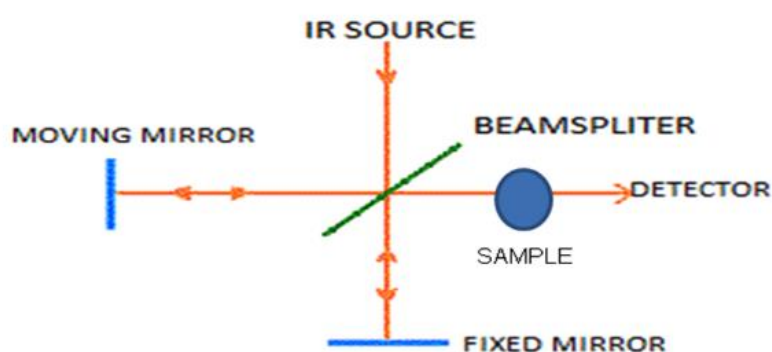


Figure II.6: Schematic diagram of FTIR for the sample analysis process [6].

In the present study, FTIR spectrometer (Shimadzu) from the faculty of science, university of Tizi Ouzou, was used in the $4000 - 1000 \text{ cm}^{-1}$ range, with a resolution of 4 cm^{-1} at room temperature.

II.2.1.4 Photoluminescence spectroscopy

Photoluminescence (PL) is a non-destructive optical method which is generally employed for the characterization and detection of point defects and impurity levels as well as for examining recombination mechanisms of charge carriers. The basic purpose is to measure the excitation and emission spectra.

PL is the process of irradiating a substance with photons and then collecting the response of the material. It always has at least two phases: the excitation of the substance's electronic system and its de-excitation, during which light emission occurs. Its process consists of three major steps (See Figure II.7):

- (1) Electrons excitation through the absorption of energy from external sources, which making them move to higher energy states. So, electron-hole pairs are generated.
- (2) Thermalization: Excited pairs relax towards quasi-thermal equilibrium distributions.
- (3) Recombination.

The used photoluminescence spectrometer in this work is Shimadzu RF-6000 fluorimeter equipped with xenon excitation source. The samples were monitored with two excitations of 325 and 410 nm.

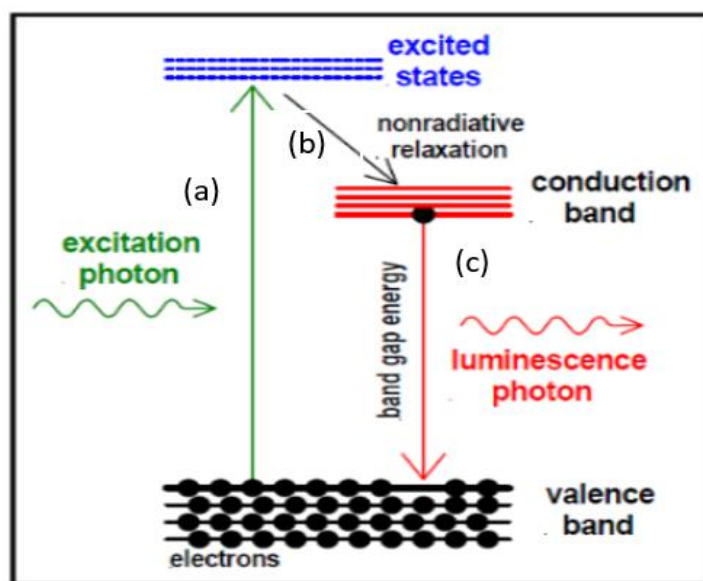


Figure II.7: Photoluminescence schematic. (a) promotion of the electron from VB to CB. (b) The electrons cool down to the bottom of the conduction band. (c) The electron recombines with the hole resulting in the emission of light with energy $h\nu$ [7].

II.2.1.5 UV-Visible spectroscopy and diffuse reflectance spectroscopy

UV-visible spectroscopy is a simple and fast method of analysis and characterization which provides information on the optical characteristics of materials. It allows the measurements of the optical density (absorbance) ($A = \log (1/T)$) and the transmittance ($T=I/I_0$) of a solid or liquid medium at different wavelengths, where I_0 is the incident light intensity and I is the transmitted intensity.

According to the Beer-Lambert Law, the absorbance is proportional to the concentration of the substance in solution. Thus, UV-visible spectroscopy can also be used to measure the concentration of a sample. The Beer-Lambert Law can be expressed as:

$$A = \epsilon_m cl \quad (\text{II.7})$$

where A is the absorbance, l the optical path length, i.e. dimension of the cell or cuvette (cm), c the solution concentration and ϵ_m the molar extinction, which is constant for a particular substance at a particular wavelength.

Diffuse reflectance spectroscopy (DRS) is very closely related to UV/Vis spectroscopy. The difference between the two techniques is that UV/Vis spectroscopy measures the relative change of transmittance of light as it passes through a solution, while diffuse reflectance measures the relative change in the amount of light reflected from a surface. In the present work, DRS was used to determine the optical properties of the synthesized materials, specifically the optical bandgap (E_g). The dependence between the photon energy and the optical absorption coefficient (α) is expressed by the following relation of Tauc model [8]:

$$\alpha \cdot hv = B(hv - E_g)^n \quad (\text{II.8})$$

Where hv is the energy of incoming photons, and B the Tauc coefficient describing the efficiency in light absorption. Depending on the direct and indirect transition behavior, the value of n is either 2 or $\frac{1}{2}$ respectively.

UV-vis diffuse reflectance spectra of the samples were collected in the of 200-800 nm range by using a Shimadzu UV-2501 spectrophotometer from LPCM of the university of Tizi Ouzou (Figure II.8 (a)), equipped with two sample holders. One suitable for liquids (Figure II.8 (b)) and another for solids (Figure II.8 (c)).

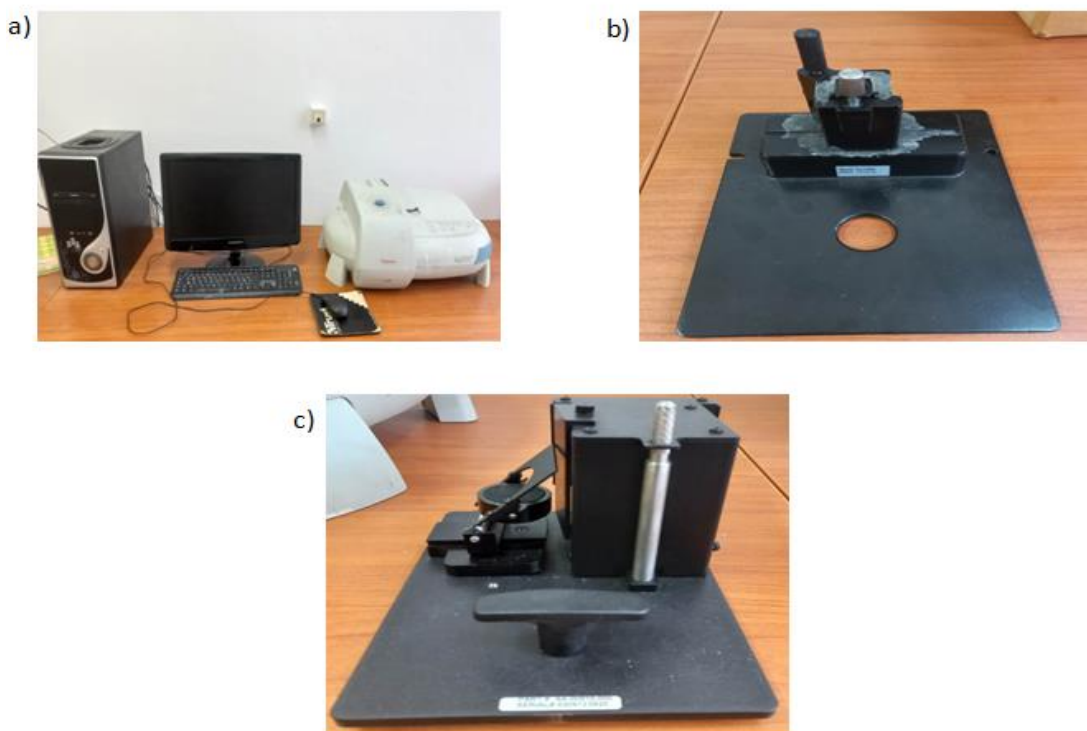


Figure II.8: (a) UV-Visible spectrophotometer (ISA-220) Photography, (b) aqueous solutions holder and (c) solids sample holder.

II.2.2 Electrochemical techniques

II.2.2.1 Cyclic voltammetry

Cyclic voltammetry (CV) is a potentiodynamic type of electrochemical measurements that is well known as a simple, rapid, and powerful method to obtain qualitative information about the electrochemical reactions and to determine the electrochemical performance of materials. CVs are often used to determine the redox potentials of the different redox couples present in the solution as well as to measure the intensity of the faradic current resulting from the electrochemical reaction (Figure II.9). The principle of this method consists in imposing a linear potential sweep with a constant speed. The potential is usually varied between the minimum and maximum electrochemical window of the electrode material. CV is a potential-controlled approach that typically employs a three-electrode system. The potential difference is used between the working and reference electrodes, and the current is monitored between the counter and working electrodes. CV employs a cyclic potential waveform, it is divided into two parts: forward and reverse sweeps. The forward sweep can be either anodic (growing potential) followed by a cathodic (decreasing potential) sweep, or cathodic followed by an anodic sweep [9].

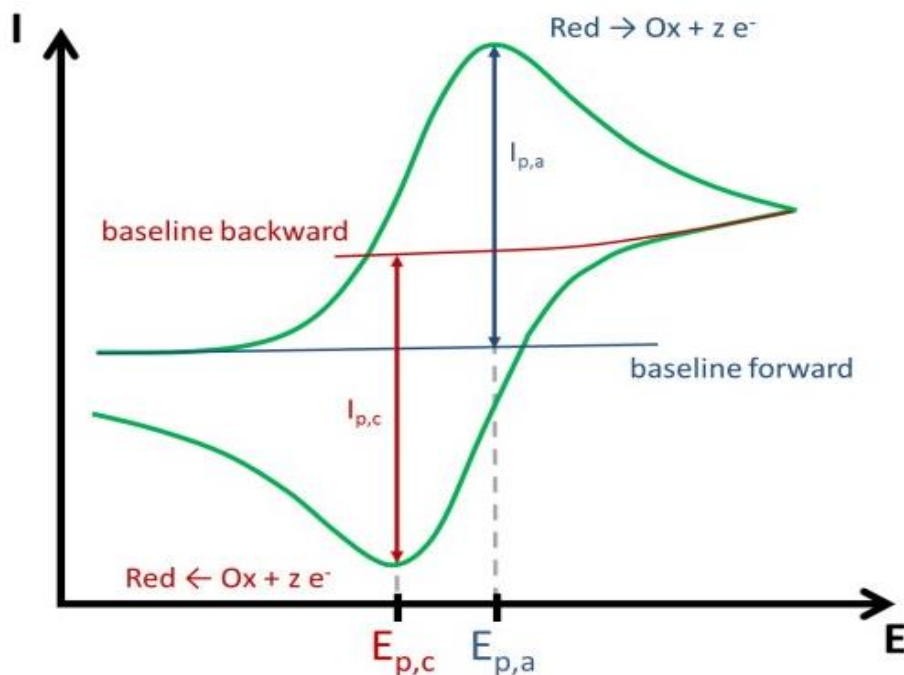


Figure II.9: A typical cyclic voltammogram showing anodic and cathodic peak currents.

II.2.2.2 Chronoamperometry

Chronoamperometry also known as a current transient technique is an alternative technique for film electrodeposition, it is one of the most methods for fabricating binary or ternary heterostructure materials. It is also used to study the kinetics of chemical reactions, diffusion processes and to obtain the initial information about nucleation and growth mechanisms of the studied systems. The principles of the electrodeposition process are based on principles of electrochemical phenomena associated with the reduction or deposition of electroactive species on the cathode in order to modify surface properties. For a metal (M) electrodeposition from an aqueous metal salt solution, the electric current is carried by the positively charged ions from the anode toward the negatively charged cathode, which means the polarization of the electrodes causes a migration of the metal ions towards the substrate. Finally, the metal ions are removed from the solution and are deposited on the surface in the form of metal (M) or metal oxide (M_xO_y). So, the reaction in aqueous medium at the cathode obeys the following equation:



Within the framework of this thesis, the electrochemical measurement setup (Figure II.10) used for the preparation of our heterojunctions is composed of an AUTOLAB PGSTAT30 potentiostat/galvanostat and an electrochemical cell containing the electrolytic solution and

three electrodes: the working “erelectrode, the reference electrode (Ag/AgCl) and the counter-electrode (a platinum foil). The potentiostatic mode was selected for the preparation of our deposits.

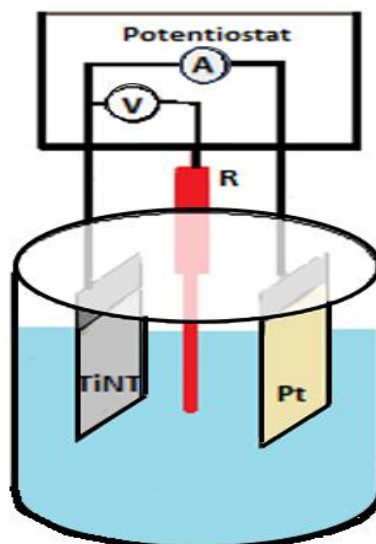


Figure II.10: Electrochemical setup used for electrodeposition.

II.2.2.3 Linear sweep voltammetry

Linear sweep voltammetry (LSV) is a simple electrochemical technique, similar to cyclic voltammetry. Instead of cycling linearly through the potential range in both directions, LSV involves a single linear potential sweep either in forward (anodic) or reverse (cathodic) direction. The recorded LSV characteristics are heavily influenced by the rate of the electron transfer reaction, the chemical reactivity of the electroactive species and the potential scan rate [10].

In this work, LSV was used to evaluate the photoelectrochemical properties of our samples.

II.2.2.4 Electrochemical impedance spectroscopy

Electrochemical impedance spectroscopy (EIS) is a powerful tool used for the analysis of interfacial properties in order to investigate electrode reactions and materials properties. EIS uses an AC signal over a different range of frequencies, which can be used to determine the impedance (Z) of the electrode material used in the electrochemical cell. The measurement approach typically consists of applying a sinusoidal voltage to the working electrode and to measure the current density response.

Thus, the excitation signal is presented as a function of time, as follows:

$$E_t = E_0 \sin(\omega t) \quad (\text{II.10})$$

where E_t is the potential at time t , E_0 the amplitude of the signal, and ω the radial frequency. In a linear system, the response signal, I_t , is shifted in phase (φ) and has a different amplitude than I_0 as demonstrated in the following equation:

$$I_t = I_0 \sin(\omega t + \varphi) \quad (\text{II.11})$$

The impedance Z of the system is defined by the following equation:

$$Z = \frac{E_t}{I_t} = \frac{E_0 \exp(j\omega t)}{I_0 \exp j(\omega t + \varphi)} = |Z_0| \exp(-j\varphi) \quad (\text{II.12})$$

The impedance expression is divided into a real part and an imaginary part:

$$Z = \text{Re}(Z) + \text{Im}(Z) \quad (\text{II.13})$$

There are two common ways of representing impedance data, the Nyquist Plot is formed when the real part is plotted on the X-axis and the imaginary part on the Y-axis (Figure II.11 (a)). Each point on the Nyquist plot is an impedance value at a frequency point. Bode plot is another way to express the impedance results, it comprises two separate logarithmic plots: magnitude vs. frequency and phase vs. frequency (Figure II.11 (b)).

The frequency analysis of the electrochemical impedance allows to differentiate the various elementary phenomena according to their characteristic frequency (or time constant). The fast electrochemical phenomena (charge transfer) are involved in the high frequency domain, while the slow phenomena (diffusion, adsorption....) occurred at low frequencies.

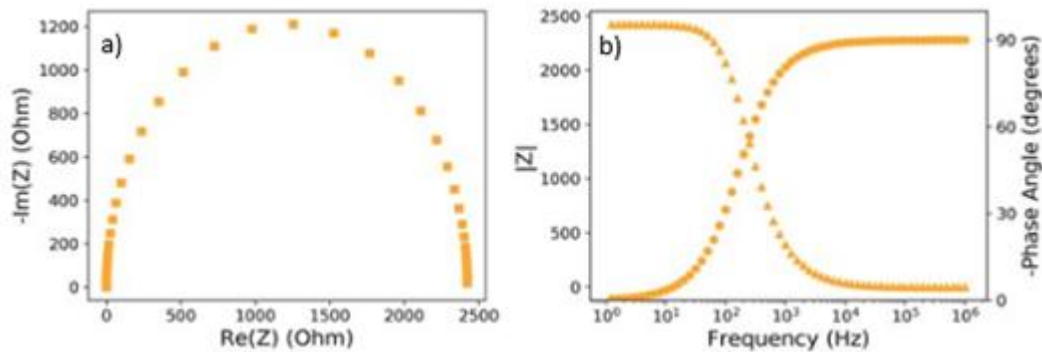


Figure II.11: a) Nyquist plot and b) Bode plot.

The objective of EIS is to associate the observable steps on the Nyquist and/or Bode diagrams to physical quantities. This can be approached by modeling the spectrum by proposing an equivalent circuit, composed of a number of simple elements; the most commonly used elements are: resistance (R), capacitor (C), inductor (L) and Constant Phase Element (CPE). CPE is applied to mimic/model the non-ideal capacitance behavior. The discussed reasons behind this include surface roughness, surface porosity and non-homogeneity of the investigated materials. The impedance of mass transmission is described by the Warburg impedance, it is based on the movement of reactants through the electrolytic solution and is most noticeable at low frequencies when diffusion dominates the electrochemical process sequence.

II.2.2.4.1 Mott-Schottky analysis

As stated before, band bending occurs at the SC/electrolyte interface due to the Fermi level difference. The consequent charge separation leads to the formation of a SCR on the SC side, the capacitance of the SCR (C_{sc}) can be used as a critical input for determining the electronic properties of the SC including charge carrier density and flatband potential. Mott-Schottky (M-S) technique is an EIS based technique which provides data on the relationship between applied potential (U) and C_{sc} at set frequencies. M-S equation is a common tool used for this purpose, it is valid in the depletion zone of the SC. The measured differential capacitance of the SCR with combining the Poisson and Boltzmann equations leads to the following M-S relationship:

$$C_{sc}^{-2} = \frac{2}{\epsilon\epsilon_0qN_qA^2} \left(U - U_{FB} - \frac{k_B T}{q} \right) \quad (II.14)$$

Where q is the electron charge (1.602×10^{-19} C), ϵ_0 the vacuum permittivity (8.85×10^{-14} F cm^{-1}), ϵ the dielectric constant, N_q the donor or acceptor density, k_B the Boltzmann constant (1.38×10^{-23} J K^{-1}), A the area and T is the absolute temperature.

N_q and U_{FB} are the most important parameters to characterize the SC/electrolyte interface. From the slope and the intercept with the potential axis of the C_{sc}^{-2} vs. U linear plot, N_q and U_{FB} can be determined respectively.

EIS measurements were carried out in 1M Na_2SO_4 solution by using the three-electrode system. The measurements were performed in a frequency range of 100 kHz to 10 mHz, with an AC perturbation of 10 mV at an open circuit potential and at an applied potential ranging

from -0.8 to 0.4V for M-S analysis. The control of the measurement parameters as well as their acquisition are managed by an acquisition card installed on a computer and driven by the software (FRA ECOCHEMIE LTD).

II.3 Methods for supercapacitor evaluation

Numerous techniques are used to characterize the performance of supercapacitors. Cyclic voltammetry, galvanostatic charge-discharge (GCD), and electrochemical impedance spectroscopy are the most commonly used techniques. The main important gained information from these techniques are specific capacitance (C_s), lifetime cycling, energy and power densities and equivalent series resistance (ESR).

Before examining the electrochemical characterization techniques used in this work, it is necessary to establish the difference between the two-electrode and three-electrode cells. Two-electrode measurements imply a complete measurement of the device, with two symmetrical electrodes. This two-electrode configuration is commonly employed to characterize the packaged cell, prototype supercapacitor device or fully fabricated devices. The three-electrode system consisting of a working electrode, a reference electrode, and a counter electrode is favorable for investigating the fundamental electrochemical properties of the electrode material system and is considered to be the most appropriate approach for examining the operating voltage.

II.3.1 CV measurements

The capacitive behavior of the supercapacitor device can be distinguished from the shape of the CV curves as shown in [figure II.12](#). Typically, ideal supercapacitors exhibit a rectangular shape CV curve ([Figure II.12 \(a\)](#)) with a constant current. However, the rectangular shape of CV curves can deviate due to the presence of Faradaic reaction. A quasi-rectangular behavior characterized by reversible current peaks are typical for pseudocapacitors ([Figure II.12 \(b\)](#)).

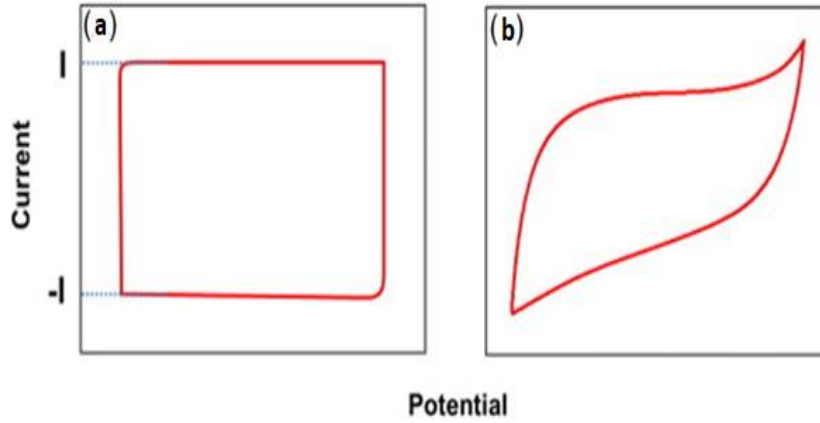


Figure II.12: Distinct shape of CV for (a) ideal and (b) pseudocapacitive type materials.

From the CV curves, the C_s of the electrodes can be calculated according to the following equation [11]:

$$C_s = \frac{\int IdV}{Sv\Delta V} \quad (\text{II.15})$$

where v is the scan rate (Vs^{-1}), ΔV is the potential window (V) and $\int IdV$ is the integrated area under the CV curve.

In the present work, CV measurements were performed in a three-electrode setup potential window from 0.2 to 1.2 V at different scan rates: 10, 20, 50, 100, 250, and 500 mVs^{-1} .

II.3.2 Galvanostatic charge-discharge (GCD) measurements

Cyclic charge-discharge is a standard technique utilized to investigate the electrochemical performance and cycle life of supercapacitors. One cycle constitutes the repetitive loop of charging and discharging between two potential limits upon applying a constant current (I). During the charging process Electrons go across an external circuit from the negative electrode to the positive electrode. In the electrolyte, anions travel toward the positive electrode whereas cations move in the other direction. The opposite processes occur during the discharge process.

Some typical galvanostatic charge-discharge plots are illustrated in [figure II.13](#). For an ideal supercapacitor, the charge and discharge curves are symmetrical (the charging and discharging processes are highly reversible) and exhibit a constant slope over the lifetime ([Figure II.13 \(a\)](#)). The C_s can be evaluated easily using the following equation [12]:

$$C_s = \frac{I}{\Delta V/\Delta t} \quad (\text{II.16})$$

where I is the magnitude of the applied current density and $\Delta V/\Delta t$ is the slope of the charge or discharge curve.

Supercapacitors do not always give such linear plots and the non-linearity may be indicative of a variety of non-idealities in the functioning of the supercapacitor. GCD curves can be distorted due to pseudo-capacitive behavior or instantaneous voltage drop (IR drop). **Figure II.13 (b)** illustrates one of these non-idealities. Decreases in the slope of the charge or discharge curve generally point to charge transfer across the electrode/electrolyte interface. This charge transfer arising from reactions in the electrolyte, electrode or both could contribute to pseudocapacitive charge storage. The second non-ideality is shown in **figure II.13 (c)**. The IR drop is due to the ohmic resistances of the system, which comprise the electrolyte resistance, the electrode resistance and all contact resistances (ESR).

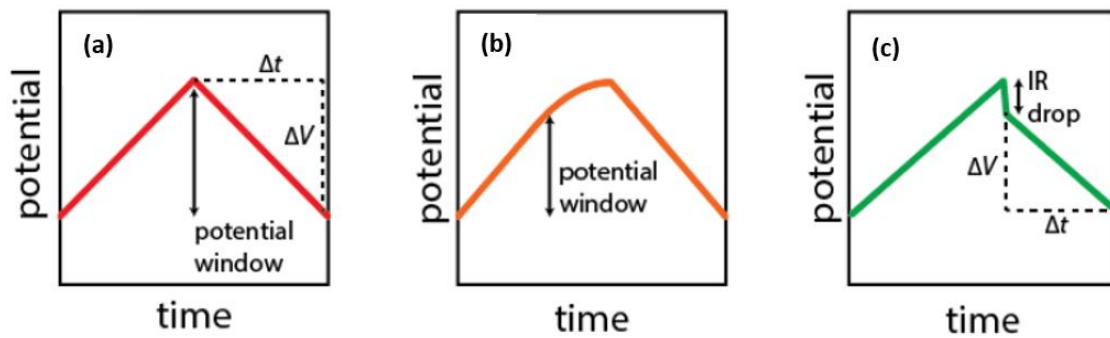


Figure II.13: GCD plots of: (a) an ideal supercapacitor, (b) and (c) non-ideal supercapacitors.

From the GCD curves it is possible to determine the amount of energy stored and the ability of a supercapacitor to be charged and discharged quickly, which corresponds to the specific energy density (E) and specific power density (P) respectively. These can be determined using the following equations [13]:

$$E \text{ (mWh cm}^{-2}\text{)} = \frac{C_s \times \Delta V^2}{7200} \quad (\text{II.17})$$

$$P \text{ (mWh cm}^{-2}\text{)} = \frac{3600 \times E}{\Delta t} \quad (\text{II.18})$$

In the present work, GCD plots were obtained over the potential of 1V at constant current densities of 5, 10, 30, 80 and 100 $\mu\text{A.cm}^{-2}$.

II.3.3 EIS measurement

EIS is a powerful tool to investigate the supercapacitor frequency behavior. Nyquist plot is a most commonly used representation for EIS. **Figure II.14** shows typical Nyquist plot

representations for charge storage materials. A pronounced capacitive behavior will correspond to vertical lines, parallel to the imaginary-axis, indicative of fast ion diffusion, with the absence of any resistive components. It is the characteristic feature of an EDL capacitor. The point intersecting the real axis of the impedance at the highest measured frequency gives ESR of the cell. 45° and 90° angle line regions with respect to the real axis of impedance are typical signatures commonly observed for the charge storage mechanisms of pseudocapacitive materials.

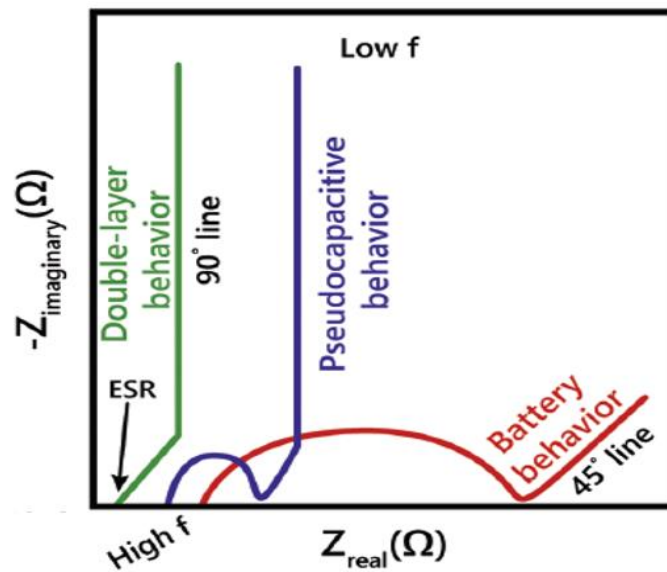


Figure II.14: Typical Nyquist plot representations for an EDLC, pseudocapacitive materials and battery.

EIS measurements were carried out in 1M Na₂SO₄ solution at an open circuit potential (OCP) by applying a small amplitude AC perturbation over a range of frequencies (10 mHz to 10 kHz).

II.4 Photoelectrochemical measurement

The photoelectrochemical effect corresponds to the transformation of the energy of photons absorbed by the system into electrochemical energy.

To examine the photoactivities of TiNT and engineered heterojunctions, photoelectrochemical measurements were performed in the same electrochemical setup described above. The different electrodes were subjected to illumination in 1M KOH (pH=13.6). The potential was swept from -1.5 to 1.5 V at a scan rate of 20 mV/s. A 450W xenon lamp was used as the visible

light source and a 125W mercury vapor lamp (HPR 125W (Philips)) was used as the UV light source (main line of emission, 365 nm).

Figure II.15 shows a scheme of the photoelectrochemical measurement setup. The photocurrent densities of the material electrodes were evaluated by LSV measurements.

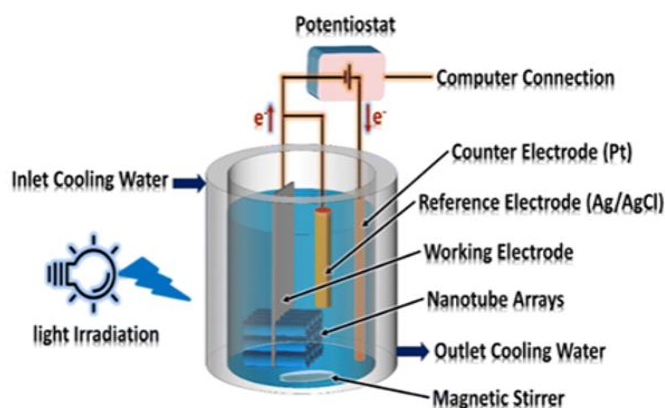


Figure II.15: Scheme of the photoelectrochemical measurement setup [14].

II.5 Photocatalytic tests

The photocatalytic activities of TiNT and modified TiNT materials were evaluated by degradation of the aqueous methylene blue (MB) dye under UV and visible light irradiations. The sample (1cm x1cm) was positioned in a quartz cuvette which is filled with 3 ml MB solution and irradiated with visible and UV light sources. The initial concentration of MB was 10 mg/L. The absorbance of MB at 663 nm was measured by a UV–Vis spectrophotometer. During decomposition, the concentration of MB was monitored every 10 minutes.

The experimental protocol used for the photocatalytic tests is shown in figure II.16 below.

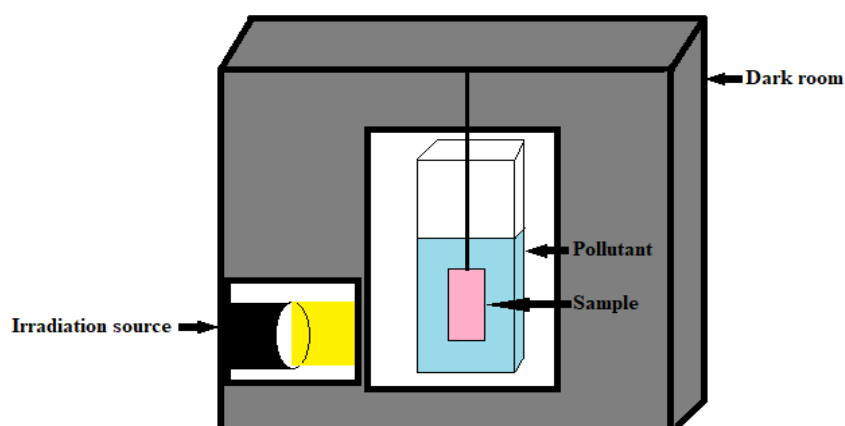


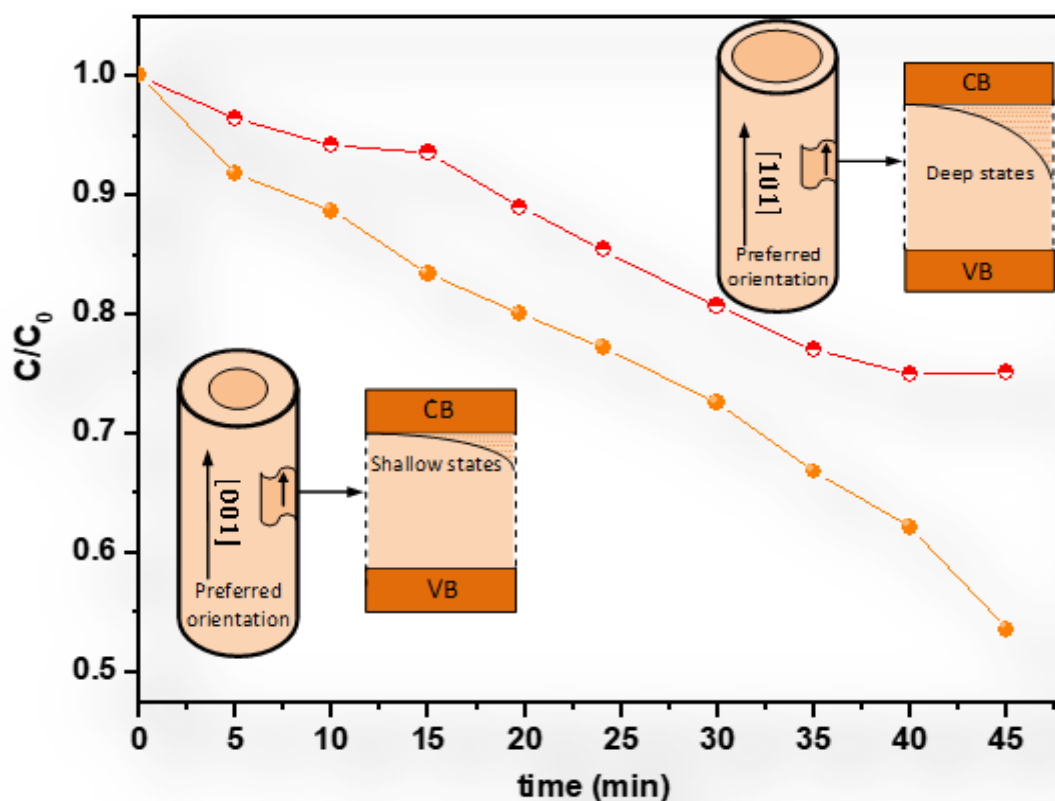
Figure II.16: Schematic representation of the experimental set-up used for the photocatalytic tests.

References

- [1] K. Indira, U. K. Mudali, T. Nishimura, N. Rajendran, *Journal of bio-and tribo-corrosion*, 1(2015)1.
- [2] J. M. Macak, H. Hildebrand, U. Marten-Jahns, P. Schmuki, *Journal of Electroanalytical Chemistry*, 621(2008)254.
- [3] J. M. Macak, H. Tsuchiya, A. Ghicov, K. Yasuda, R. Hahn, S. Bauer, P. Schmuki, *Current Opinion in Solid State & Materials Science*, 11(2007)3.
- [4] K. Lee, A. Mazare, P. Schmuki, *Chemical Reviews*, 114(2014)9385.
- [5] P. Roy, S. Berger, P. Schmuki, *Angewandte Chemie International Edition*, 50(2011)2904.
- [6] D. Kumar, B. Singh, K. Baudh, J. Korstad, *Algae and environmental sustainability*, (2015)87.
- [7] M. Vallikkodi, Doctoral thesis, University, Karaikudi, India, (2018).
- [8] R. Raciti, R. Bahariqushchi, C. Summonte, A. Aydinli, A. Terrasi, S. Mirabella, *Journal of Applied Physics*, 121(2017)234304.
- [9] J. F. Rusling, & S. L. Suib, *Advanced Materials*, 6(1994)922.
- [10] T. J. Davies, R. G. Compton, *Journal of Electroanalytical Chemistry*, 585(2005)63.
- [11] S. Pisana, M. Lazzeri, C. Casiraghi, K. S. Novoselov, A. K. Geim, A. C. Ferrari, F. Mauri, *Nature materials*, 6(2007)198.
- [12] R. Liu, W. Guo, B. Sun, J. Pang, and G. Zhou, *Electrochimica Acta*, 156(2015) 274.
- [13] Z. S.Wu, K. Parvez, X. Feng, K. Müllen, *Nature communications*, 4(2013)2487.
- [14] R. Habibi, N. Gilani, J. V. Pasikhani, A. E. Pirbazari, *Journal of Solid State Electrochemistry*, 25(2021)545.

Chapter III

TiO₂ nanotubes synthesis with dominant {001} exposed facets for efficient photocatalytic and photoelectrochemical water oxidation applications



Graphical abstract

Introduction

As stated before, to tune the optical and electrical properties of TiNT and in order to enhance their solar energy conversion efficiency, significant efforts have been performed to extend the absorption spectrum and to enhance the separation rate of the photogenerated electron-hole pairs.

Apart from altering their optical and electrical properties by the introduction of another material, engineering their crystal facets has been shown as a novel approach for extending the photoresponse towards visible light and for promoting the separation of photogenerated carriers. Crystal orientation has been reported to have a pronounced impact, as it can affect the process of electron-hole separation by surface arrangement [1, 2]. It is well known that each TiO₂ crystal facet possesses a distinctive intrinsic energy. Anatase TiO₂ crystals are mainly composed of {101} facets which are thermodynamically stable due to their low surface energy (0.44 J/m²). The growth of {100} facets dominated anatase TiO₂ requires 0.53 J/m². Whereas, that of {001} facets is thermodynamically unfavorable due to their higher surface energy (0.90 J/m²) [3-5]. Theoretical and experimental investigations have demonstrated that {001} facets of anatase TiO₂ are considerably more reactive than {101} facets, which may constitute the dominant source of active sites for several applications such as photovoltaic cells, photocatalysis and water splitting [6, 7]. TiNT with dominant {101} facets have been produced and have showed enhanced photocatalytic oxidation activity [8, 9]. Moreover, it was found that the photocatalytic activity of TiNT, assessed by monitoring the photodegradation of rhodamine B, increases with increasing exposure of {001} facets, suggesting that highly energetic {001} facets boost the photocatalytic activity of large-scale TiNT [10]. Ding et al. [11] and Roy et al. [12] systematically investigated the influence of different exposed facets on the photocatalytic activity of anatase TiO₂ for methyl orange (MO) degradation. The results indicated that, among the different facets, {101} was the least active towards MO degradation, whereas an optimum {101}/{001} ratio resulted in excellent performance. Similar conclusions were drawn by Han et al. [13], using MO as target pollutant in aqueous solutions, they confirmed that anatase TiO₂ nanoplatelets with dominant {001} facets significantly improve the photocatalytic reactivity for the oxidation of organic pollutants, with both catalytic efficiency and stability, making these materials desirable for high-level water purification. Furthermore, hydrogenated {001}-facet-dominant TiO₂ nanocrystals were reported to be more active in photocatalytic hydrogen evolution than the hydrogenated TiO₂ nanocrystals with {101} and {100} facets [14].

Despite the general agreement on the enhancement of photocatalytic reactivity by appropriate engineering of crystal facets, there remain controversial viewpoints on the role of {001} facets in attaining the superior photoreactivity of {001} facet-dominated TiNT. Some authors attributed the improved photoreactivity to the different energy levels of the conduction and valence band edges of the different facets, leading to an efficient surface heterojunction [15, 16]. Others to the charge transport improvement and higher reactivity rate [17, 18].

In contrary to particulate TiO₂ crystals with dominant {001} facet [19, 20], which were mainly synthesized by hydrothermal and/or solvothermal processes, anatase TiNT with high exposure degree of the reactive facets {001} have been less reported. Indeed, surface fluorination under acidic conditions is a common way to reduce markedly the {001} faceted surface energy and thus preserving the as-grown facets [21]. Lee et al. [10] have reported that the optimization of the quantity of hydroxyl groups, i.e. water content in the electrolyte in as-grown nanotubes seems to be one of the critical factors in fabricating preferred oriented TiNT. According to them, the water content had to be controlled carefully, 2% of water was the optimal content for (004) preferred oriented TiNT. In fact, in an electrolyte of only 2 wt% of water, low dissolution of the fluoride species is occurring. Upon annealing, the commonly volatile fluoride species may be trapped in the porous structure of TiNT, acting as a capping agent that stabilizes the {001} facets at the temperature of crystallization. More extensive surface Ti–F bonding can play a major role in achieving higher percentages of {001} facets in anatase TiO₂ [22].

In addition to low water content (2 wt%), fluoride content in the electrolyte has been also reported to be a key factor in producing (004) preferred oriented TiNT [23]. To further improve the degree of exposure of the {001} facets, NH₄F was utilized as a capping agent during the anodization and the evolution of TiNT was modified by varying the anodization time and NH₄F concentration. Increasing the first anodization time (up to 11 h) and/or NH₄F concentration leads to an increase in the exposed {001} facets [2]. Consequently, crystallization time affects the preferred orientation degree of TiNT, which is also in agreement with the main conclusions drawn by Pang et al. [24].

Inspired by the above results and viewpoints, in the present work we have tried to prepare TiNT arrays with mixed exposed {101} and {001} facets by two step anodization process, by adjusting the fluoride and water contents as well as the anodization potential. Photoactivity experiments have revealed that photocatalytic and PEC water oxidation efficiencies increase mainly with the increase of the degree of exposure of {001} facets. The separation efficiency

of photogenerated electrons and holes were investigated using photoluminescence spectra, electrochemical impedance and onset photocurrents. More importantly, deep and shallow gap states distribution in the bandgap of TiNT, which depend on the atomic surface arrangement, play an essential role in the electronic transport and performance of the photoelectrodes. Therefore, electronic properties, including gap states quantification (density and location) of TiNT were determined and correlated to their crystalline orientation. To the best of our knowledge, this kind of study has never been reported on TiNT exhibiting different atomic surface arrangement.

III.1 Two-step anodization TiNT synthesis procedure

Prior to anodization, titanium foils were polished with 400, 600, 1000 and 1200 SiC grinding paper. Titanium foils were then degreased in an ultrasonic bath with acetone and finally rinsed with de-ionized water and dried. Electrochemical anodization of titanium was achieved with a two-electrode configuration described in the previous chapter.

TiNT with mixed exposed facets were fabricated by two-step anodization approach by adjusting the potential and the concentration of F^- and water. The anodizing bath was: Ethylene Glycol + 0.27 M NH_4F + 2 wt% H_2O .

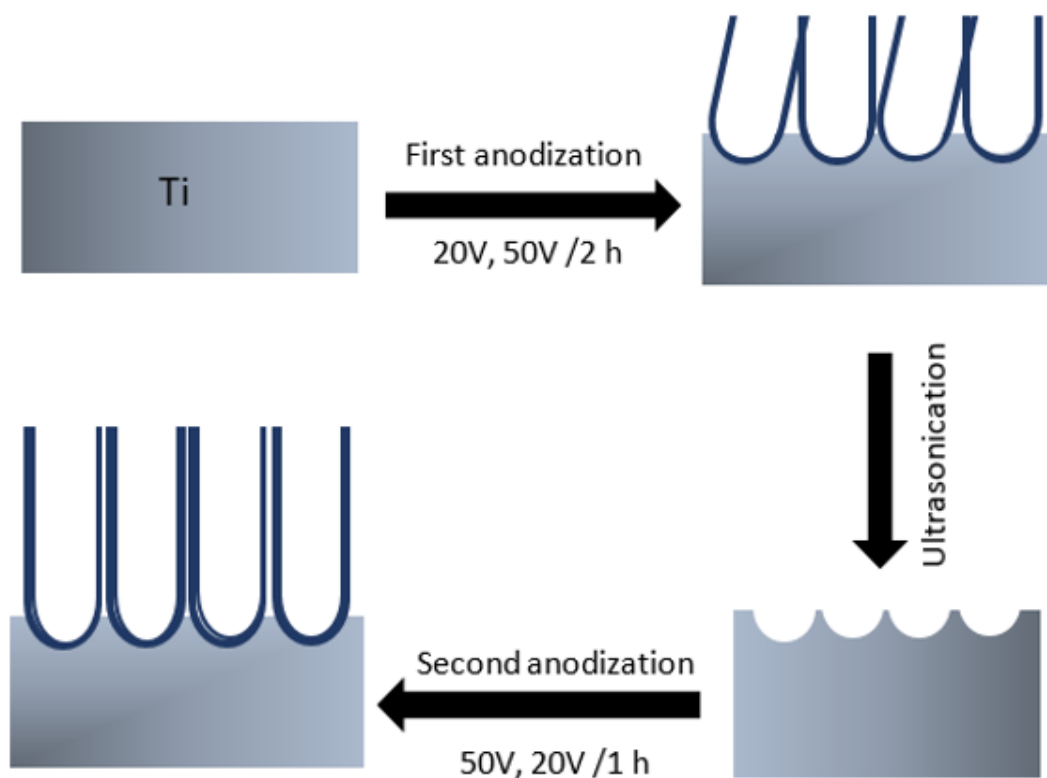
The two-step anodization method consists of removing the layer of nanotubes produced in the first anodization step by ultrasonic treatment. This step results in the production of regular shaped imprints suitable for a second anodization step for the subsequent growth of high order nanotubes. Obviously, the imprints or dimples play the role of nuclei for the growth of nanotubes.

For the two-step anodization approach, two sequences were used:

- (i) From 50V to 20V: the first anodization was performed at 50V during 2 hours and the second one at 20V during an hour.
- (ii) From 20V to 50V: in this case, the first anodization was performed at 20V during 2 hours and the second one at 50V during an hour.

The resulting samples are designated as 50V/20V TiNT and 20V/50V TiNT respectively.

Scheme III.1 shows the fabrication procedure of the TiNT by the two-step anodization.



Scheme III.1: A Two-step anodization to grow high-aspect-ratio TiNT.

TiNT with exposed (101) facets were also synthesized, in the same anodizing bath, by one step anodization at 50V during 2 hours and serve as a reference.

The as-anodized nanotube arrays were then subjected to thermal annealing at 450°C to achieve the pure anatase phase.

III.1 Morphological and structural analysis

SEM micrographs in [figure III.1 \(a-c\)](#) show low magnification SEM surface morphologies of TiNT samples synthesized by one-step (50V during 2 hours) and two-step anodization processes. As can be seen, relatively clean top surfaces are obtained over large area. A fully developed TiO₂ with nanotubular structure are obtained. The average wall thicknesses are 27, 23 and 31 nm for TiNT formed at 50V, 20V/50V TiNT and 50V/20V TiNT respectively.

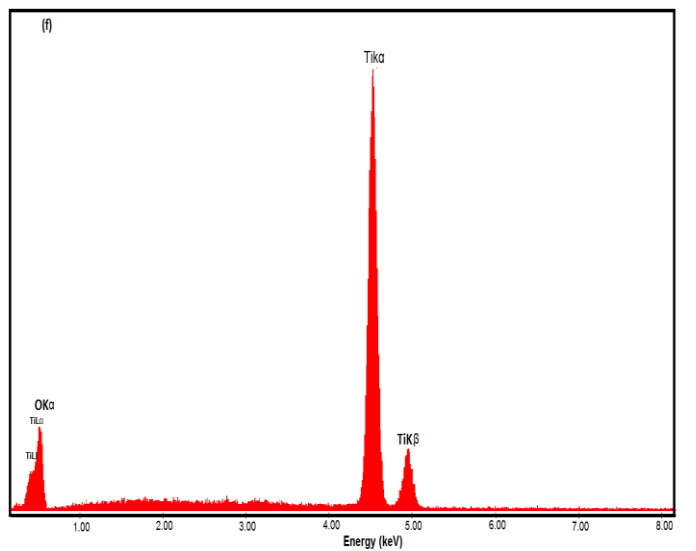
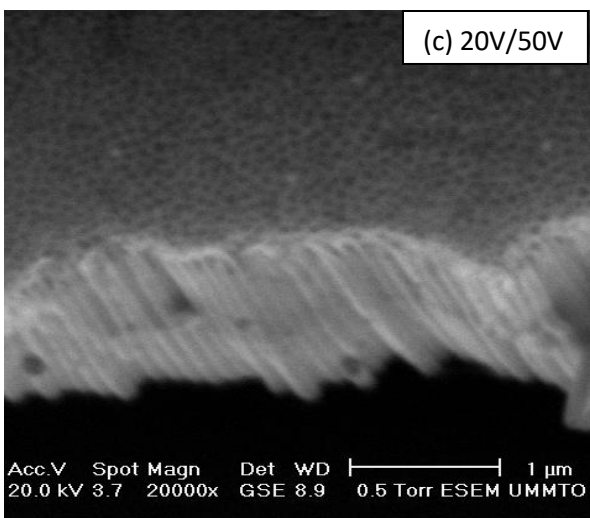
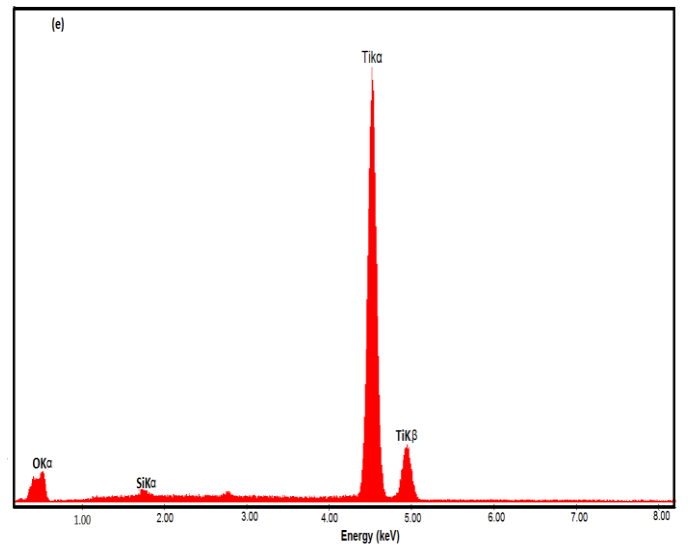
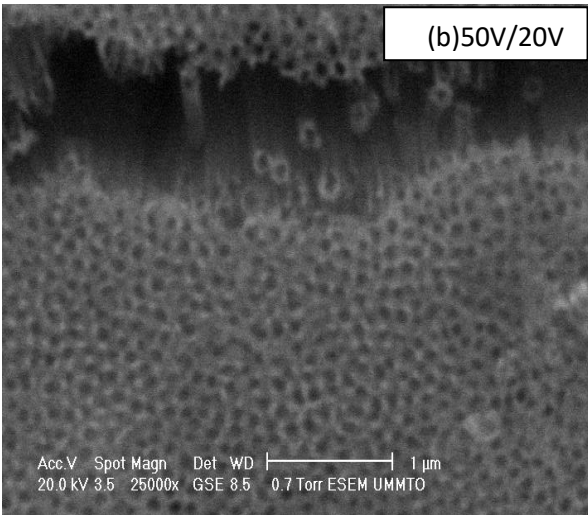
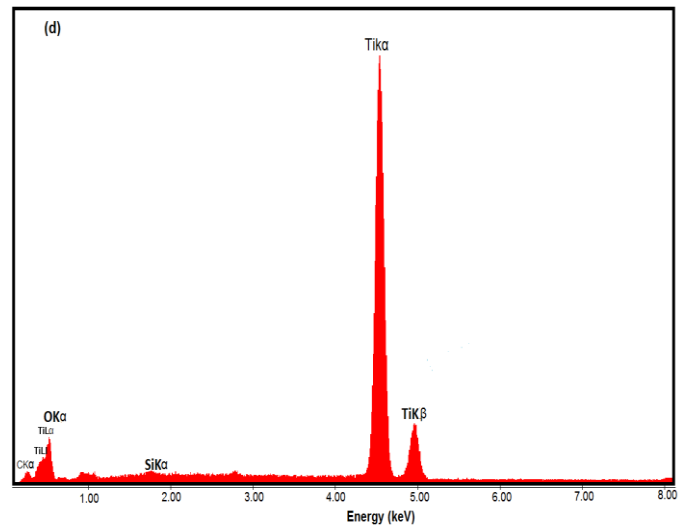
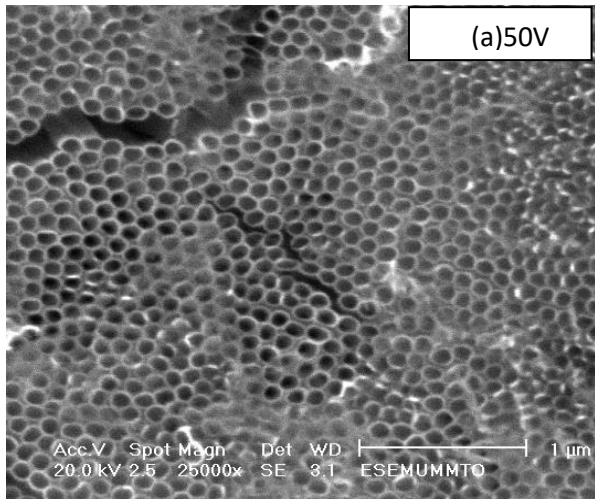


Figure III. 1: SEM images of (a) TiNT grown at 50V, (b) TiNT grown at 50V/20V and (c) TiNT grown at 20V/50V in a solution containing Ethylene glycol + 0.27 M NH_4F + 2 wt% H_2O .

TiNT formed at 50V exhibit higher inner diameter (~119 nm) and longer tubes (~8 μm). An elemental analysis was carried out by using the energy dispersive X-ray spectroscopy (EDS). The presence of TiO_2 nanotubular layers is revealed by the peaks at 0.5 keV for O as well as at 4.5 keV and 4.9 keV for Ti (Figure III.1 (d-e)).

XRD was used in this study to evaluate the crystallinity and preferred crystallite orientation of the different materials. As shown in the XRD patterns in figure III.2, the only crystalline phase present in the films is anatase. The films are polycrystalline in nature. The main diffraction peaks from anatase TiO_2 can be detected at $2\theta = 25.5^\circ$, 37.8° , 48.2° , 54.2° and 55.2° which correspond to (101), (004), (200), (105) and (211) respectively (JCPDS card No.21-1272). The patterns of Ti substrate are in good agreement with the Ti (JCPDS No.44-1294).

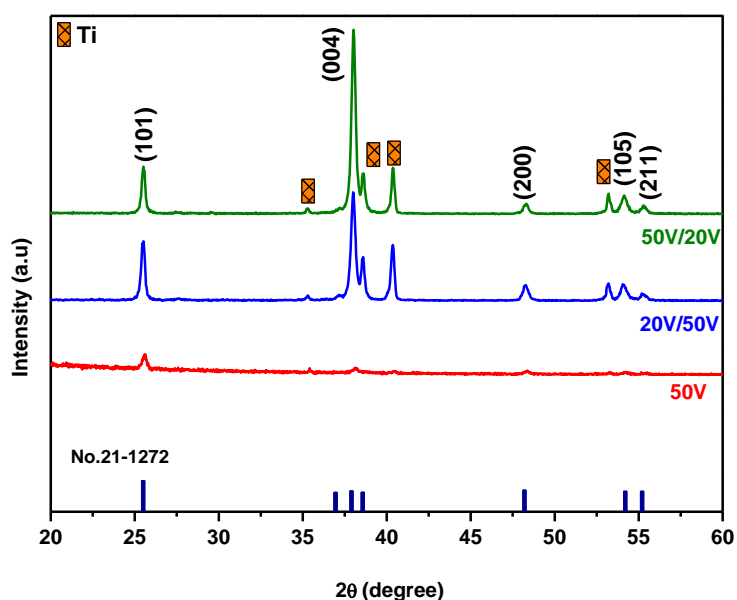


Figure III.2: XRD patterns of the different materials.

The crystallographic structure was significantly different between the formed TiNT. The intensities of the anatase peaks related to TiNT formed by two step anodization are higher than that of one step anodization, suggesting higher crystalline properties of these arrays. Besides, the most intense peak for anatase depends on the growth conditions of TiNT. TiNT formed at 50V shows less crystallinity, the only marked peak of anatase is the one corresponding to (101) plane, indicating that TiNT formed at 50V are preferentially oriented along (101) plane. 20V/50V TiNT and 50V/20V TiNT display preferred orientation with (004) peak which

correspond to the {001} facets of anatase TiO₂. This puts forward a preferential growth of these TiNT along the anatase [001] direction.

The relative intensity and the preferred orientation degree trend of the materials can be evaluated by calculating the ratio of peak intensity of (004) plane to (101) plane (I_{004}/I_{101}) and (004) plane to (200) plane (I_{004}/I_{200}). The relative intensities showed values ranging from 4.06 to 0.37 for I_{004}/I_{101} and from 18.8 to 5.87 for I_{004}/I_{200} (see **Table III.1**). Average crystallite sizes of 31.4 and 35.4 nm were found for 20V/50V TiNT and 50V/20V TiNT respectively using Scherrer formula by analyzing the peak broadening in the (004) peak at 37.8°. One may notice that 50V/20V TiNT shows higher relative intensity and higher crystallite size. The observed trends suggest that the degree of the {001} preferred orientation and crystallite size depend on the anodization potential. Because (004) peak is practically undetected for TiNT grown at 50V in the same controlled electrolyte (2% of water and 0.27 M NH₄F), it is so reasonable to conclude that in our conditions, the preferred oriented TiNT cannot be obtained only by adjusting the water and fluoride contents of the anodizing solution. One may speculate that in addition to these two key factors, the second anodization potential plays an essential role in the formation of TiNT dominated by the highly reactive {001} facets. This is may be related to the optimal presence of F⁻ ions and optimal voltage which stabilize the (001) surfaces.

Applied voltage (V)	50	20/50	50/20
I_{004}/I_{101}	0.37	2.19	4.06
I_{004}/I_{200}	/	5.91	18.85
Crystallite size based on (004) plane (nm)	/	31.4	35.8

Table III.1: Ratios of peak intensities of (004) plane to (101) plane and (004) plane to (200) plane of the TiNT formed at different anodizing conditions.

III.2 Electronic characterization of the materials

Interfacial capacitance measurements have usually been used for the characterization of semiconductor oxides [25]. In the present study, Mott-Schottky (M-S) plots were first carried, aiming to gain information on the charge transport and electronic properties of the different materials.

Figure III.3 (a-c) illustrates M-S plots of the different materials at a frequency of 1 kHz. Since the M-S plots are difficult to discern in the same figure, the curves are plotted separately. As

can be seen, all the curves show the occurrence of two positive linear parts (M-S behaviour), reflecting n-type semiconductor behaviour.

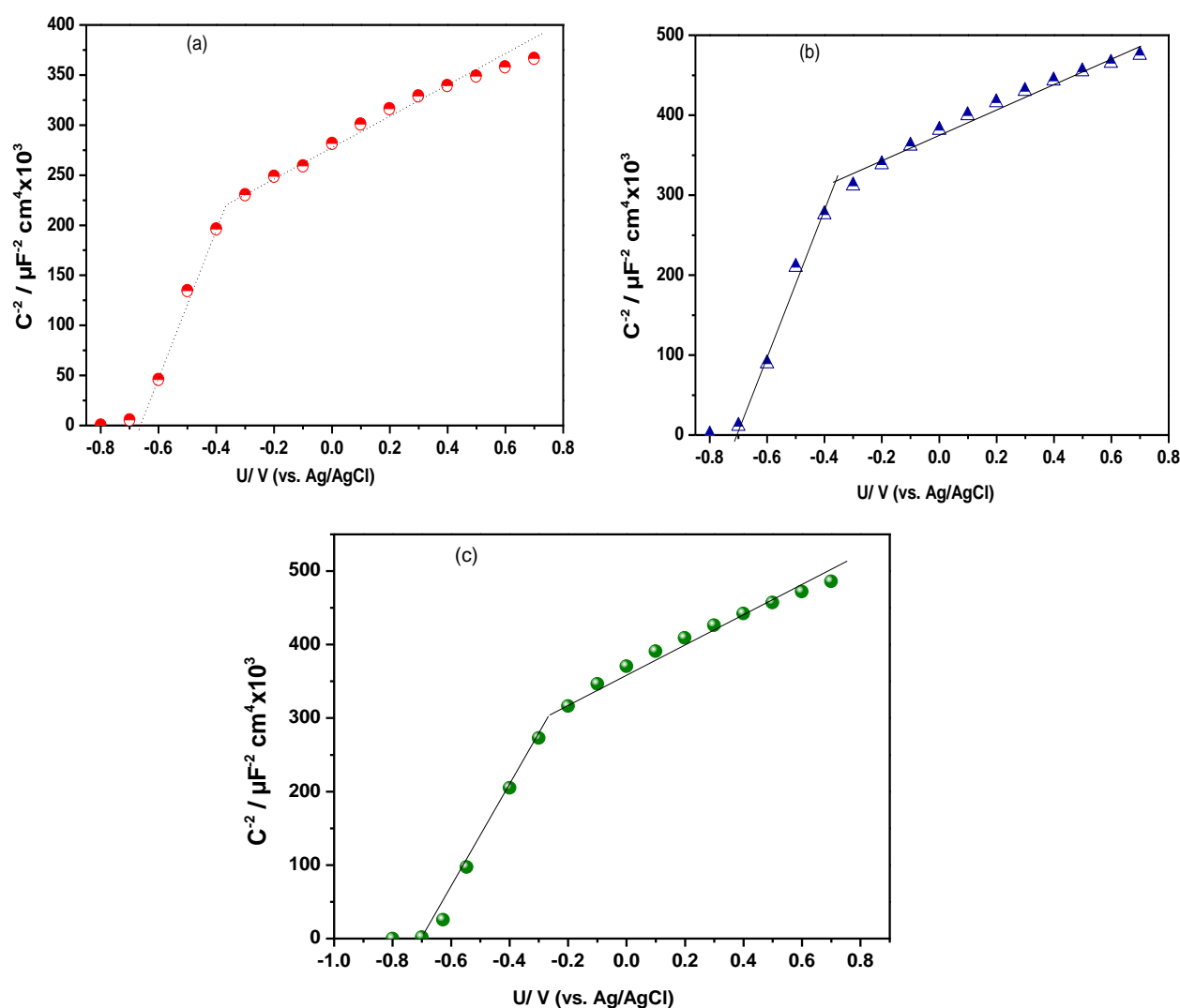


Figure III.3: M-S relationships of the different materials at a frequency of 1 kHz ((a): 50V, (b): 20V/50V and (c): 50V/20V).

M-S plot of TiNT formed at 50V (**Figure III.3 (a)**) shows the occurrence of two distinct linear parts. Such deviations from linear relationship are frequently attributed to the influence of potential dependent charging of surface or bulk states. So, the appearance of two slopes in the M-S plots may be related to the presence of both shallow and deep level donor species. Both the shallow and the deep levels of donor states contribute to the electrode capacitance. The potential at which these changes in slope occur reflects the energy level of the deep-level states [26], which is about -0.4V for TiNT prepared at 50V and for 20V/50V TiNT (**Figure III.3 (b)**), whereas it is around -0.3V for 50V/20V TiNT (**Figure III.3 (c)**).

The doping densities N_{D1} at shallow levels of the samples can be determined from the slopes of the first linear sections. Donor density values are about 2.35×10^{18} , 1.8×10^{18} and $1.6 \times 10^{18} \text{ cm}^{-3}$ for TiNT formed at 50V, 20V/50V TiNT and 50V/20V TiNT respectively.

Defect gap states are of particular relevance for PEC and photocatalytic applications, nevertheless, to the best of our knowledge, correlation between the crystallinity, the ratio of exposed {001} facets and the defect gap states quantification (density and location) has never been or rarely reported. In the present investigation, we aim to correlate photo-induced gap states properties with the TiNT dominated exposed facets. For this purpose, electrochemical impedance spectroscopy measurements were carried out after 3 hours UV illuminated TiNT. Impedance diagrams in Bode representation are shown in **figure III.4 (a-c)** for some potentials only.

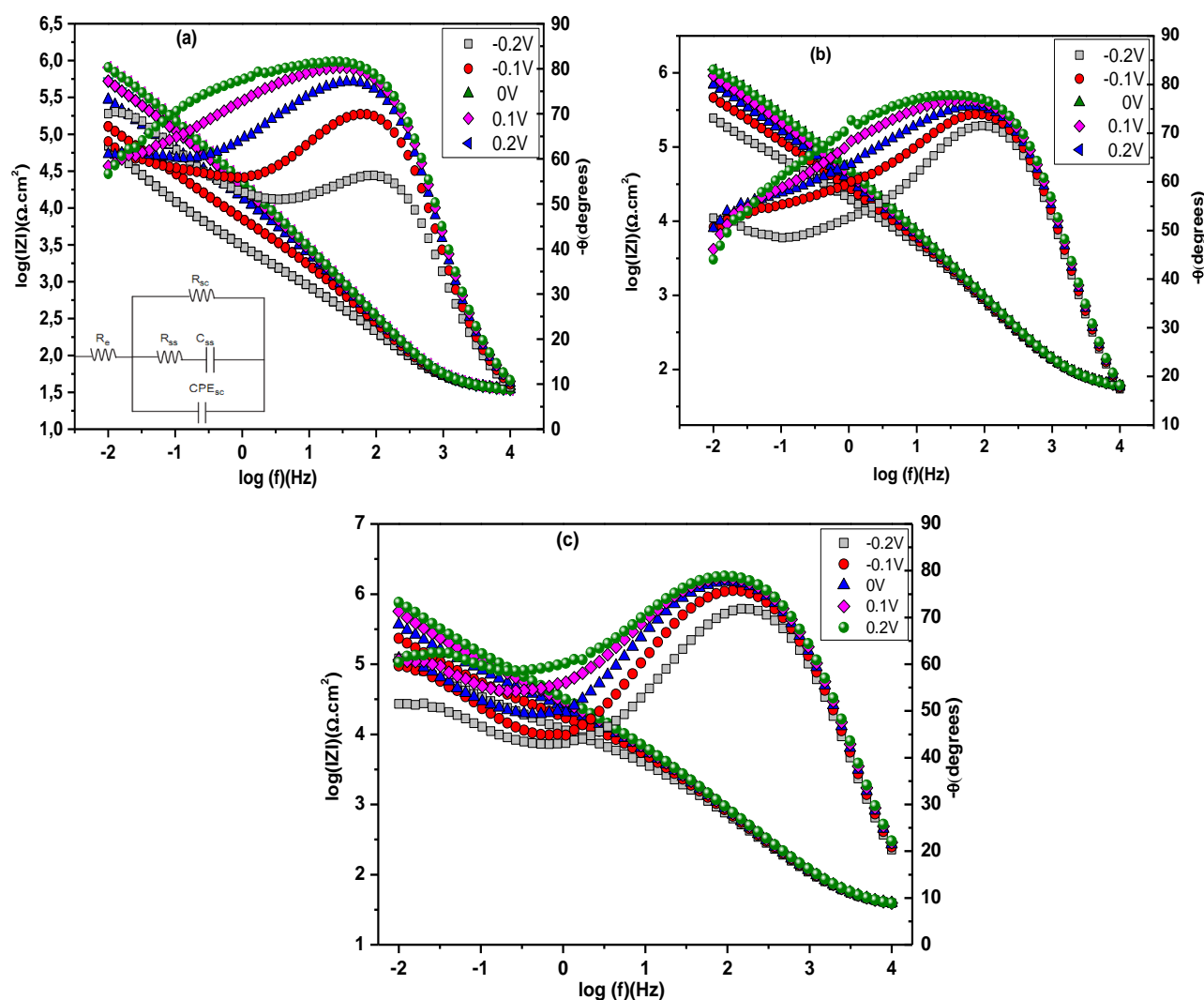


Figure III.4: Bode representation of TiNT electrodes after 3h of UV illumination ((a) TiNT grown at 50V, (b) 20V/50V TiNT and (c) 50V/20V TiNT).

Impedance data collected across the interfaces exhibited two time constants over the examined range of potentials. These plots show an increase of impedance modulus and phase magnitude with applied potential. TiNT formed at 50V showed particularly a remarkable increase.

To model the responses of TiO₂ films after illumination, the equivalent circuit illustrated at the insert in figure III.4 (a) is used. This circuit takes into consideration the resistances and capacitances associated with space charge layer of the oxide and surface gap states. R_{ss}-C_{ss} and R_{sc}-CPE_{sc} circuits are arranged in parallel, which signifies that gap state filling and band bending in the space charge layer of the oxide happen simultaneously.

The gap states capacitance (C_{ss}), corresponding to the response of some long lasting gap states, as a function of applied potential is an efficient way to characterize the gap states of TiNT. The dependency of the surface gap state capacitance on applied potential is illustrated in figure III.5 below.

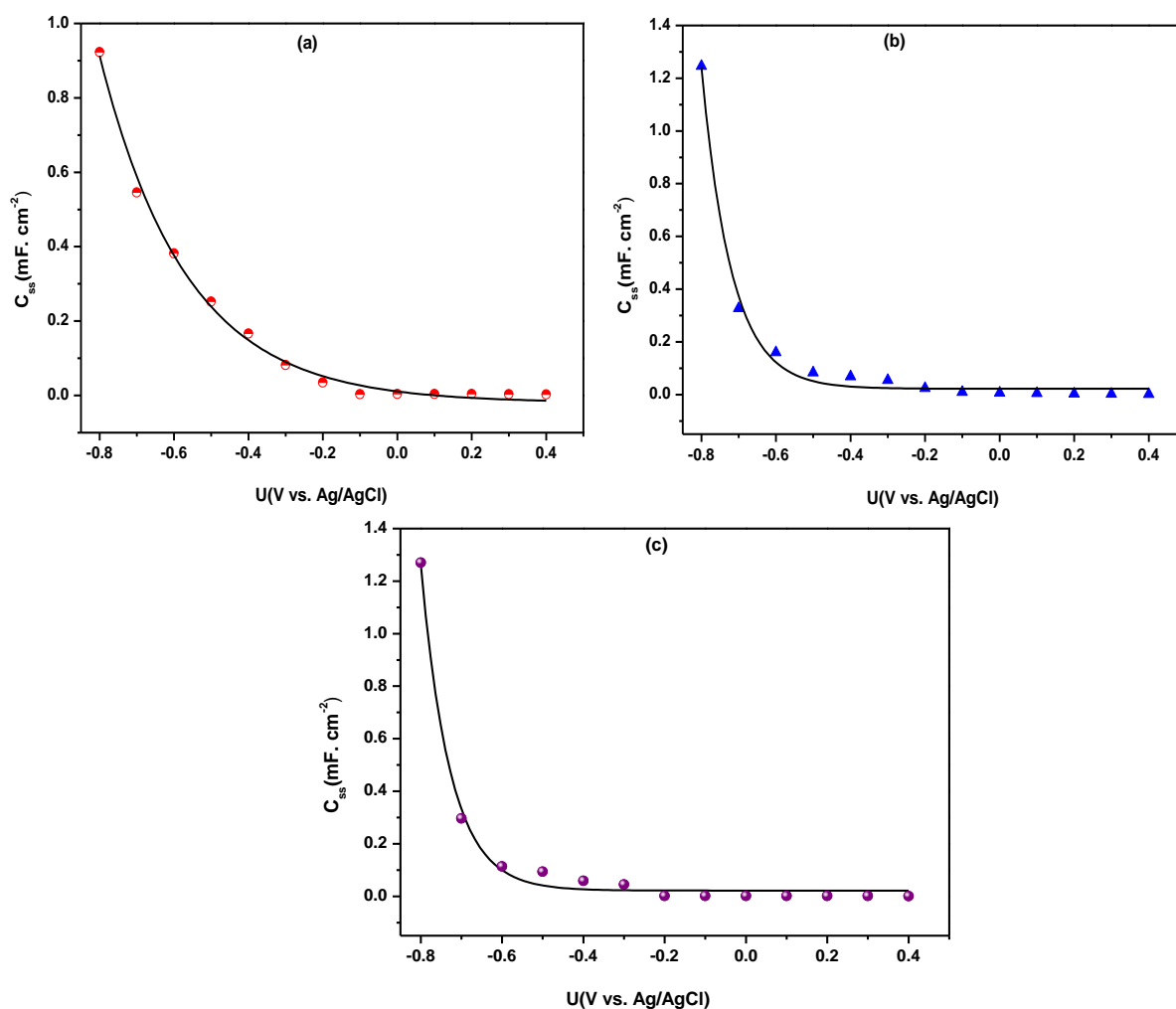


Figure III.5: Variations of the gap state capacitance (C_{ss}) as a function of the applied potential for TiNT electrodes after 3 hours UV illumination ((a): 50V, (b): 20V/50V and (c): 50V/20V).

As can be seen, the capacitance decreases exponentially with applied potential for each sample, which highlights the presence of an exponential surface gap states distribution. Otherwise, gap states can continuously extend from the band edge into the gap.

Capacitance voltage (CV) relationship, according to the exponentially localized states distribution is given as follows [27]:

$$C_{ss} = \frac{N_L q^2}{k_B T_0} \exp\left[\frac{E-E_c}{k_B T_0}\right] + C_b \quad (\text{III.1})$$

where N_L is the total density of localized gap states, E_c the energy of the lower edge of the conduction band, C_b the quasi constant capacitance at lower potentials and T_0 a characteristic temperature that defines the broadening of the exponential distribution, i.e. the parameter controlling the depth of a gap state distribution.

The broadening can otherwise be described by the coefficient $\alpha = \frac{T}{T_0}$. Smaller α means a deeper distribution of gap states.

For a better comprehension of the sample behaviours, simulated plots were computed assuming an exponential distribution of gap states. The experimental and simulated curves are superimposed in the same figure as it is shown. T_0 evaluates the concentration and energetic location of electronic gap states in the considered materials, N_L and T_0 parameters are obtained by fitting the experimental data and are presented in **Table III.2** bellow.

Anodisation potential (V)	T_0 (K)	N_L (cm ⁻²)	α
50	2714.6	4.4x10 ¹³	0.11
20/50	928.07	2.83x10 ¹⁰	0.32
50/20	835.26	8.5x10 ⁹	0.36

Table III.3: gap states characteristics of TiNT electrodes after UV exposure.

The CV responses analysis revealed a strong dependence of gap state characteristics on the crystallographic orientation of the films. Both gap states density and location strongly depend on the crystallinity and preferred orientation of the materials. α values of 0.11–0.36 were found according to the (101) degree of exposure. Higher α value was found for the 50V/20V TiNT, exhibiting higher percentage of (001) surface. Higher α value means a shallower distribution of gap states. The total density of gap states (N_L) for this sample is about 8.5x10⁹ cm⁻² only. In contrast, higher total density of states was obtained for TiNT formed at 50V, displaying poor

crystallinity and higher ratio of (101) surface, it is about $4.4 \times 10^{13} \text{ cm}^{-2}$. Lower α value of 0.11 obtained for this sample means long-lasting charge carriers most probably due to deeper gap states. Deep gap states may lie deep within the band gap; these gap levels are also called trap levels because they are traps for charge carriers.

A simple analysis of the above results suggests that deeper gap states are found on the (101) surface, whereas shallow gap states and/or lower deep states are predominately found on (001) surface. Interestingly, the density of these shallow gap states decreases with increasing the ratio of the exposed (001) surface.

The exact nature of these defect states is largely unclear and a matter of debate, they may originate from incompletely coordinated Ti^{3+} sites, Ti^{4+} and surface OH groups.

The above results corroborate previous works, which report that shallow gap levels are found on the anatase (001) surface [28]. Whereas, a deep gap states are observed on anatase (101) exposed surface [29].

III.3 Optical properties

III.3.1 Photoluminescence analysis

The photoluminescence emission spectrum has been extensively used to investigate the electronic structure and optical properties of semiconductor materials. Most importantly, it has been used to elucidate the nature of defect states and to examine the efficiency of charge carrier trapping, migration and charge transfer. Besides, PL intensity quantifies the recombination efficiency of photogenerated charges, that represents the mainly important limiting factor for many applications.

PL spectra of the synthesized materials monitored with excitations of 325 and 410 nm are illustrated in figure III.6. Because PL peaks of TiNT are indiscernible in the same figure, so they are plotted separately (Figure III.6 ((b) and (d))). As can be seen, all of the materials exhibited similar line shapes. Positions of the PL peaks are almost the same with differences in intensity. The films display several emission bands which are located at 375, 394, 450, 465, 480, 590 and 525 nm with an excitation of 325 nm. With an excitation of 410 nm, the emission bands are centered at 440, 465, 480, 490, 566 and 610 nm.

In general, two types of transitions contribute in the PL intensity. The first one is called excitation emission; it concerns the electron transitions from the conduction band to the valence band (band-to-band transition), and possesses the wavelength belonging to the UV light region. The emission peak around 375 nm ($\sim 3.2\text{-}3.3 \text{ eV}$) is close to the band-edge emission of TiO_2 , whereas, the emission band at 394 nm (3.14 eV) was found to be the excitonic emission [30].

The second type of transitions concerns the electron transitions from the defect energy level to the valence band and possesses the wavelength belonging to the visible light region. These emissions are attributed to three kinds of physical origins: (i) self-trapped excitons (STE), (ii) oxygen vacancies, and (iii) surface states [31, 32]. The emission peak at 440 nm may be related to STE located on the TiO_6 octahedra. Emission peaks positioned at 450-465 nm (2.76-2.66 eV) are generally linked with the shallow and deep surface traps associated with Ti^{3+} states [33, 34]. The emission peak at about 490 nm (2.53 eV) has been believed to be originated from the surface defects associated with oxygen vacancies [35]. The green emission peaks positioned around 520-530 nm (2.38-2.34 eV) are ascribed to the recombination of mobile electrons with trapped holes, which were assigned to oxygen-vacancy F and F^+ color centers [36, 37]. F center represents the neutral oxygen vacancy, whereas F^+ center represents oxygen vacancy losing one electron [38]. The PL that peaks at a red wavelength, 610 nm (~ 2 eV), is assigned to radiative recombination of electrons in deep traps [37, 39].

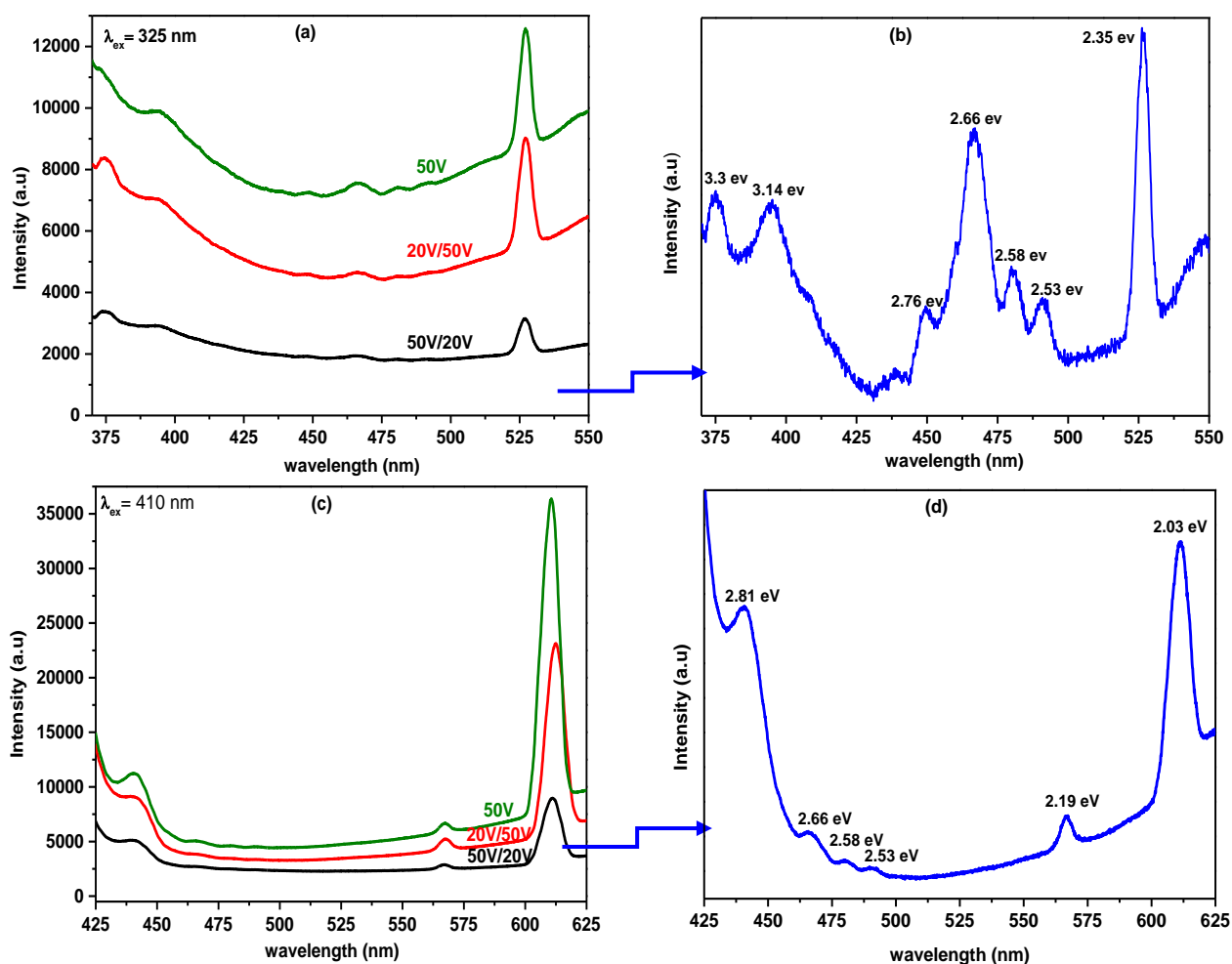
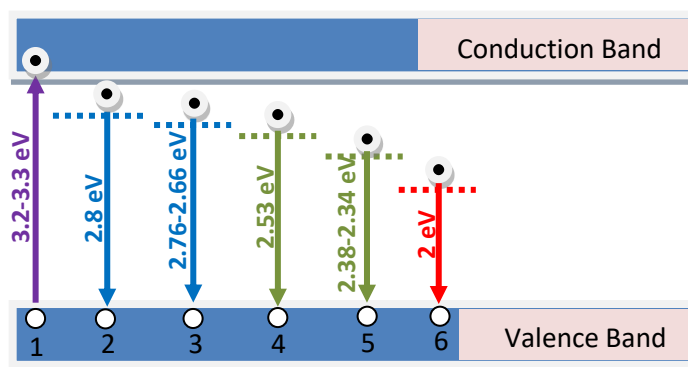


Figure III.6: Photoluminescence spectra of the different materials.

A schematic representation of the most probable emissions is summarized in the [scheme III.2](#) below.



1. Bandgap emission
2. STE localized on TiO_6 octaedra
3. Shallow and deep surface traps associated with the Ti^{3+} states
4. Surface defects associated with oxygen vacancies
5. Oxygen vacancies giving rise to F and F^+ centers
6. Emission caused by interstitial defects, Ti^{3+} .

Scheme III.2: The most probable emissions derived from photoluminescence analysis.

Among the three samples, the sample with more exposed $\{101\}$ facets (TiNT formed at 50V) displays the highest PL intensity. The PL of the sample is found to be orders of magnitude higher than others. PL intensity depends on the defects density as well as on the charge carrier transport, which compete with radiative recombination. Higher PL intensity of the sample with more exposed $\{101\}$ facets indicates the creation of more defect states in accordance with the above study. Furthermore, close examination of the red emission peaks provides evidence that electron traps are predominately located on (101) surface. So, high density of deep trapping sites on (101) surface increases charge carrier recombination rates and reduces the lifetime of photogenerated electrons and holes. Deep trap states that enhance recombination of carrier and impede carrier transport were already reported by Wang et al. [40]. In addition, very relevantly recent investigations by Tachikawa et al. [41], through a single-molecule imaging and kinetic analysis of the fluorescence also evidenced the preferential trapping of electrons on $\{101\}$ facets. Weaker PL intensities of the sample with more exposed $\{001\}$ facets (50V/20V TiNT) is most likely a consequence of its shallower gap states and/or lower amount of trapping sites and so lower photogenerated electron-hole recombination rate.

III.3.2 Optical bandgap analysis

UV-Vis diffuse reflectance spectroscopy was exploited to characterize the optical properties of the different systems. **Figure III.7 (a)** shows the UV-vis diffuse reflectance spectra of the different TiNT electrodes.

As can be seen, all the samples exhibit the same typical UV-Vis light absorption spectrum. The highest absorbance was recorded in the UV range, which is characteristic of TiO₂ materials. All the spectra show an absorption edge at ~ 400 nm, corresponding to the band gap energy of ~3.1 eV which may be attributed to the direct absorption of the intrinsic band gap of TiO₂. The light absorption is more improved in the visible range for 50V/20V TiNT, displaying higher {001} facets, which means that the former have the singular capacity to collect, guide and trap light, leading to the formation of more electron-hole pairs.

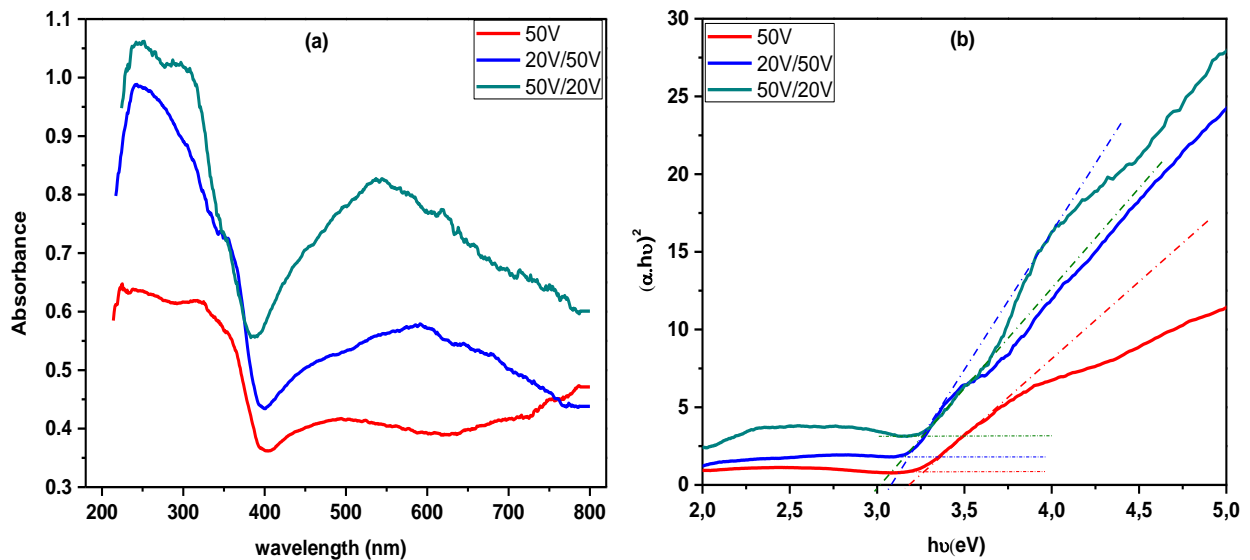


Figure III.7: (a) UV-Vis spectra of TiNT electrodes and (b) the corresponding Tauc plots.

From optical absorption measurements, optical band gap energy (E_g) of the different samples were determined by means of Tauc plot [42].

Tauc plots are presented in **figure III.7 (b)**. As can be seen, linear portions were established in a large gap of optical energies, indicating that the excitation process of the materials is governed by an indirect allowed transition. The intrinsic band gaps of the materials are determined by extrapolating the linear portions of the plots to the photon energy axis. Higher bandgap energy of about 3.2 eV is obtained in the case of TiNT formed at 50V. 20V/50V TiNT exhibits bandgap

energy of 3.1 eV. Whereas, 50V/20V TiNT display bandgap energy of about 3.01 eV, which is decreased by 0.19 eV from that of TiNT formed at 50V.

The noticed red-shift in the absorption threshold and so the bandgap narrowing concern TiNT with dominant {001} facets only and suggest that the band structure of the different materials are largely modified by the atomic distribution as well as by the gap states location.

Note that such a band gap narrowing was already reported and was connected to an increased amount of exposed {001} facets percentage [43-45].

III.4 Photoelectrochemical (PEC) measurements

PEC analysis is often used to investigate charge carrier transfer within the photocatalysts and can yield valuable information on the photocatalytic process. The effect of the preferential exposed facets of TiNT films on their photoelectrochemical water oxidation performance was evaluated under UV and visible lights by LSV measurements. LSV provides the photocurrent densities of the different samples.

Figure III.8 (a) shows photocurrent densities of the prepared samples under UV light. As can be seen, TiNT formed at 50V, with {101} facets exhibit lower photocurrent response. Photocurrent density of about 60 $\mu\text{A}/\text{cm}^2$ was obtained at water oxidation potential (0.23 V/Ag/AgCl), apparently due to its significantly higher deep trap state density. Whereas, 50V/20V TiNT, displaying higher exposed {001} facets, shows the best PEC water splitting performance, photocurrent reached 200 $\mu\text{A}/\text{cm}^2$ at 0.23 V/Ag/AgCl, which is more than 3 times that of TiNT with {101} exposed facets.

The photocurrents demonstrated by the 50/20 TiNT are better than those of TiNT dominated by {101} exposed facets. Photocurrent values in the range of 10-70 $\mu\text{A}/\text{cm}^2$ were previously reported on TiNT with preferred (101) orientation [48-50]. As an example, photocurrent value of about 10 $\mu\text{A}/\text{cm}^2$ was measured for TiNT produced under almost the same conditions, i.e. in ethylene glycol solution (0.5 wt% NH_4F and 10 wt% distilled water) [50], while 60 $\mu\text{A}/\text{cm}^2$ was measured for TiNT produced in ethylene glycol electrolyte containing 0.3wt% NH_4F , 2 vol% H_2O by two step anodization [48]. More recent work reports photocurrent of about 70 $\mu\text{A}/\text{cm}^2$ for TiNT synthesized in ethylene glycol electrolyte containing 0.1M NH_4F , 5 wt% H_2O and 1.5M lactic acid [49].

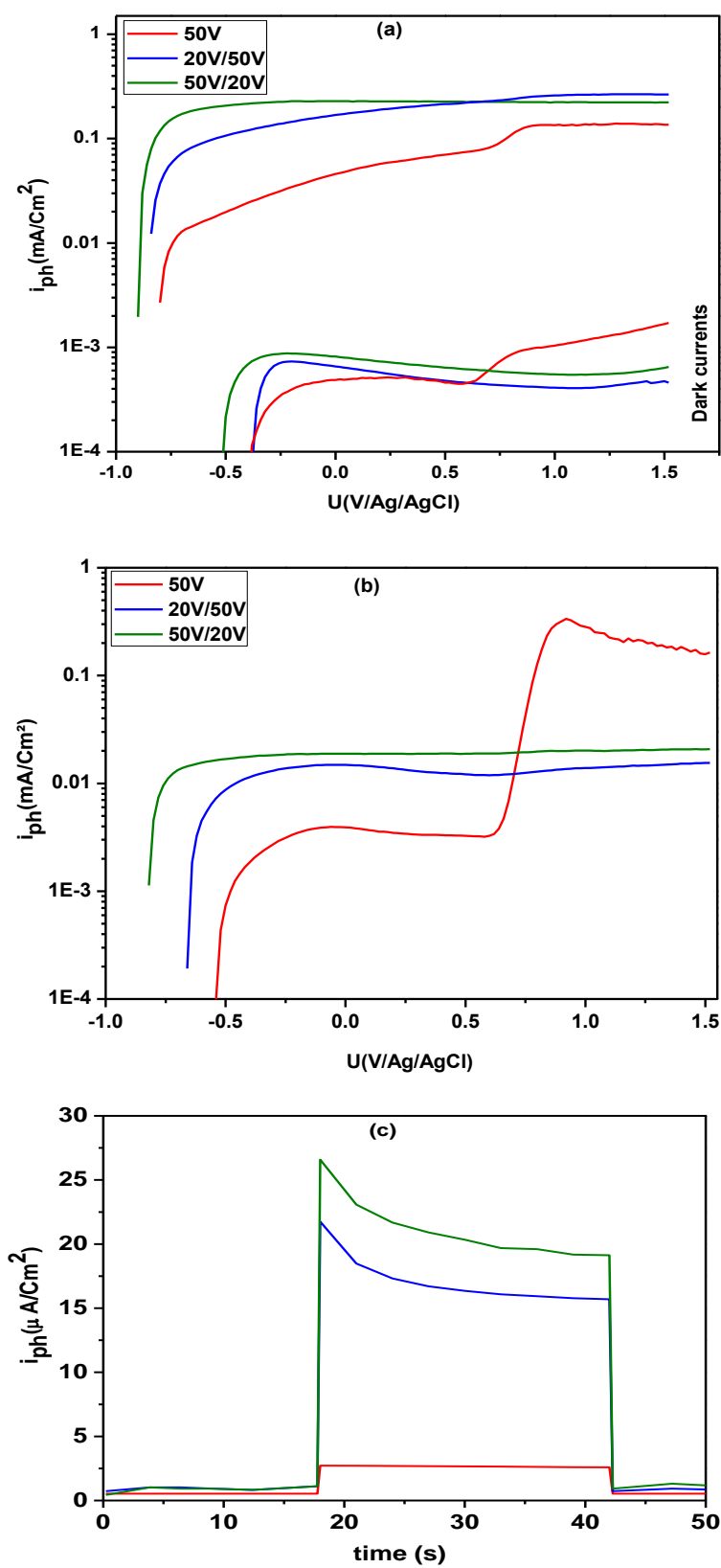


Figure III.8: (a) photocurrent densities of the electrodes under UV light, (b) photocurrent densities of the electrodes under visible light and (c) photocurrent transients under visible light, recorded at 0.2 V vs. Ag/AgCl.

Under visible light (Figure III.8 (b)), TiNT formed at 50V exhibit photocurrent densities of 3.4 $\mu\text{A}/\text{cm}^2$ at 0.23 V vs. Ag/AgCl. Whereas, the 50V/20V TiNT sample achieved the highest photocurrent density, it is about 0.02 mA/cm² at 0.23 V vs. Ag/AgCl. As the photocurrent is proportional to the number of photogenerated electrons transported to the external circuit, this suggests that 50V/20V TiNT performs more efficient charge transport. In other words, superior water splitting efficiency can be expected.

The transient photocurrent responses of the electrodes under visible light irradiation at a bias potential of 0.2 V are shown in figure III.8 (c). A rise in the photocurrent responses of TiNT dominated by {101} under illumination is due to the fast generation and separation of photo-generated electron-hole pairs at the TiNT/electrolyte interface. The value trends of photocurrent are 50V/20V>20V/50V>50V.

To further support the efficiency of the highly {001} exposed facets on the photogenerated charge carrier separation and transfer, flatband potential which refer to the position of the Fermi level of the semiconductor, were estimated by measuring the photocurrent onset through Gärtner-Butler analysis of the square of the photocurrent as a function of electrode potential [51]. Figure III.9 (a-c) shows squared photocurrent versus electrode potential of the considered systems. At low values of applied bias, the plots closely approximate straight lines. This behaviour was related to the separation of photogenerated charges by the electric field of the depletion layer [52]. Intersections with the potential axis of the extrapolated plots gives U_{FB} values of -0.5, -0.63 and -0.82V for TiNT formed at 50V, 20V/50V TiNT and 50V/20V TiNT respectively. U_{FB} of the highly {001} exposed facets (50V/20V TiNT) is the most negative, which means that the depleted space charge layer of the electrode provides the stronger electrical field that is indispensable for an effective separation of photoexcited electrons from holes. Furthermore, the shift of U_{FB} towards more negative values results in an up-shift of Fermi level to the conduction band and a larger band bending, which makes the electron-hole separation more efficient. Higher U_{FB} of TiNT, exhibiting abundant {101} facets indicates enhanced recombination of the photoelectrons and holes as noticed before.

From the point of view of the photoconversion efficiencies of the PEC systems, it is necessary to recall that PEC water oxidation reaction relies on three typical processes: (i) light absorption, leading to electron-hole pair formation, (ii) photogenerated carriers separation and transfer and (iii) interfacial chemical reaction. So better PEC performance of the sample with highly exposed {001} facets may be associated to its better optical absorption as well as to its better photogenerated carriers separation and transport as supported by absorbance spectra, photoluminescence and photocurrent onset.

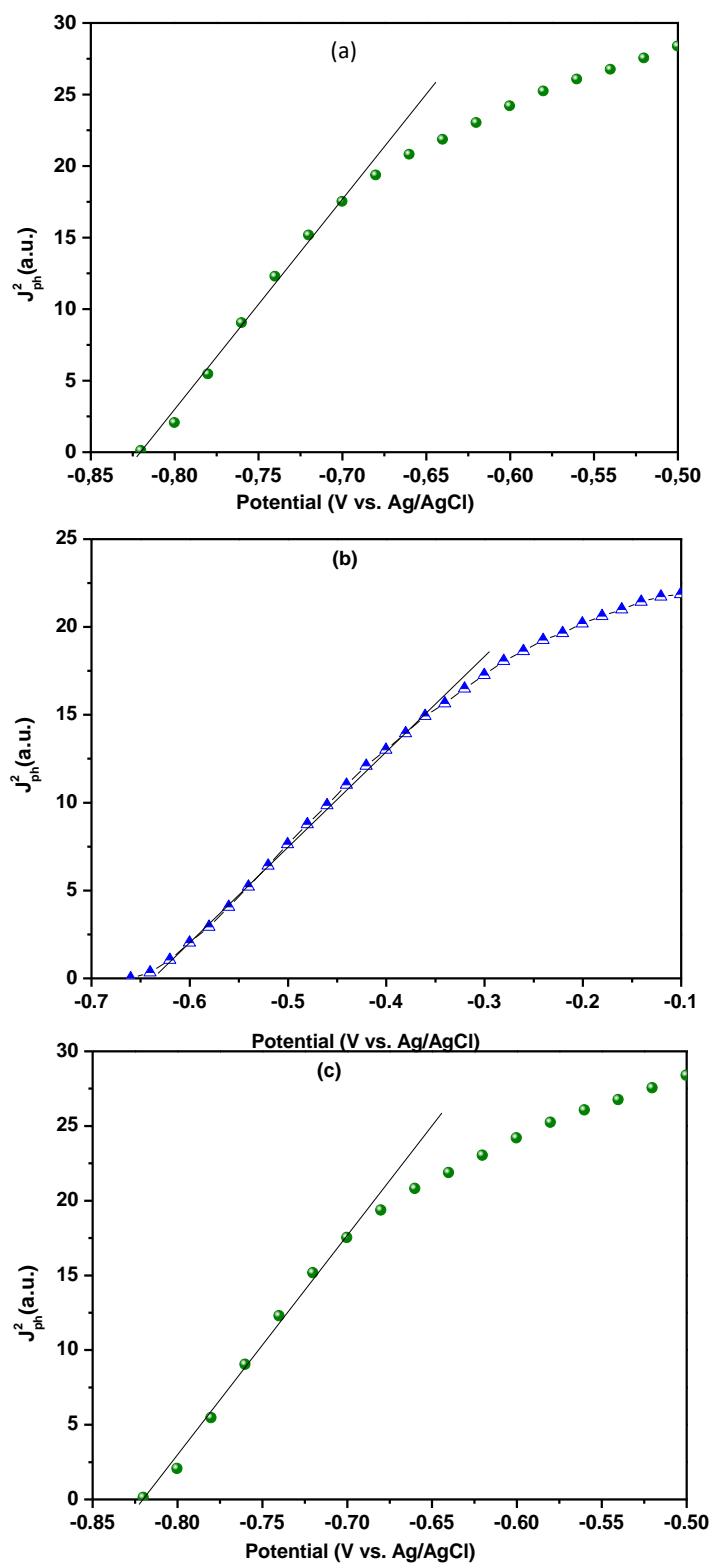


Figure III.9: Squared photocurrent versus electrode potential of TiNT formed at (a) 50V, (b) 20V/50V TiNT and (c) 50V/20V TiNT.

Different explanations were reported in the literature to account the improved separation rate of photogenerated electrons and holes of TiO₂ exhibiting different facets. The most common one is based on the heterojunction concept [53-55]. According to this concept, the different exposed facets result in different energy levels in the valence and conduction bands, which drive the electrons and holes to different crystal facets aiming to reach the most stable energy configuration. These energy levels dictate the transfer route of photoexcited holes and electrons, which can directly affect the carrier separation. So, the co-existence of various exposed facets in the same crystal is favourable in the separation and transfer of photogenerated charge carriers.

In the present work, we suggest that the improved charge carriers collection and separation in TiNT dominated by {001} facets is primarily attributed to the reduction in the density of deep trap states. The reduced deep trap state density and so the long electron diffusion path most probably facilitated charge collection and transfer across the electrode.

III.5 Photocatalytic performance

The influence of selected TiNT on the photocatalytic degradation of methylene blue was investigated under UV and visible irradiations. The UV-Vis spectra of MB decomposition at different time intervals exhibit an absorption wavelength maximum at 663 nm.

The photocatalytic reactivity of the materials is quantified by the ratio between the residual concentration (C) and the initial concentration (C_0) of MB, denoted as C/C_0 . **Figure III.10 (a-b)** shows the results of MB degradation for the different photocatalysts under UV and visible illuminations. As can be seen, oxidation occurs at a low rate during the first 25 minutes. This step which is associated with an adsorption process is followed by a noticeable change in the reaction rate, indicating a change in reaction kinetics. As expected, 50V/20V TiNT display superior photocatalytic activity for the degradation of MB under both UV and visible lights, signifying that this sample present a large amount of surface active sites, facilitating the adsorption of organic molecules and enhancing the MB photodegradation. In contrary, TiNT formed at 50V display a lower photocatalytic activity.

Figure 10 (c-d) illustrates the photocatalytic degradation efficiency of the considered materials under UV and visible irradiation. 50V/20V TiNT exhibited the highest MB photodegradation efficiencies of about 40% after 45 min of UV irradiation and about 15% after 60 min of visible irradiation, indicating that 50V/20V TiNT as a photocatalyst was better-quality.

Photocatalytic efficiency of TiNT increases in accordance with an increase in the exposure degree of the {001} facets. 50V/20V TiNT, with best crystallinity and predominant {001}

facets, shows the best photocatalytic performance. Photocatalytic efficiency may be related to the reactivity of {001} facets, which are more reactive than {101} facets, thus leading to a strong absorption of reactant molecules. Most long-lasting electrons in TiNT formed at 50V are trapped at deep levels and consequently located at low energy levels, which can be considered as insufficient to contribute in redox reactions.

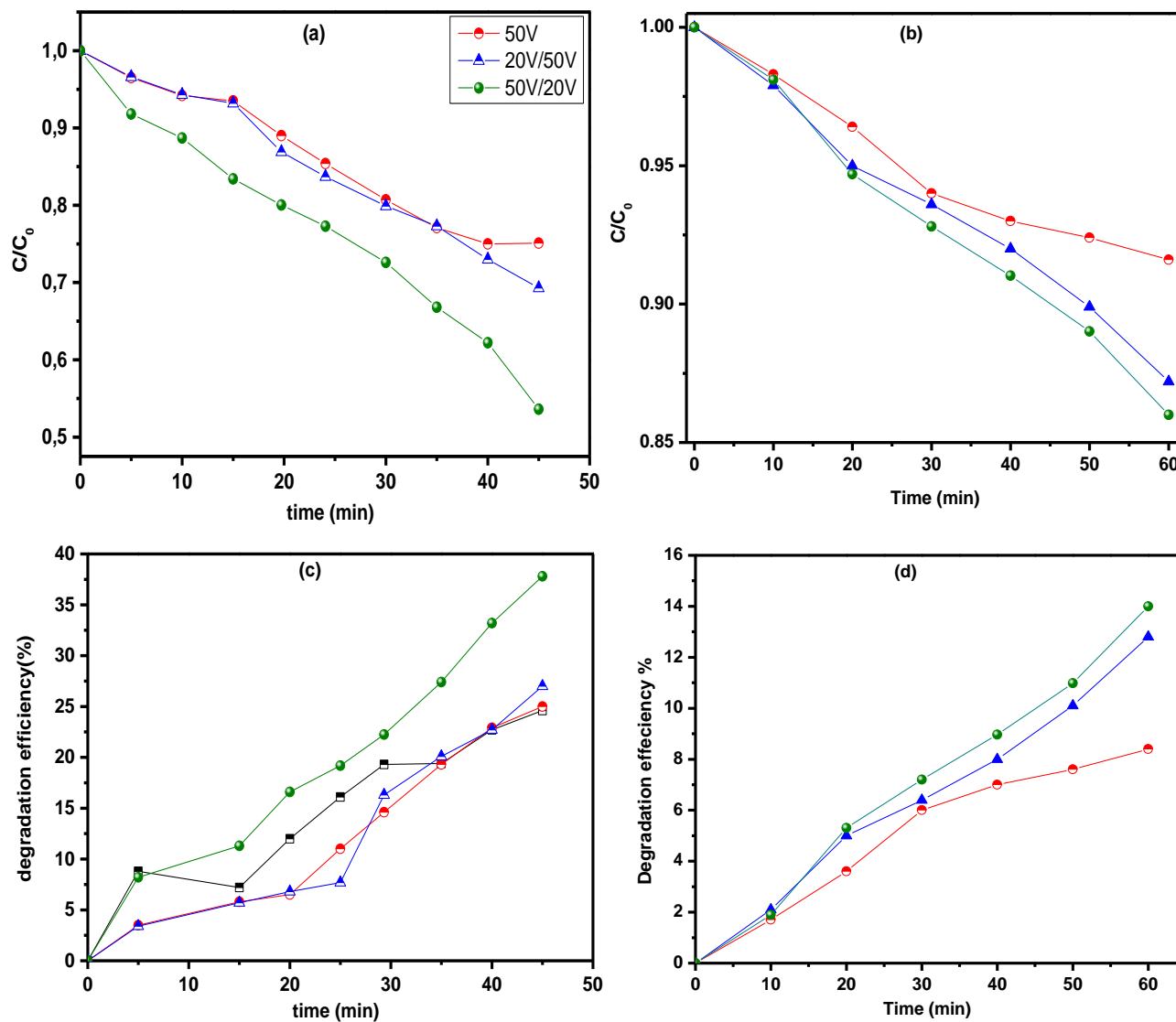


Figure III.10: (a) C/C_0 under UV light, (b) C/C_0 under visible light, (c) corresponding photocatalytic degradation efficiency under UV light and (d) corresponding photocatalytic degradation efficiency under visible light for the different photocatalysts.

Conclusion

In the present work, TiNT dominated with {101} facets and {001} facets were fabricated by one step and two step anodization approaches respectively in an electrolyte containing ethylene glycol, 2 wt% of water and 0.27M NH_4F .

The following conclusions have been drawn:

Different surface facets on TiNT exhibit obviously different defect gap states properties. An exponential defect states distribution was revealed by CV measurements.

Long lasting charge carriers were identified in the more exposed {101} surface, due to deeper trap states, whereas shallow defect states and/or lower deep states are predominately found on {001} surface. The density of these shallow gap states decreases with increasing ratio of (001) exposed facets.

Photoluminescence peaks provide evidence that electron traps are predominately located on {101} facets compared to {001} facets. These deep trap states enhance recombination of carrier and impede carrier transport and are detrimental for photoelectrochemical and photocatalytic performances. Whereas, TiNT with dominant {001} facets, should be very effective in improving the separation and transfer of photogenerated electron-hole pairs and thus enhancing the photoelectrochemical and photocatalytic performances.

Different surface facets on TiNT showed also different band gap energies. TiNT dominated with {001} facets displayed bandgap energy of about 3.01 eV, which is decreased by 0.19 eV from that of TiNT dominated with {101} facets.

Consequently, in addition to the hydrogen generation through water splitting and removal of pollutants, we believe that synthesized TiNT with dominant {001} facets can be used in many other applications.

References

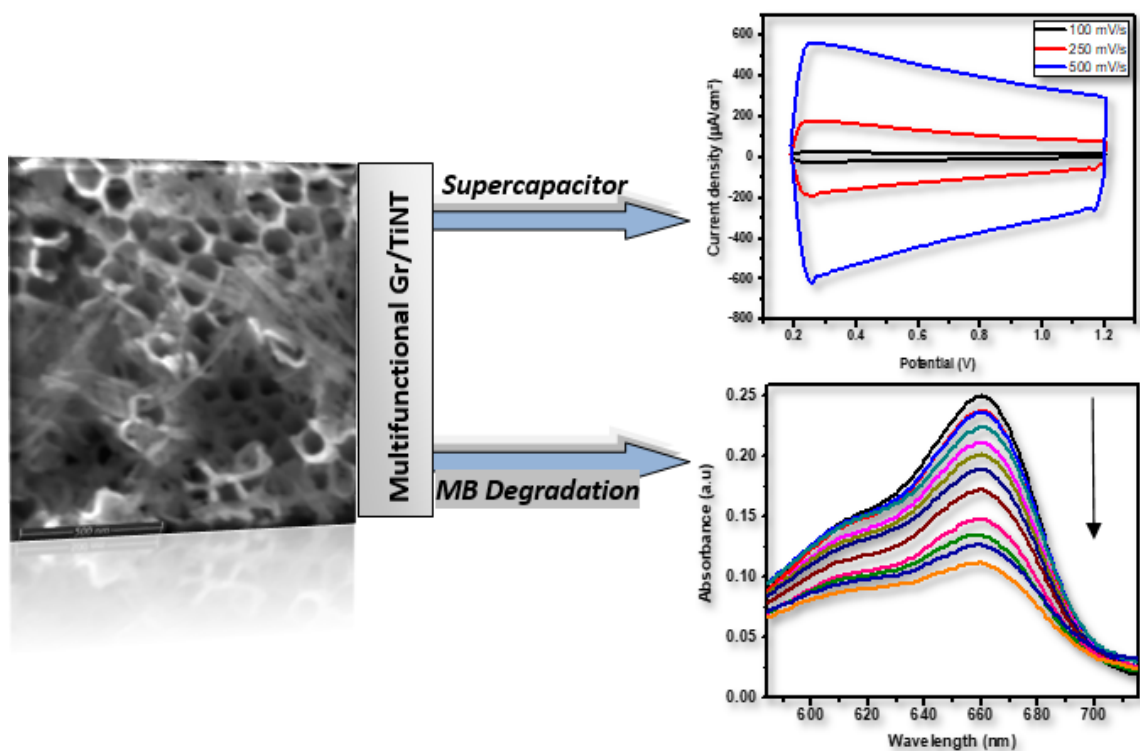
- [1] R. Gerbasi, M. Bolzan, N. El, G. Habra, L. Rossetto, A. Schiavi, S. Strini, Barison, *Journal of Electrochemical Society*, 156(2009)K233.
- [2] H. Lee, T. H. Park, D. J. Jang, *New Journal of Chemistry*, 40(2016)8737.
- [3] U. Diebold, *Surface Science Reports*, 48(2003)53.
- [4] L. Sun, Z. Zhao, Y. Zhou and L. Liu, *Nanoscale*, 4(2012)613.
- [5] H. Xu, S. Ouyang, P. Li, T. Kako and J. Ye, *ACS Applied Materials & Interfaces*, 5(2013)1348.
- [6] M-H. Jung, M-J. Chu, M. G. Kang, *Chemical Communications*, 48(2012)5016.
- [7] H.-B. Kim, H. Kim, W. I. Lee and D.-J. Jang, *Journal of Materials Chemistry A*, 3(2015)9714.
- [8] X. Han, Q. Kuang, M. Jin, Z. Xie, L. Zheng, *Journal of the American Chemical Society*, 131(2009)3152.
- [9] G. Shukri, H. Kasai, *Surface Science*, 619(2014)59.
- [10] S. Lee, J. Park, D. H. Kim, W. M. Seong, D. W. Kim, G. S. Han, J. Y. Kim, H. S. Jung, K. S. Hong, *Energy & Environmental Science*, 5(2012)7989.
- [11] J. Ding, Z. Huang, J. Zhu, S. Kou, X. Zhang, H. Yang, *Scientific Reports*, 5(2016)17773.
- [12] N. Roy, Y. Sohn and D. Pradhan, *ACS Nano*, 7(2013)2532.
- [13] X. G. Han, Q. Kuang, M. S. Jin, Z. X. Xie, L. S. Zheng, *Journal of the American Chemical Society*, 131(2009)3152.
- [14] S. Chen, D. Li, Y. Liu, W. Huang, *The Journal of Catalysis*, 341(2016)126.
- [15] Y. Cao, Q. Li, C. Li, J. Li and J. Yang, *Applied Catalysis B: Environmental*, 198(2016)378.
- [16] L. Liu, Y. Jiang, H. Zhao, J. Chen, J. Cheng, K. Yang and Y. Li, *ACS Catalysis*, 6(2016)1097.
- [17] O. Lyandres, D. Finkelstein-Shapiro, P. Chakthranont, M. Graham, K. A. Gray, *Chemistry of Materials*, 24(2012)3355.
- [18] S. Weon, E. Choi, H. Kim, J. Y. Kim, H. J. Park, S. m. Kim, W. Kim, W. Choi, *Environmental Science & Technology*, 52(2018)9330.
- [19] Y. Dai, C. M. Cobley, J. Zeng, Y. Sun, Y. Xia, *Nano Letters*, 9(2009)2455.
- [20] X. Y. Ma, Z. G. Chen, S. B. Hartono, H. B. Jiang, J. Zou, S. Z. Qiao, H. G. Yang, *Chemical Communications*, 46(2010)6608.
- [21] K. Ding, Z. Miao, Z. Liu, Z. Zhang, B. Han, G. An, S. Miao and Y. Xie, *Journal of American Chemistry Society*, 129(2007)6362.

- [22] G. Liu, C. Sun, H. G. Yang, S. C. Smith, L. Wang, G. Qing, H. M. Cheng, *Chemical Communications*, 46(2010)755.
- [23] A. Auer, E. Portenkirchner, T. Götsch, C. V. Vidal, S. Penner, J. Kunze-Liebhäuser, *ACS Applied Materials Interfaces*, 9(2017)36828.
- [24] Y. Pang, G. Xu, Q. Feng, J. Lv, Y. Qin, Y. Zhang, Z. Zheng, Y. Wu, *Physics Letters A*, 382(2018)2759.
- [25] L. Hamadou, A. Kadri, N. Ben Brahim, J-P. Petit, *Journal of Electrochemical Society*, 154(2007)G291.
- [26] D. B. Bonham, M. E. Orazem, *Journal of Electrochemical Society*, 139(1992)127.
- [27] F. Fabregat-Santiago, I. Mora-Seró, G. Garcia-Belmonte, J. Bisquert, *Journal of Physical Chemistry*, 107(2003)758.
- [28] S. Moser, L. Moreschini, J. Jacimovic, O. S. Barisic, H. Berger, A. Magrez, Y. J. Chang, K. S. Kim, A. Bostwick, E. Rotenberg, L. Forro, M. Grioni, *Physical Reviews Letters*, 110(2013)196403.
- [29] A. G. Thomas, W. R. Flavell, A. K. Mallick, A. R. Kumarasinghe, D. Tsoutsou, N. Khan, C. Chatwin, S. Rayner, G. C. Smith, R. L. Stockbauer, S. Warren, T. K. Johal, S. Patel, D. Holland, A. Taleb, and F. Wiame, *Physical Review B*, 75(2007)035105.
- [30] K. Rajkumar, P. Vairaselvi, P. Saravanan, V. T. P. Vinod, Miroslav Cernik, R. T. Rajendra Kumar, *RSC Advances*. 5(2015)20424.
- [31] S. Mathew, A. K. Prasad, T. Benoy, P. P. Rakesh, M. Hari, T. M. Libish, P. Radhakrishnan, V. P. N. Nampoori, C. P. G. Vallabhan, *Journal of Fluorescence*, 22(2012)1593.
- [32] T. Tachikawa, T. Majima, *Langmuir*, 25(2009)7791.
- [33] H. Zhang, M. Zhou, Q. Fu, B. Lei, W. Lin, H. Guo, M. Wu and Y. Lei, *Nanotechnology*, 25(2014)275603.
- [34] A. Sarkar, K. Karmaka, G. G. Khan, *Journal of Physical Chemistry*, 121(2017)25705.
- [35] W. Y. Wu, Y. M. Chang, J. M. Ting, *Crystal Growth & Design*, 10(2010)1646.
- [36] C. C. Mercado, F. J. Knorr, J. L. McHale, S. M. Usmani, A. S. Ichimura, and V. L. Saraf, *Journal of Physical Chemistry C*, 116(2012)10796.
- [37] D. K. Pallotti, L. Passoni, P. Maddalena, F. D. Fonzo, S. Lettieri, *Photoluminescence Mechanisms in Anatase and Rutile TiO₂*, *Journal of Physical Chemistry C*, 121(2017)9011.
- [38] Y. Lei, L. D. Zhang, G. W. Meng, G. H. Li, X. Y. Zhang, C. H. Liang, W. Chen, and S. X. Wang, *Applied Physics Letters*, 78(2001)1125.
- [39] K. Y. Jung, S. B. Park, M. Anpo, *The Journal of Photochemistry and Photobiology A*, 170(2005)247.

- [40] Q. Wang, Z. Zhang, S.M. Zakeeruddin, M. Gratzel, *Journal of Physical Chemistry C*, 112(2008)7084.
- [41] T. Tachikawa, S. Yamashita, T. Majima, *Journal of the American Chemical Society*, 133(2011)7197.
- [42] M. Singh, D. Jampaiah, A. E. Kandjani, Y. M. Sabri, *Nanoscale*, 10(2018)6039.
- [43] H.-B. Kim, H. Kim, W. I. Lee, D.-J. Jang, *Journal of Materials Chemistry A*, 3(2015)9714.
- [44] K. Cheng, W. Sun, H.-Y. Jiang, J. Liu, J. Lin, *Journal of Physical Chemistry C*, 117(2013)14600.
- [45] L. Ye, J. Mao, J. Liu, Z. Jiang, T. Peng, L. Zan, *Journal of Materials Chemistry A*, 1(2013)10532.
- [46] Y. Lai, H. Zhuang, K. Xie, D. Gong, Y. Tang, L. Sun, C. Lin, Z. Chen, *New Journal of Chemistry*, 34(2010)1335.
- [47] R.P. Vitiello, J.M. Macak, A. Ghicov, H. Tsuchiya, L.F.P. Dick, P. Schmuki, *Electrochemistry Communications*, 8(2006)544.
- [48] J. Zhou, L. Yin, H. Li, Z. Liu, J. Wang, K. Duan, S. Qu, J. Weng, B. Feng, *Materials Science in Semiconductor Processing* 40(2015)107.
- [49] S. Mohajernia, S. Hejazi, A. Mazare, N. T. Nguyen, P. Schmuki, *Chemistry: A European Journal*. 23(2017)12406.
- [50] Z. Xu, J. Yu, *Nanoscale*, 3(2011)3138.
- [51] A. Hankin, F. E. Bedoya-Lora, J. C. Alexander, A. Regoutz, G. H. Kelsall, *Journal of Materials Chemistry*, 7(2019)26162.
- [52] Yu. V. Pleskov, M. D. Krotova, *Electrochimica Acta*, 38(1993)107.
- [53] L. Ye, J. Liu, L. Tian, T. Peng, L. Zan, *Applied Catalysis B: Environmental* 134(2013)60.
- [54] R. G. Li, H. X. Han, F. X. Zhang, D. E. Wang and C. Li, *Energy & Environmental Science*, 7(2014)1369.
- [55] T. Tachikawa and T. Majima, *Chemical Communications*, 48(2012)3300.

Chapter IV

Promising supercapacitive and photocatalytic performances of TiO₂ nanotubes loaded with graphene.



Graphical abstract

Introduction

The energy crisis and environmental pollution are the two major interconnected problems of the modern society. To overcome these issues, various approaches have been developed. Among them, the design of multifunctional nanomaterials is attracting a lot of attention due to their ability to combine simultaneously many applications. Various metal oxide-based semiconductor nanostructures have been attempted. Owing to its non-toxicity and photostable characteristics, TiO₂ has gained a lot of attention and has been considered as a promising candidate for both energy and environmental issues [1, 2].

To overcome the TiO₂ limitations, its doping with carbon based materials have attracted abundant attention. Among carbon materials, graphene has attracted a considerable interest and hybridization of TiO₂ with graphene is a prominent alternative to deal with the shortcomings. Kamat and co-workers [3], believed graphene would provide channels for transferring electrons and thus reducing recombination between electrons and holes in the graphene/TiO₂ composite photocatalysts.

Graphene is a two-dimensional sp² hybrid carbon structure. It has an hexagonal honeycomb-like structure with carbon-carbon interlayer distance of 1.42 Å. Graphene has become one of the most exciting research topics in the last decade. Its unique properties including high specific surface area, high chemical stability and elasticity along with excellent electrical conductivity make it a suitable material for numerous applications.

In order to produce graphene from graphite for these applications, numerous fabrication procedures have been attempted. One may cite: chemical vapor deposition (CVD) process [4], thermal decomposition on SiC wafer under ultrahigh vacuum (UHV) [5], electrochemical exfoliation approach [6] and Hummers methods [7].

The electrochemical exfoliation of graphite in anodic or cathodic conditions has emerged as a possible candidate for the mass-production of graphene. It has many advantages over other methods, including large-scale, fast production-rate, low-cost, simple operation and high-quality graphene, i.e. negligible amount of defects and residual oxygen-containing functional groups. Electrochemical exfoliation forces the intercalation of electrolyte ions between the graphene layers with their exfoliation as the consequence [8, 9]. Exceptional exfoliation efficiency has been reported in sulfate-containing electrolytes compared to other aqueous electrolyte systems [10]. Sulfate anions can move relatively freely within the graphite lattice, compared to other anions, facilitating the diffusion of more water molecules into the bulk of the graphite. The subsequent water oxidation enables efficient exfoliation of graphite into

graphene [11]. The detailed mechanism of the electrochemical exfoliation of graphite into graphene in aqueous electrolyte containing sulfate anions (SO_4^{2-}) can be found in [10].

Coupling TiO_2 with graphene has been shown to be more photocatalytically active than pure TiO_2 . It is commonly accepted that graphene sheets act as an electron acceptor enabling the transfer and separation of photogenerated electrons, therefore reducing the electron-hole recombination [12]. Besides applications involving a light source, TiNT are also attractive candidates for electrochemical energy storage devices. Among these devices, the supercapacitor is nowadays considered to have high potential in future electronics [13]. Supercapacitors also known as electrochemical capacitors or ultracapacitors are considered to be one of the most promising power sources for many systems.

TiNT are very prospective as electrodes for supercapacitors due to their excellent electrochemical stability and their large specific surface area which promote the availability of solvated ions. However, the specific capacitances of TiNT previously cited in the literature are in the order of ($80\text{-}911 \mu\text{F cm}^{-2}$) [15-16]. The relatively low specific capacitance has most often been attributed to their low electrical conductivity and their weak electrochemical activity because of their wide band gap semiconductor characteristic. As graphene has been extensively explored as an EDLC material, a promising way to improve the capacitance performance of TiNT is their combination with graphene.

In this chapter, we report a simple cost-effective approach to synthesis Gr/TiNT composite by combining anodization and electrochemical reduction processes. Graphene with high electrical conductivity, low amount of oxygen-containing functional groups and free metallic and non-metallic impurities was produced by electrochemical exfoliation of pure graphite sheet in sulfate-containing electrolytes. Less consideration has been afforded to the effects of the inevitable residual oxygen functional groups of Gr on the capacitive and photocatalytic mechanisms. So, for comparison, graphene exfoliated from 5B (82% graphite and 12% clay) pencil cores was also synthesized to explore the effect of oxygen functional groups on the specific capacitance and photocatalytic performances. Very few studies have explored the application of TiNT as a supercapacitor. So, to the best of our knowledge, this kind of study has never been reported on TiNT modified by graphene.

IV.1 Graphite exfoliation

Electrochemical exfoliation was conducted in sulfate-containing electrolyte (H_2SO_4). Pure graphite sheet (99.8%) and pencil (5B) core were used as sources to form graphene (Figure IV.1 ((a) and (b))). In a typical synthesis approach, a two-electrode cell was used. The

graphene source (graphite foil or pencil (5B) core) was connected to the anode of a power supply and a platinum foil to the cathode. The two electrodes were placed parallel with a separation of a few cm away. The electrochemical exfoliation was conducted by applying a relatively high voltage (10V) for some minutes). The foil electrode itself vanished gradually. It is important to mention that H_2SO_4 electrolyte exhibited ideal exfoliation efficiency from pure graphite and 5B pencil core. Particularly, graphite sheet exfoliation showed a notably higher production rate. The graphite source electrode vanished rapidly.

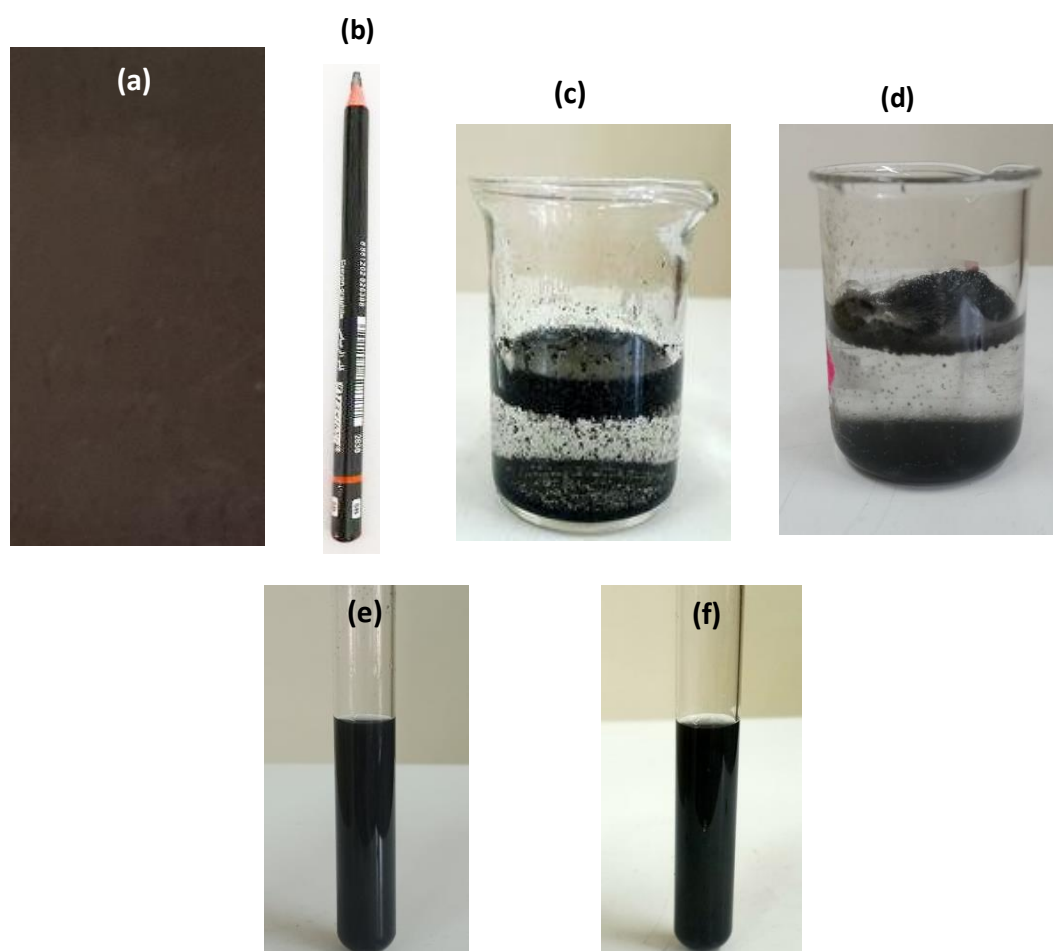


Figure IV. 1: Synthesis of graphene. (a) Photograph of pure graphite sheet (99.8%), (b) Photograph of black-marking pencil (5B), (c) Photograph show the condition after electrochemical exfoliation of pure graphite sheet in H_2SO_4 electrolyte, (d) Photograph show the condition after electrochemical exfoliation of 5B pencil core in H_2SO_4 electrolyte, (e) Photograph of dispersed graphene produced from pure graphite sheet in H_2SO_4 electrolyte, (f) Photograph of dispersed graphene produced from 5B pencil core in H_2SO_4 electrolyte.

Two main resulted products were distinguished after pure graphite and 5B pencil core exfoliations (Figure IV.1 ((c) and (d))): (i) black products, floated on the electrolyte surface and (ii) black precipitate, stayed at the bottom of the cell. In the case of 5B pencil core, this precipitate may be mainly composed by un-exfoliated graphite along with clay. This makes easy the separation of graphene from un-exfoliated graphite.

Black floated products were collected, washed several times with DI water via a vacuum filtration method, and then dried at 80° C for 24 h. To yield dispersed graphene, the obtained products were dispersed in 15 ml N, N-dimethylformamide (DMF) and placed in an ultrasonic bath for 30 minutes. Photographs of the resulted dispersed graphene are depicted in figure IV. 1 (e-f). As can be seen, characteristic of graphene black color is noticed whatever the graphite source.

IV.2 Graphene/TiNT hybrid system synthesis

Before electrodeposition, cyclic voltammetry (CV) measurements were used to find the appropriate potential for graphene deposition. Figure IV.2(a) shows CV curve of TiNT substrate in an aqueous solution containing 4 ml of dispersed Gr (from pure graphite sheet and 5B pencil core) and 35 ml of Na₂SO₄ (1M) as the supporting electrolyte at a scan rate of 20 mV/s. From the voltammograms, starting from the open potential and sweeping towards the cathodic direction, the reduction current started to be noticeable at -0.6 V for both solutions.

The selected potential for the electrodeposition was -0.8 V for both produced Gr. The application of negative potentials has in principle the advantage of reducing the oxygen functional groups introduced during the electrochemical exfoliation of graphite. The application of cathodic potentials below -0.7 V not only leads to the reduction of various oxygen functional groups, such as epoxide, peroxide, and aldehyde, but also to the reduction of water molecules [17].

The deposition time of 300 s was applied, longer deposition times (> 300 s) leads to a thick deposit of reduced graphene oxide onto the TiNT electrode, which is not very interesting and useful in terms of electrochemical performance. TiNT surfaces loaded with Gr would need to be modified so as to produce a few Gr monolayers or a few layers thick.

The resulted Gr/TiNT electrodes are labeled as PGr/TiNT (graphene was produced from pure graphite) and 5BGr/TiNT (graphene was produced from 5B pencil core).

Figure IV.2(b) shows the current vs. time profile for the potentiostatic electrochemical reduction of graphene onto TiNT by applying -0.8 V/Ag/AgCl. As can be seen, chronoamperometric curves of graphene electrodeposition were approximately the same. The current increases as the deposition time increases, reaching a plateau at the end of the deposition process. This shows that under these conditions the TiNT surface is coated by graphene.

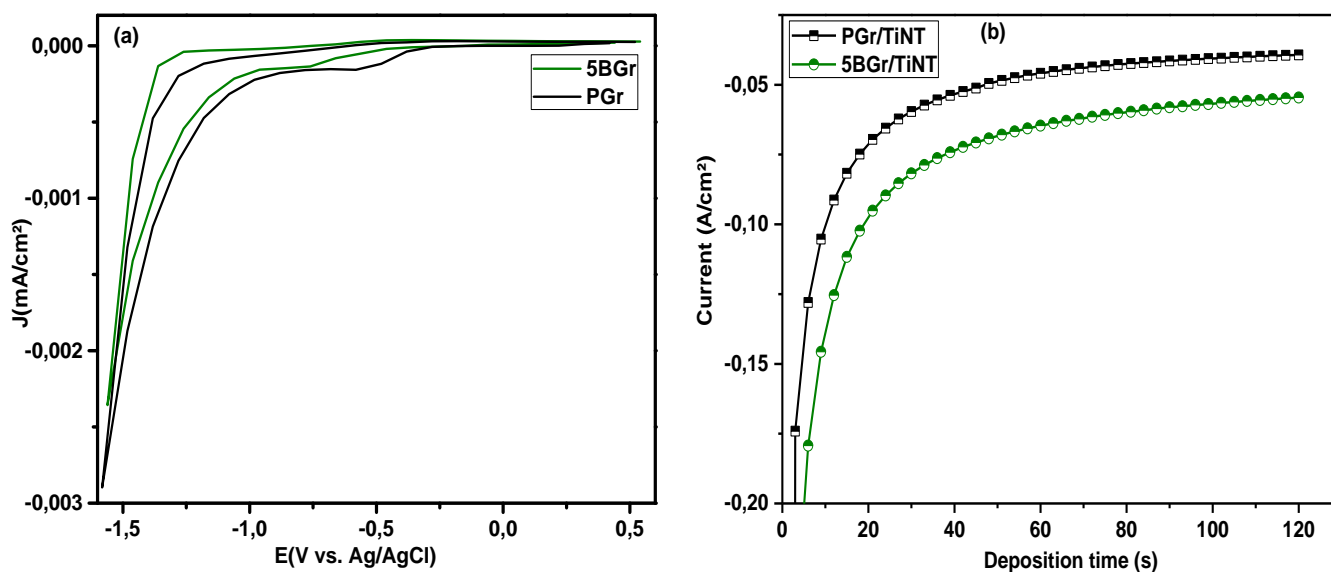


Figure IV. 2: (a) Cyclic voltammograms of TiNT in solution containing 4 ml of dispersed Gr (from pure graphite sheet and 5B pencil core) and 35 ml of Na₂SO₄ (1M) and (b) Current transients recorded during electrodepositing.

IV.3 Morphological and structural characterizations of Gr/TiNT

Figure IV.3 (a-d) shows the SEM images of Gr/TiNT. As can be seen, some transparent sheet products of graphene on the top of TiNT are clearly visible, which means that Gr/TiNT composites were well obtained and that graphene sheets were attached to the TiNT after electrodeposition. Exfoliated graphene sheets from pure graphite (Figure IV.3 (a)) reveal transparent, folded and wrinkled areas. The typical surface rippling of graphene is clearly visible. Graphene sheets from 5B pencil core (Figure IV.3 (b)) display relatively smooth flat surfaces which partly covered the TiNT surfaces. Surface elemental compositions of Gr/TiNT (Figure IV.3 (c, d)) were carried out by using EDS analysis. The presence of TiO₂ nanotubular layers is revealed by the characteristic peaks of Ti at 4.5 keV and 4.9 keV as well as at 0.5 keV for O. The peak associated with C at 0.4 eV is clearly observed in the spectra of both

Gr/TiNT samples, evidently resulted from graphene sheets. Short signals from N indicate the presence of low concentration of nitrogen in 5BGr/TiNT, which is most probably originated from the N,N-dimethylformamide used during the processing, whereas PGr/TiNT exhibits an impurity-free material. The atomic percentage of O in 5BGr/TiNT is 47%. Whereas, it is about 44% in PGr/TiNT, implying that some oxygen containing groups were removed.

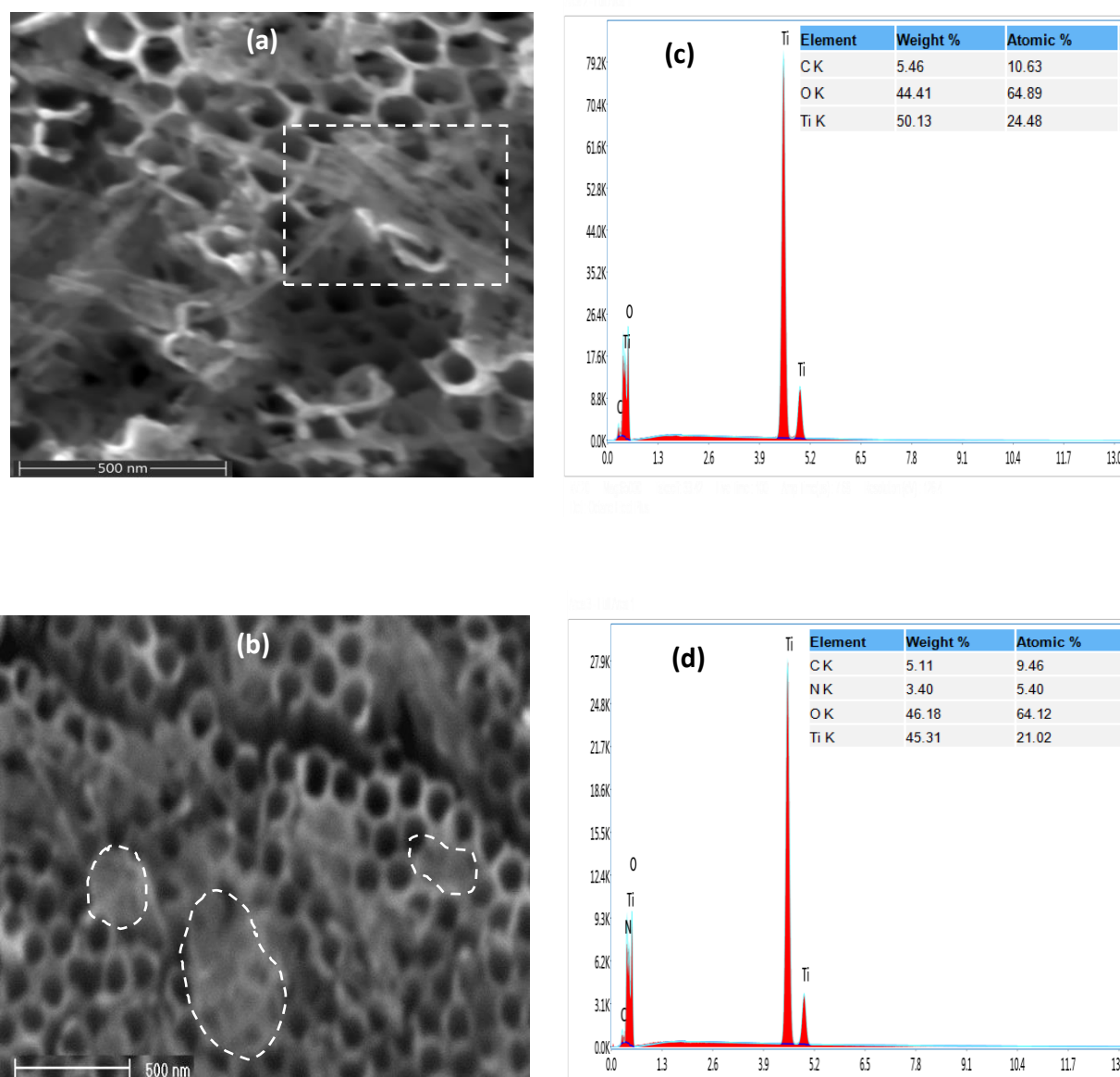


Figure IV. 3: SEM images of Gr/TiNT and corresponding EDS spectra.

The XRD analysis was used to characterize the crystalline nature and phase purity of the synthesized materials. The XRD patterns of both Gr/TiNT (**Figure IV. 4 (a)**) are similar to that of pure TiNT. All the diffraction peaks are ascribed to tetragonal TiO₂ anatase phase and to Ti

metal phase. No obvious characteristic diffraction peak for graphene was observed which is possibly due to the dispersed and thin graphene sheets, which is below the detection limit of XRD, or to an overlap of the main characteristic peaks of graphene and the (101) peak of anatase at around 25° , in accordance with earlier reports [18-20]. Remarkable shifts are observed in the peaks at around 25° (Figure IV.4 (b)) after graphene loading, which suggests the successful doping of graphene on TiNT and so the change in the lattice parameters of TiO_2 .

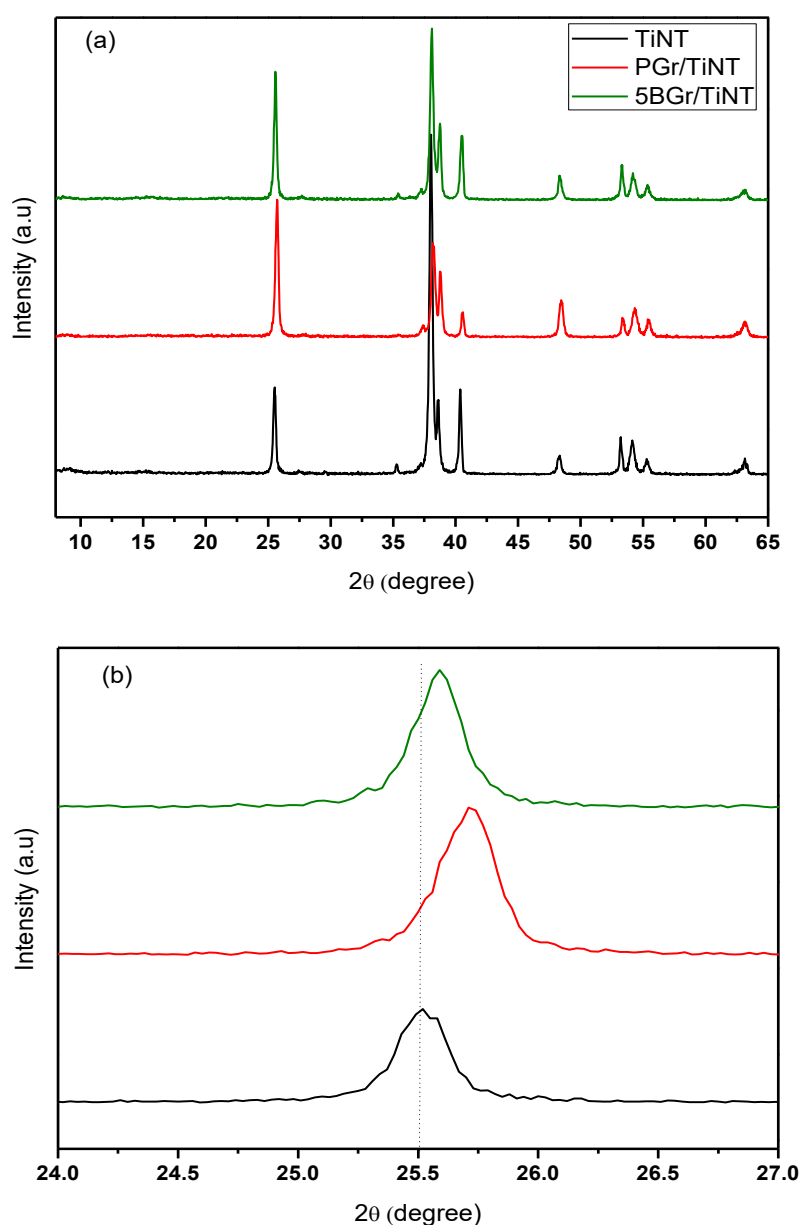


Figure IV.4: (a) XRD patterns of TiNT and Gr/TiNT samples and (b) Enlarged XRD pattern around 25° .

IV.4 Optical characterizations of Gr/TiNT systems

The prepared systems were further characterized by FTIR transmission spectra. FTIR was utilized to study the chemical groups of TiNT and their transformation when adding graphene. The FTIR spectra of TiNT and Gr/TiNT composites are presented in figure IV.5. The spectra of these samples show several common peaks that are mostly concentrated in the range from 800 to 1800 cm^{-1} .

The peak around 840 cm^{-1} can be assigned to the stretching vibration of Ti–O–Ti [21]. The observed peak at 1030 cm^{-1} corresponds to C–O–C stretching vibration [22]. The peak occurred at 1270 cm^{-1} can be attributed to the vibrations of C–O functional group [23]. The peak related to carboxyl (C–OH) bending vibration can be observed at around 1380 cm^{-1} [24]. Whereas, the peak associated to bending vibration of coordinated H_2O as well as Ti–OH can be observed around 1630 cm^{-1} [25, 26].

The peak near 1720 cm^{-1} indicates the stretching vibration of oxygen containing functional groups of carboxyl (C=O) [27].

Other bands at 2849 and 2963 are assigned to the stretching vibration of C–H bond [22, 28].

The broadest band in TiNT spectra is observed at around 3400 cm^{-1} , which is ascribed to the stretching vibrations of the surface hydroxyl group (O–H) [29, 30].

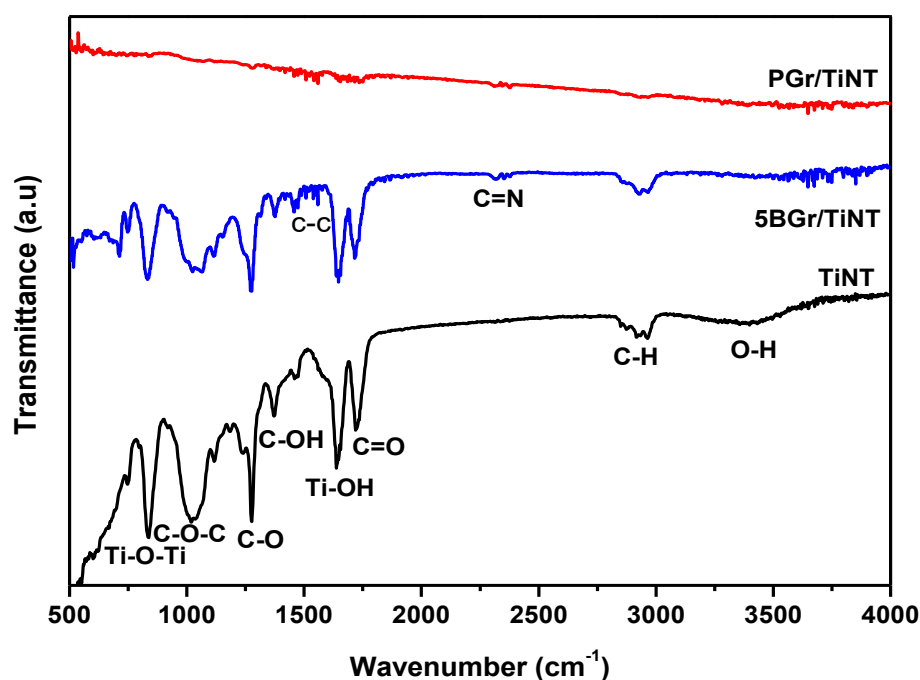


Figure IV.5: Fourier transform infrared spectroscopy (FTIR) spectra of TiNT and Gr/TiNT.

Note that for 5BGr/TiNT, the peak intensities decreased a little comparatively to TiNT. For PGr/TiNT, the peaks strengths are lower than the others and some of the peaks assigned to oxygen containing functional groups significantly decreased and even disappeared. For example, the bands associated to the stretching vibrations of surface hydroxyl group (O-H) and intercalated water between graphene sheets ($3000-3600\text{ cm}^{-1}$) vanished. Moreover, the bands associated to C-O functional group highly decreased, suggesting that graphene oxide on TiNT was reduced well.

In addition to the peaks observed on TiNT, FTIR spectrum of Gr/TiNT samples show a weak band at 1564 cm^{-1} corresponding to the sp^3 C-C stretching [31].

To investigate the graphene impact on light harvesting of TiNT, the UV-Vis absorption spectra were plotted and presented in [figure IV.6](#).

All samples exhibited absorption bands within the UV region (200-370 nm) of the spectra, which can be assigned to the intrinsic absorption of TiNT ($\text{O}2\text{p} \rightarrow \text{Ti}3\text{d}$).

The spectrum of TiNT shows an absorption edge at $\sim 400\text{ nm}$, which is attributing to the indirect absorption of the intrinsic band gap of TiO_2 . After graphene was loaded, the light absorption is improved above 600 nm range which is likely due to the formation of more electron-hole pairs. PGr/TiNT shows the highest UV and visible light absorption, which means it can be more activated with UV and solar lights.

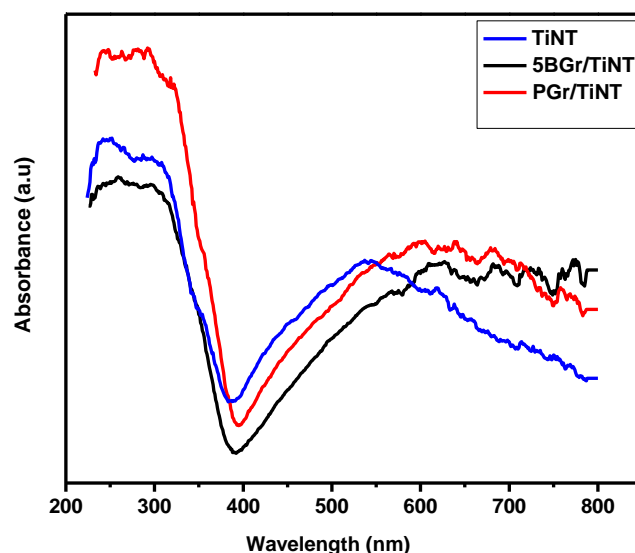


Figure IV. 6: (a) UV-visible absorption spectra of the different materials.

Photoluminescence was generally used to evaluate the efficiency of charge carrier trapping, migration and charge transfer. In this study, PL spectra of the samples were used as reliable approach for quantifying the defects density and in order to study the effect of graphene on the recombination of the photogenerated charges. **Figure IV.7** shows PL spectra of the different materials monitored with excitation of 325 nm. The same line shapes are noticed for all the materials. Although the PL intensities are different, the positions of the peaks are the same. The origin of the different emission peaks was already discussed in the previous chapter.

The introduction of graphene in TiNT results in a decrease of the PL intensity, demonstrating a significant reduction of the defects density and charge carrier recombination rate and so an enhanced charge separation of electron hole pairs when compared to TiNT. A lower PL emission intensity was depicted for PGr/TiNT, which may be attributed to its lower defects density and so lower photogenerated electron–hole recombination.

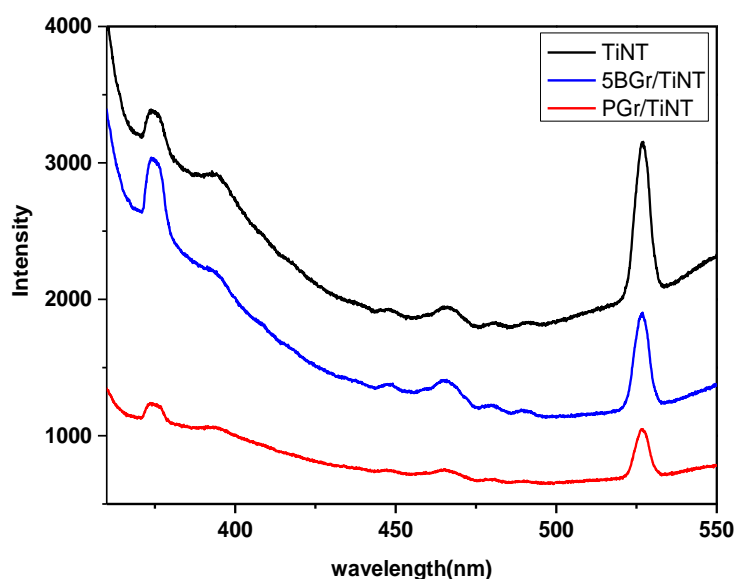


Figure IV.7: Photoluminescence spectra of the different materials.

IV.5 Electrochemical performance of the electrodes for supercapacitor

To evaluate the power capability of Gr/TiNT electrodes, electrochemical measurements, including galvanostatic charge–discharge (GCD), Electrochemical impedance spectroscopy (EIS) and cyclic voltammetry (CV) techniques were performed.

IV.5.1 GCD investigation

Among all electrochemical techniques, GCD tests are known to reflect real performance more accurately. GCD behaviors of the supercapacitors were examined by chronopotentiometry over the potential of 1V at different current densities. **Figure IV.8 (a)** shows the typical charge–discharge curves of TiNT and Gr/TiNT electrodes at 30 $\mu\text{A}/\text{cm}^2$. Pure TiNT showed quasi-linear and sloping charge-discharge profiles. A decrease in the slope of the charge curve is generally related to charge transfer through the electrode/electrolyte interface. This suggests non-ideal supercapacitor or pseudocapacitive characteristics of TiNT material, where electrode reactions are involved in the storage of pseudocapacitive charges.

The pseudocapacitive behavior of TiNT has already been attributed to the increased surface area of the nanostructured material [32]. According to Okubo et al. [33], some faradaic electrode materials that typically show strong redox reactions in bulk exhibit behaviors like pseudocapacitive materials with the size reduced to nanoscale. The surface or near-surface charge transfer leads to surface faradaic reaction of pseudocapacitor that is similar to EDLC [34, 35]. As a consequence, pseudocapacitive electrodes basically exhibit almost linear GCD curves.

The charge-discharge plots of Gr/TiNT electrodes exhibit isosceles triangles, indicating their good electrochemical capacitive characteristics. Among Gr/TiNT samples, PGr/TiNT exhibits an extended charge-discharge time and perfect symmetry. The mirror-like potential–time responses during the charge–discharge process is an indication of the good capacitive behavior achieved by Gr/TiNT electrodes.

To compare the charge storage actions of the Gr/TiNT electrodes, GCD curves with varying current densities have been analyzed and are depicted in **figure IV.8 (b, c)**. As can be seen, the charge-discharge time for each current density increases in the order of 5BGr/TiNT < PGr/TiNT, which reflects the highest specific capacitance of PGr/TiNT.

As the discharge curves of a Gr/TiNT electrodes are linear, their areal specific capacitances can be calculated using the slopes of the discharge curves

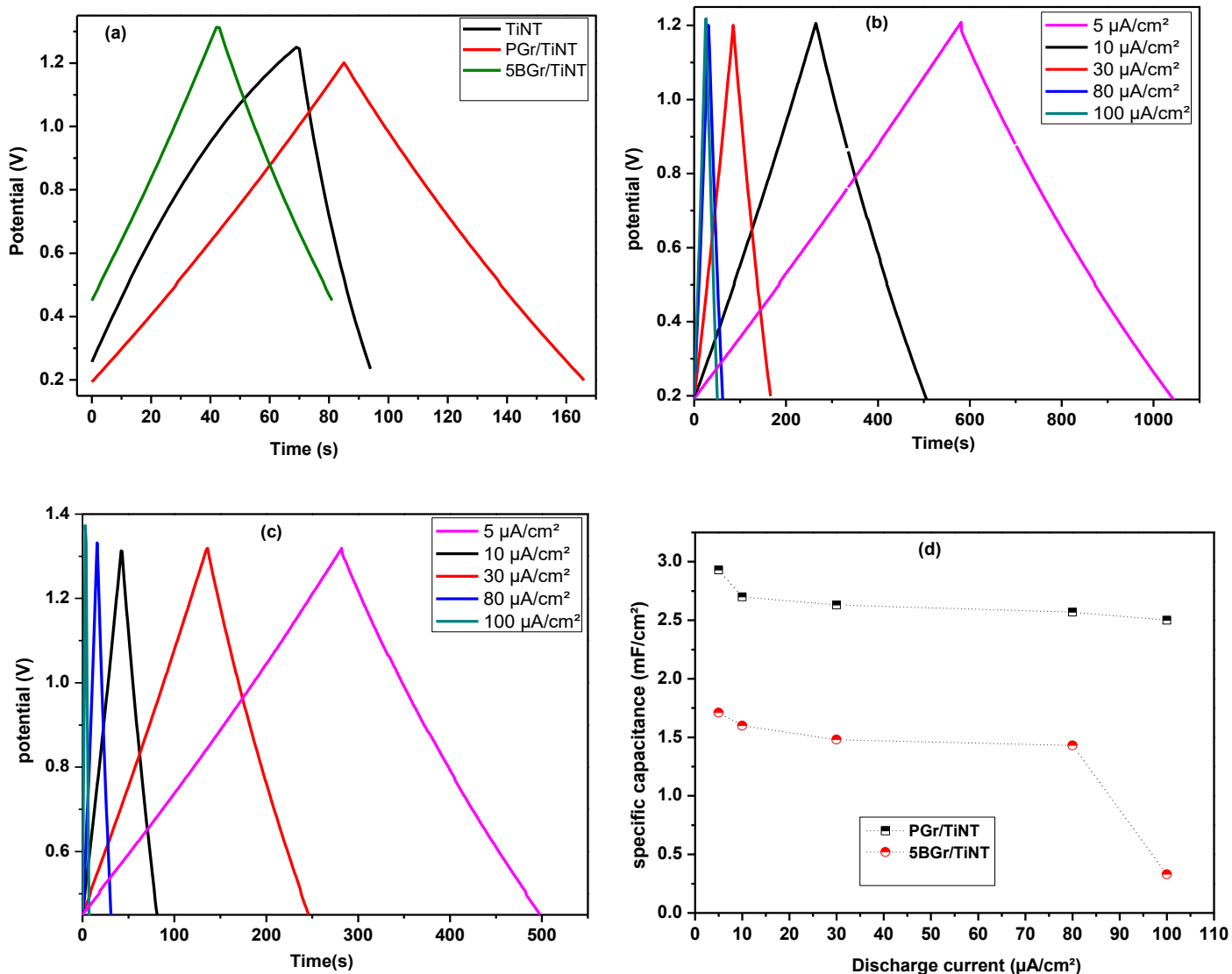


Figure IV. 8: (a) GCD curves of TiNT and Gr/TiNT at 30 $\mu\text{A}/\text{cm}^2$, (b) GCD curve of PGr)/TiNT at different current densities, (c) GCD curve of 5BGr/TiNT at different current densities and (d) Variation of areal specific capacitance at different discharge current densities.

The capacitances of Gr/TiNT electrodes were measured to be 2.63 and 1.48 $\text{mF}\cdot\text{cm}^{-2}$ at 30 $\mu\text{A}/\text{cm}^2$ for PGr/TiNT and 5BGr/TiNT respectively.

The areal specific capacitances of the electrodes at different current densities were calculated and presented in [figure IV.8 \(d\)](#). As can be seen, the specific capacitance of PGr/TiNT electrode was the higher whatever the current density. Furthermore, the specific capacitance values decrease with increasing current density due to reduced electrolyte ion diffusion at a faster time scale. Higher C_s values in PGr/TiNT electrodes may be a consequence of its lower amount of oxygen-containing functional groups. The specific capacitance of porous materials is strongly linked to the pore volume. Oxygen functional groups can lead to a reduction in the

effective pore volume and therefore prevent or block the penetration of ions into these areas where the double layers can be formed.

The reached areal capacitances are comparable or superior to those reported in the literature with other kinds of supercapacitors. Zheng et al. [37] have shown comparable areal capacitance of 2.25 mF/cm² for carbon-modified single-layered TiO₂ nanotubes. Mohammed et al. [38] have previously reported areal capacitance of 1.2 mF/cm² for a few-layer graphene nano-flake thin film. Sheng et al. [39] demonstrated areal specific capacitance of 0.48 mF/cm² on electrochemically reduced graphene oxide. Yadav et al. [40] revealed specific capacitance of 49.7 μF cm⁻² for TiO₂/graphene composite. Lower capacitances of 0.4 mF/cm², 0.087 mF/cm² and 0.02 mF/cm² were found on single-fiber based supercapacitors using graphene electrodes, vertically oriented graphene and Graphene fibers respectively [41, 42].

IV.5.2 EIS investigation

EIS is a very powerful technique for characterizing double layer capacitors at open circuit potential (OCP) and under bias. EIS analysis was first used to study the fundamental behavior of the electrode materials for supercapacitors at OCP. Nyquist and Bode plots of TiNT electrode showed a two-time constant model (Figure IV. 9 (a and b)). Nyquist plots of Gr/TiNT electrodes (Figure IV.9 (c)) show the presence of a very small arcs at low frequencies, followed by a short Warburg 45° lines, clearly indicating features of porous electrodes characterized by more efficient ionic diffusions into the electrolyte and proves that all reactive sites are entirely accessible in a very short time [43]. The straight lines in the low-frequency region are close to parallel to the Y-axis, characteristic of an EDLC systems. A nearly vertical line indicates good capacitive behavior without diffusion limitations. Supercapacitors can be modeled with a combination of resistive, Warburg and capacitive elements. A wide range of electronic equivalent circuits have been utilized to model EIS data for metal oxide and graphene/metal oxide electrodes. The EIS behavior of TiNT electrode can be well represented by the equivalent circuit model: $R_s(CPE_f [R_f(R_{ct} CPE_{dl})W])$, where one parallel R||CPE circuit is embedded within a second parallel R||CPE circuit. This model has been often used to describe porous electrodes (inset in Figure IV.9 (a)). Capacitances were replaced by double layer constant phase elements (CPE) to take into account the non-ideal behavior of the capacitive elements. In this model, R_s is the bulk solution resistance, R_f and CPE_f are the resistance and pseudocapacitance characterizing the electronic properties of the TiO₂ film. R_{ct} is the resistance of the charge transfer process at the film/electrolyte interface, CPE_{dl} is a double layer capacitance accompanying charge transfer processes at the interface

and W represents the diffusion-related Warburg element. The EIS behavior of Gr/TiNT electrode can be appropriately described by the equivalent circuit model: $R_s(C_{int}[R_{int}W])C_{dl}$ (inset in **Figure IV.9 (c)**). R_{int} represents the main resistive element (equivalent series resistance (ESR)); it arises from the total internal resistance of the cell, comprising resistance of the electrode material, ionic resistance of electrolyte and contact resistance at the interface of the active material/current collector. A high internal resistance results in: (i) reduced power output and energy production from the capacitor and (ii) short lifetime of the capacitor due to the heat generated inside the cell [44]. C_{int} is the interfacial contact capacitance between graphene and TiNT foil and C_{dl} the interfacial double layer capacitance. Introducing graphene into TiNT results in low R_{int} . R_{int} of the electrodes are all less than 1Ω , which means important electrical contact at the electrode/current collector interface and so suggest higher power output and energy production and longer lifetime of the capacitor.

Specific areal capacitances of the electrodes are found to be 2.46 and 2.03 mF/cm^2 for PGr/TiNT and 5BGr/TiNT respectively.

Complex capacitance analysis is considered as an excellent technique for investigating the interfacial electrochemical properties. The capacitance evolution as a function of frequency reflects how many electrolyte ions have attained the surface of the pores at a specific frequency.

The specific areal capacitance may be estimated based on the following equation:

$$C_s = -\frac{1}{2\pi f Z'' S} \quad (\text{IV.1})$$

where S is the apparent surface area of the electrode (1 cm^2), f the frequency and Z'' the imaginary part of the impedance.

Figure IV.9 (d) shows the specific areal capacitance versus frequency response. As can be seen, the capacitive behavior is maintained up to 1 kHz. Besides, the capacitance achieves its maximum at lower frequency since the ions have enough time to penetrate deep inside the pores of the electrodes and form a double layer on the surface of the electrode.

The areal capacitances of the electrodes are about 2.4, and 2.03 mF/cm^2 for PGr/TiNT and 5BGr/TiNT respectively. These values are strongly close to those obtained by fitting analysis, suggesting that EIS plots may be essentially modeled by a series RC circuit. Note also that these values agree well with the GCD extracted capacitances.

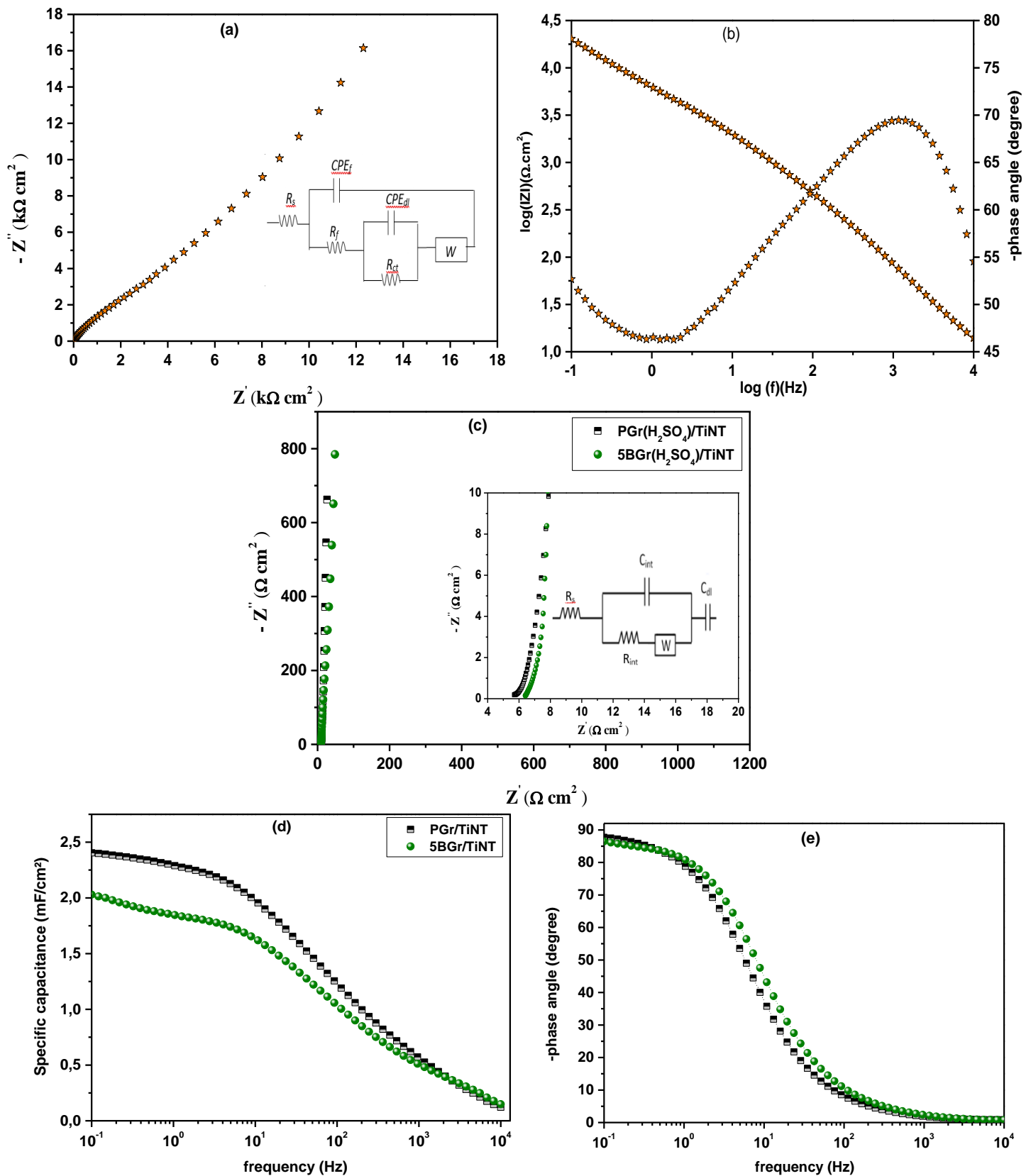


Figure IV. 9: (a and b) Nyquist and Bode spectra at OCP of TiNT electrode, (c) Nyquist spectra of Gr/TiNT electrodes at OCP, (d) specific areal capacitance versus frequency response of Gr/TiNT electrodes and (e) phase angle versus frequency response of Gr/TiNT.

Bode plots are also very useful to characterize the Gr/TiNT performances. It is well established that the closer the phase angle approaches 90° , the better the device performs. Flat regions and phase angles of about 87.7° and 86.5° at the lowest frequency are found for PGr/TiNT and 5BGr/TiNT respectively (Figure IV.9 (d)), revealing characteristic of a pronounced capacitive behaviors of PGr/TiNT electrodes. Phase angle of approx. 70° was found for TiNT electrode, implying its poor capacitive behavior.

EIS response of the electrode/electrolyte interface under bias have been also examined to investigate the electronic and conductive properties of the samples and to explore the dynamic trend of the electric double layer capacitance. To fully present our impedance data and to give a more general understanding on the influence of electrode potential on the impedance response of the interface, EIS data are presented in Nyquist and Bode plots. The phase angle plots are more sensitive to the system parameters and consequently provide a good way of comparing the model to experiment.

The potential was scanned from -0.8 to 0.4V, but the results presented in figure IV.10 are only for some potential. As can be clearly seen, impedance spectra of TiNT (Figure IV.10 (a and b)) performed at different applied potentials have almost the comparable features. For each potential, the total of two time constants can be identified, suggesting the occurring of two distinct processes. In addition, phase angle diagrams reveal dispersion due to R-CPE combination. It is also interesting to notice that the impedance amplitude increases significantly with increasing potential.

Impedance spectra of Gr/TiNT (Figure IV.10 (c-f)) have nearly the same characteristics. Nyquist plots reveal a very small arcs at high frequencies followed by a very short Warburg 45° lines at intermediate frequencies. At low frequencies, an almost vertical lines are clearly seen for PGr/TiNT electrode (Figure IV.10 (c)), whereas a slight deviation in vertical lines is observed for 5BGr/TiNT electrode (Figure IV.10 (e)). Bode diagrams show that at low frequencies, their phases increase with applied potential and both tend towards 90° thus becoming more capacitive. This behavior is particularly more pronounced for PGr/TiNT. Whereas, at higher frequencies the phase angles are closer to 0° and become more resistive. To acquire interfacial parameter values of the systems, a nonlinear least square fitting of impedance spectra was used. The best agreement between experiment and fitting was obtained with the equivalent circuits illustrated at the insert in figure IV.9 (a) and (c) for TiNT and PGr/TiNT respectively. For 5BGr/TiNT, the double layer capacitance was replaced by the double layer pseudo-capacitance. The functional groups were reported to be responsible for generating the pseudocapacitance contribution [45].

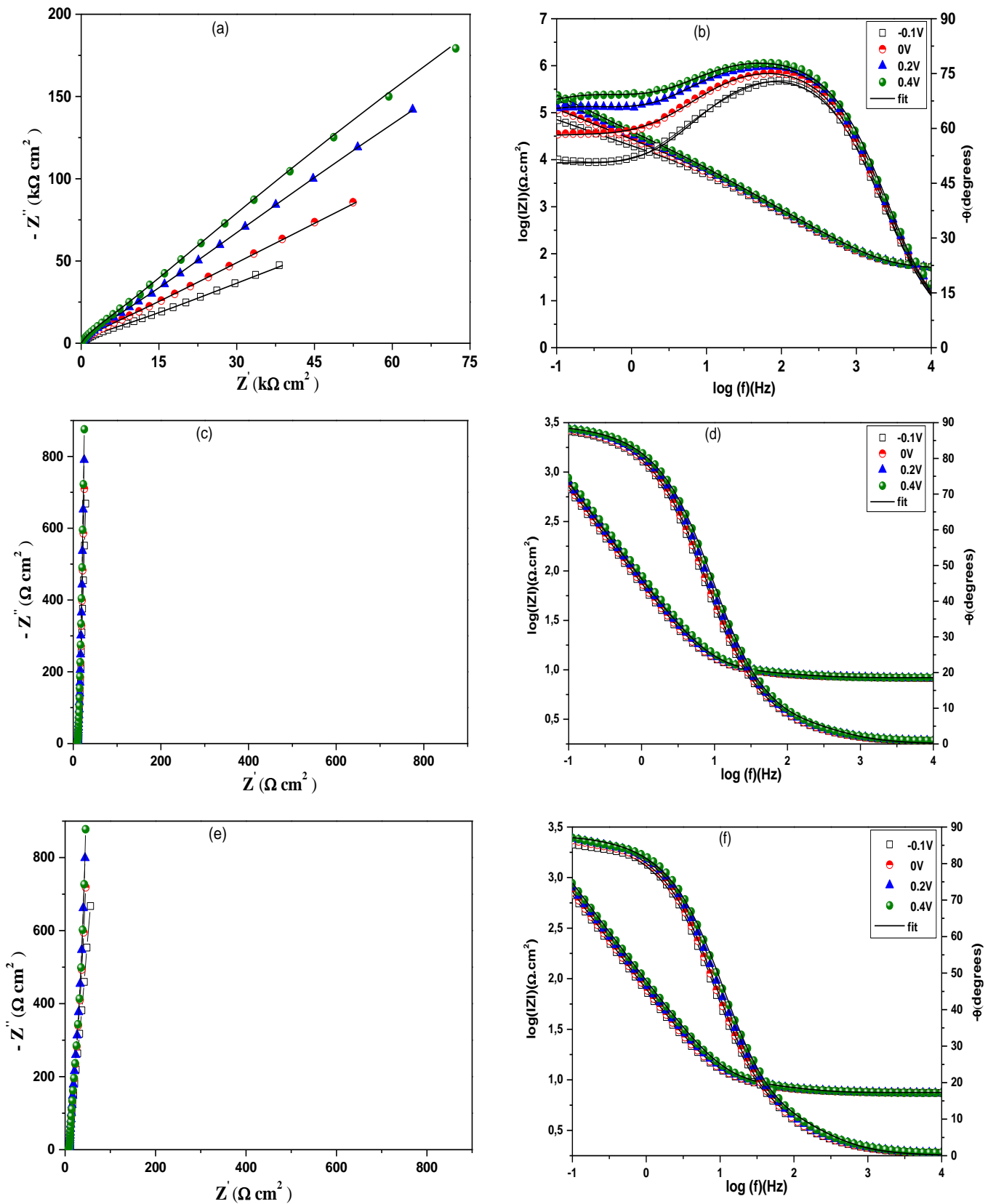


Figure IV.10: Nyquist and Bode representations under different bias of: (a-b) TiNT, (c-d) PGr/TiNT and (e-f) 5BGr/TiNT.

The occurrence of a CPE is a result of the dispersion of time constants which can be due to the non-uniform distribution of reaction sites at electrode surface [46] by a large presence of oxygen functional groups. The non-vertical slope of the low frequency impedance according to Nian and Teng [47], indicates the presence of oxides, inducing the non-ideality of the capacitive behavior.

The impedance of a CPE is given by:

$$Z_{CPE} = [Q(j\omega)^n]^{-1} \quad (IV.2)$$

where n is the CPE exponent, it indicates the angle of deviation of the impedance from a vertical line, and Q is the CPE parameter.

The fit curves (solid lines) and the experimental data are in good agreement, indicating that the equivalent circuit models accurately represent the electrochemical process occurring at the different electrodes.

Figure IV.11 (a) illustrates the values of R_{int} obtained by regression of EIS data for Gr/TiNT electrodes as a function of applied bias. R_{int} value obtained for PGr/TiNT is comprised, according to the applied potential, between 0.37 and 0.68 $\Omega.cm^2$. Whereas, it is comprised between 0.96 and 1.67 $\Omega.cm^2$ for 5BGr/TiNT. Lower R_{int} values of PGr/TiNT in the whole polarization range means it higher conductivity. The higher values of R_{int} for 5BGr/TiNT may be interpreted by the greater presence of oxygen functional groups, resulting in the reduction of the electrical conductivity of the electrode.

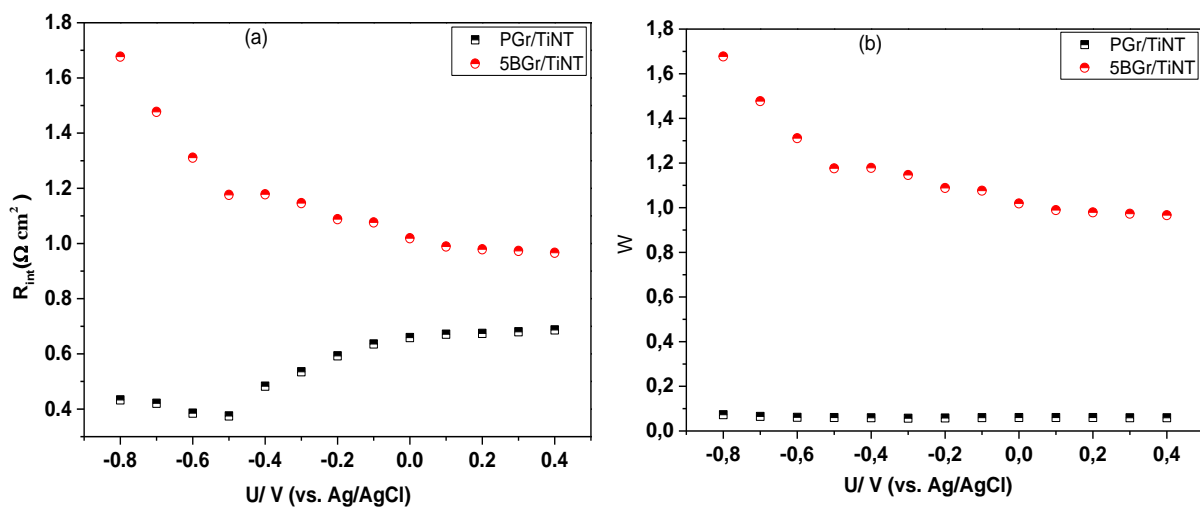


Figure IV.11: (a) interfacial resistance (R_{int}) evolution as a function of applied bias and (b) Warburg diffusion impedance evolution as a function of applied bias.

The Warburg diffusion impedance, which measures the degree of difficulty of entering the pores is also evaluated as a function of applied bias (Figure IV.11 (b)). As can be seen, Warburg impedance of 5BGr/TiNT is potential dependent, W lies from 1.67 at -0.8V to 0.86 at 0.4V, which are much higher than that of PGr/TiNT (W ranges from 0.057 to 0.073 according to the applied potential). So, one may suggest less ion diffusion and a greater difficulty for ions to reach the pores of 5B/TiNT. These findings are in good agreement with previous reports. According to He et al. [48], too many oxygen functional groups will, to some extent, hinder the transport of ions into the pores, which increases the Warburg impedance. As the oxygen functional groups on surface cause the decrease of the specific surface area and hinder the migration of electrolyte in the micropores, Kim et al. [45], demonstrated that Warburg impedance gradually increase with increasing the oxygen content.

In order to investigate the electronic and conductive properties of Gr/TiNT samples, M-S characterizations were carried out. The differential capacitance (C_{dl}) of the electric double layer at the interface is mainly composed of the semiconductor electrode capacitance (C_{sc}), which is the result of the depletion of electrons in the SCR of the electrode and the solution charge layer capacitance (C_d), which are connected in series to each other:

$$\frac{1}{C_{dl}} = \frac{1}{C_{sc}} + \frac{1}{C_d} \quad (IV.3)$$

In the Gouy-Chapman-Stern model, the solution charge layer is separated into the compact layer (Helmholtz layer), which is the result of corresponding counter ions and the Gouy-Chapman layer, from the diffusive electrolyte. So, the differential capacitance in the electrolyte can be conceived as a series connection of two capacitances, that of the Helmholtz layer (C_H) and that of the diffuse charge layer (C_{GC}):

$$\frac{1}{C_d} = \frac{1}{C_H} + \frac{1}{C_{GC}} \quad (IV.4)$$

So, the capacitance can be resolved into three distinct components arranged in series:

$$\frac{1}{C_{dl}} = \frac{1}{C_{sc}} + \frac{1}{C_H} + \frac{1}{C_{GC}} \quad (IV.5)$$

C_{sc} is the smallest of the three capacitances and therefore will dominate in the inverse sum:

$$\frac{1}{C_{dl}} \approx \frac{1}{C_{sc}} \quad (IV.6)$$

Any change in applied potential will be dominated by the potential change in the space charge layer of the electrode.

For Gr/TiNT electrodes, C_{dl} values obtained from the fitting procedure were taken for the M-S analysis. Concerning TiNT electrode, the space charge layer capacitance per surface unit was calculated from the fitting parameters, using a general expression developed for surface distributions of capacitance, established by Brug et al. [49].

M-S plots of TiNT and Gr/TiNT electrodes (Figure IV.12) exhibited M-S behaviour with distinct slopes. These slopes are positive, which is typical of n-type semiconductor behaviour. M-S curve of pristine TiNT electrode (Figure IV.12 (a)) reveals that the oxide layers are getting fully depleted for U up to around -0.65 V. An inflection point is noticed at about -0.2 V, after this voltage, the slope is lowered. As suggested in the previous chapter, the appearance of two slopes in the M-S plots may be related to the presence of both shallow and deep level donor species. The introduction of Gr into TiNT resulted in single slopes, which are very much smaller than that of TiNT (Figure IV.12 (b)). In addition, one may notice a negative shift of U_{FB} from -0.65 V for TiNT to values below -0.9 V for Gr/TiNT systems. The negative U_{fb} displacement in the Gr/TiNT systems indicates an increase in band edge bending, which is beneficial to the transfer of photogenerated charge carriers. Graphene caused also a strong increase in conductivity on the Gr/TiNT material when compared with TiNT. A dramatic increase in the carrier density of TiNT when loaded with graphene is noticed. Donor densities of the Gr/TiNT materials are 6.5×10^{24} and $4.67 \times 10^{24} \text{ cm}^{-3}$ for PGr/TiNT and 5BGr/TiNT respectively, which are orders of magnitude higher than that of unmodified TiNT ($1.6 \times 10^{18} \text{ cm}^{-3}$).

The increased electron density of Gr/TiNT materials may be caused by the high electrical conductivity of graphene, which is a consequence of its exclusive electronic properties. It has been reported that graphene electrons act in the same way as photons in terms of their mobility due to their zero effective mass [50]. So graphene is characterized by extremely high carrier mobility. These properties are derived from its exceptional electronic band structure, which is considered a zero-coverage semi-metal. The higher electrical conductivity of PGr/TiNT material demonstrates also that the graphene materials carried relatively lower amount of oxygen functional groups.

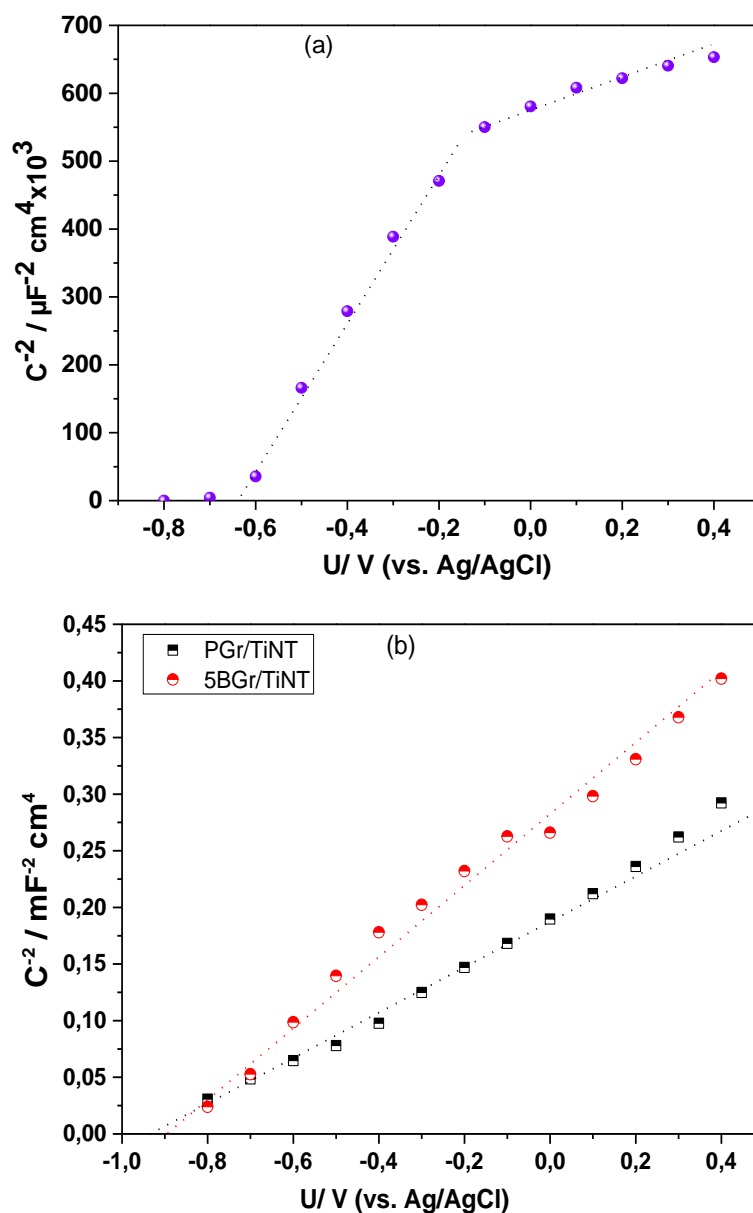


Figure IV.12: M-S plots of (a) TiNT and (b) Gr/TiNT.

IV.5.3 CV analysis

CV is considered as an efficient procedure to further validate the capacitive nature of the different electrodes. CV experiments were carried out at scan rates ranging from 10 to 500 mV/s. Since the curves are indiscernible at lower scan rates, [figure IV.13 \(a-b\)](#) shows the CV curves of Gr/TiNT electrodes at scan rates of 100, 250 and 500 mV/s only. As can be seen, all of the CV curves had nearly a similar and quasi rectangular shape over a potential window of 1V. Furthermore, the current density of the electrodes increases at higher scan rates, which

proves the supercapacitor nature of the composites. It is also interesting to notice that the integrated area increased with scan rate and exhibited a nearly rectangular shape even at scan rates of 500 mV/s, which is an indication of capacitive charge storage.

Among the areas of the CV curves of Gr/TiNT electrodes, that of PGr(H₂SO₄)/TiNT is the highest.

Areal C_s of the electrodes are calculated from the CV curves. At higher scan rate of 500 mV/s, C_s is about 1.65 and 1.24 mF/cm² for PGr/TiNT and 5BGr/TiNT respectively. The obtained C_s values are mainly consistent with the order indicated by the Nyquist plots and GCD curves. Ragone plot compares electrochemical devices based on their energy density, characterizing the total amount of charge able to be stored in the device and their power density, the speed at which a device can be charged or discharged.

Ragone plots presented in [figure IV.13\(c\)](#) illustrate the relation between the areal specific energy density (E) and the areal specific power density (P). The energy density of PGr/TiNT electrode is considerably higher than the other. PGr/TiNT electrode reaches the highest power density of 50 μW cm⁻² and the maximum energy density of 0.35 μWh cm⁻². These values are also much higher than those of other graphene-TiO₂ based supercapacitors reported recently [\[51\]](#) and those of 3D graphene fiber in which the energy density ranges from 0.04 to 0.17 μWh cm⁻² [\[52\]](#).

The cycling performance of every electrode is another important factor to consider for its real time applications. Under realistic conditions of a supercapacitor, the electrodes must have high cyclic stability for a long period of time. [Figure IV.13 \(d\)](#) shows the capacitance retention values of PGr/TiNT and 5BGr/TiNT electrodes achieved after running 1000 cycles using cyclic voltammetry. From the figure, it is clear that the loss of capacitance of both electrodes is little during the cycles. PGr/TiNT and 5BGr/TiNT exhibit reduced capacitance retention of 98.6% and 95.4% respectively after 1000 cycles. Such higher retention values can be attributed to the fact that graphene sheets are strongly impregnated in the TiNT surface as already mentioned in XRD analysis.

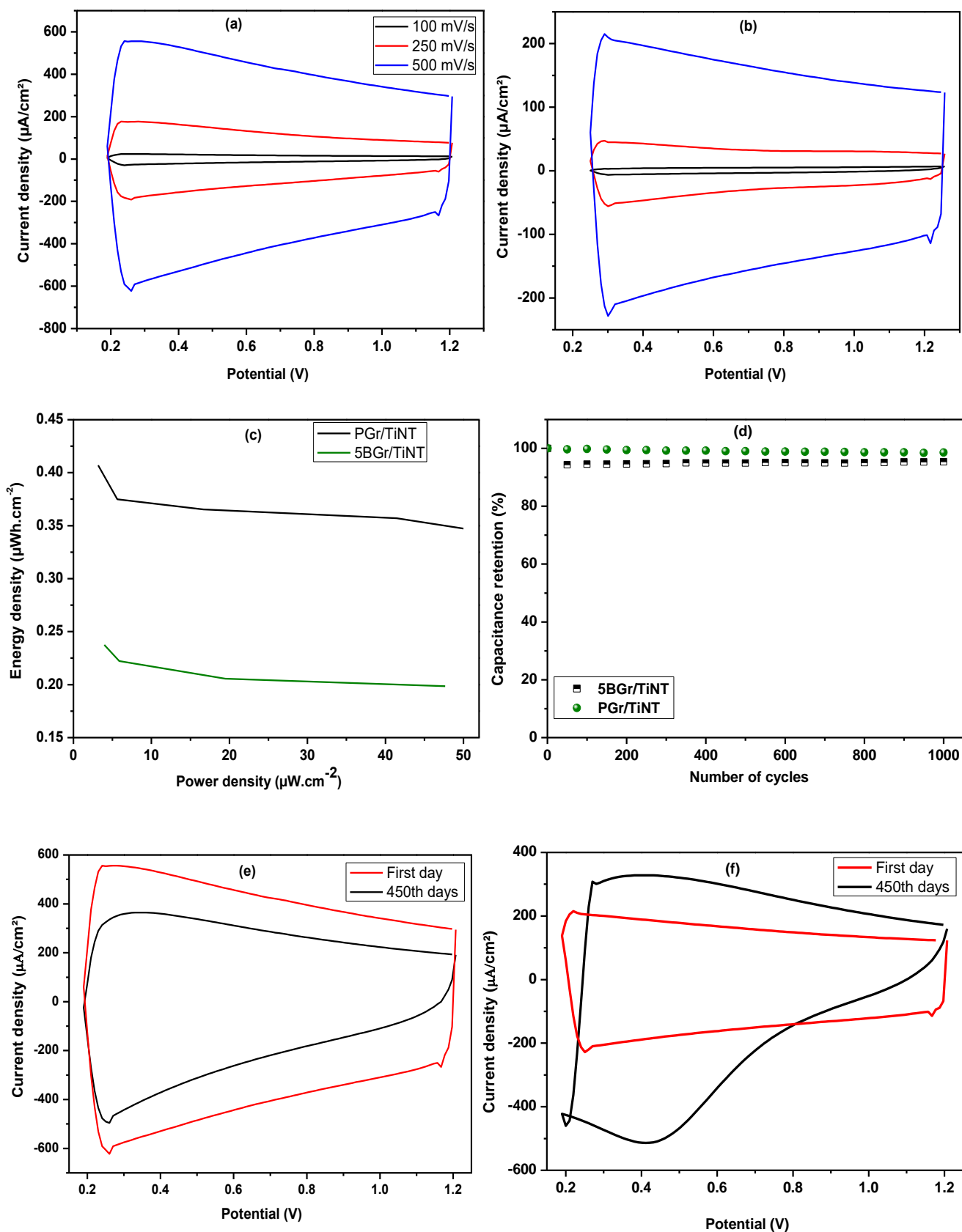


Figure IV.13: CV curves of (a) PGr/TiNT electrode and (b) 5BGr/TiNT electrode at scan rates of 100, 250 and 500 mV/s. (c) Ragone plot of Gr/TiNT, (d) Capacitance retention behavior of Gr/TiNT electrodes for 1000 cycles. CV curves of (e) PGr/TiNT electrode and (f) 5BGr/TiNT electrode at a scan rate of 500 mV/s after extended time of 450 days.

Furthermore, in order to evaluate the stability of both Gr/TiNT electrodes, the specific capacitance was measured after an extended period of 450 days during which various experiments and numerous cycles were conducted. **Figure IV.13 (e-f)** shows the cyclic voltammetry curves of the Gr/TiNT electrodes obtained at the first day and the 450th day. A moderate change in the CV curve (**Figure. IV.13 (e)**) and a slight decrease in the specific capacitance are noticed for PGr/TiNT electrode, showing capacitance retention of 88%, implying that this electrode retains its activity over a much extended time period. The CV curve of the 5BGr/TiNT electrode (**Figure IV.13 (f)**) has fully lost its initial quasi-rectangular shape. Nevertheless, it has retained 84% of its initial capacity. After a prolonged time, a higher amount of oxygen functional groups leads to the formation of a passive layer, which hinders the flow of the ions in the deeper pores, thus limiting the EDLC performance.

By considering all the above electrochemical results, it can be concluded that PGr modified TiNT electrode is the most stable and displays the most efficient supercapacitive behavior. Consequently, this electrode can be regarded as promising materials in the supercapacitor application.

IV.6 Photocatalytic performance of the electrodes

To compare the photocatalytic efficiencies of the different electrodes, a series of photodegradation experiments were carried out by using MB as a model pollutant under simulated sunlight. **Figure IV.14 (a-c)** illustrates the UV-vis absorption spectra of MB solution illuminated by the visible light for different exposure times in the presence of TiNT and Gr/TiNT electrodes. All UV-vis absorption spectra show that the absorbance peaks of MB for all samples decrease with the increase of reaction time, indicating good photodegradation activity of the samples. PGr/TiNT show higher photocatalytic activity for MB degradation than the others. Indeed, the absorbance of the spectra rapidly decreases with increasing irradiation time.

The quantification of the photocatalytic behavior of the samples was achieved by the calculation of the relative changes in the concentration of MB. The results of photocatalytic MB degradation over the different photocatalysts are shown in **figure IV.14 (d and e)**.

Compared to TiNT, Gr/TiNT exhibits better photocatalytic activity for MB degradation. Moreover, PGr/TiNT electrode displays significantly improved photodegradation efficiency to MB, achieving a degradation percentage of about 60% in 2 hours.

The photocatalytic degradation of MB dye by Gr/TiO₂ nanostructures has been already studied. In the majority of cases, after few hours of visible exposure, the initial MB concentration was reduced to about 20-40% [53-56], while in other works a complete reduction has also been mentioned [57].

The improvement in the photocatalytic degradation of MB dye by the PGr/TiNT electrode may be linked to the interaction effect of graphene. The presence of conductive graphene promotes the adsorption ability of MB on the surface and enhances the lifetime of the generated electron/hole pairs, acting as photosensitizer. By using transient absorption spectroscopy measurements, Williams et al. [58] showed that transfer of photoexcited electrons from graphene to TiO₂ occurs faster than charge recombination. In addition, the recombination of photoexcited electrons and holes in the composite materials is slower than that in TiO₂ alone. By theoretical calculations, Masuda et al. [59] have also supported the high transfer rate of photoexcited electrons from graphene to TiO₂ nanosheets and demonstrated the ability of visible light-induced charge transfer photoexcitation from graphene to TiO₂.

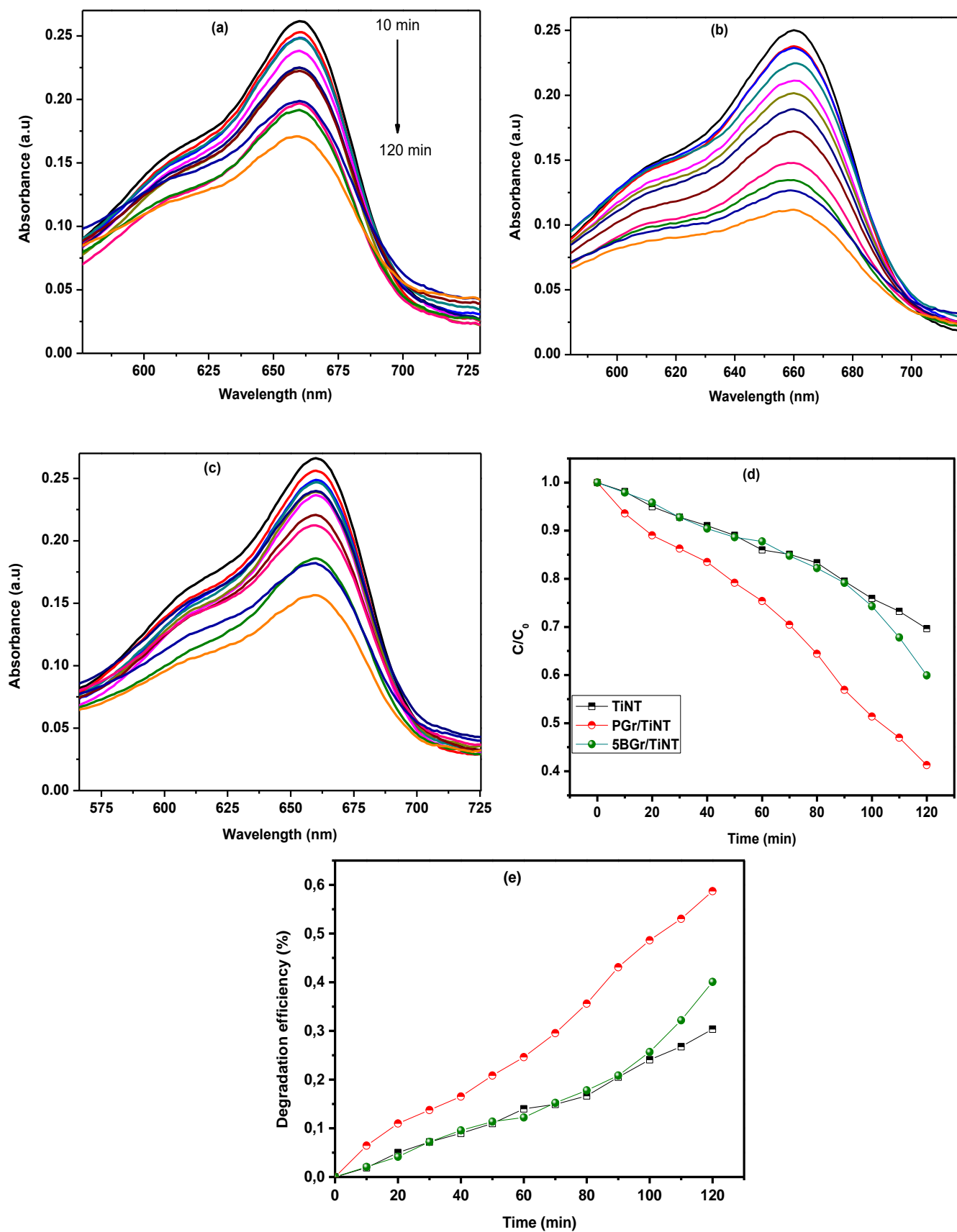


Figure V.14: UV-vis absorption spectra of MB solution in the presence of: (a) TiNT, (b) PGr/TiNT, and (c) 5BGr/TiNT, (e) C/C₀ under visible light and (f) corresponding photocatalytic degradation efficiency under visible light for the different photocatalysts.

Conclusion

In the present work, graphene-modified TiNT electrodes were successfully prepared by anodization and electrochemical deposition processes.

The following conclusions have been drawn:

- High quality, i.e. impurity-free and unoxidized graphene with high electric conductivity was achieved by exfoliating pure graphite in H_2SO_4 solution.
- Donor density of graphene modified TiNT is orders of magnitude higher than that of unmodified TiNT, which may be related to the high electrical conductivity of graphene as a consequence of its extremely high carrier mobility.
- The introduction of graphene in TiNT results in a decrease of the photoluminescence intensity, demonstrating an enhanced charge separation of electron hole pairs when compared to TiNT.
- The electrical double layer capacitance nature of the Gr/TiNT electrodes was confirmed by CV, galvanostatic charge-discharge and EIS analysis.
- Graphene with high electrical conductivity, low amount of oxygen-containing functional groups and free impurities modified TiNT system has been found to be the better candidate for achieving both higher capacitance and higher MB photocatalytic degradation.
- The presence of oxygen functional groups have a significant effect on the capacitive properties, as they may block ions from reaching the pores and hence lowering the specific capacitance.
- From galvanostatic charge-discharge tests, PGr/TiNT electrode exhibited an extended charge-discharge time, perfect symmetry and the highest specific capacitance of $2.6 \text{ mF}\cdot\text{cm}^{-2}$ at $30 \mu\text{A}/\text{cm}^2$.
- From EIS analysis, higher value of interfacial resistance for 5BGr/TiNT is connected to the greater presence of oxygen functional groups, resulting in the reduction of the electrical conductivity of the electrode.
- PGr/TiNT electrode reached the highest power density of $50 \mu\text{W cm}^{-2}$ and the maximum energy density of $0.35 \mu\text{Wh cm}^{-2}$. Furthermore, it showed a very good stability. Capacitance retention of 98% was demonstrated after 1000 cycles and of 88% after extended time period of 450 days.
- Gr/TiNT electrodes exhibited photocatalytic activities that are greater than that of TiNT, thanks to the combined action of graphene as a photosensitizer.

References

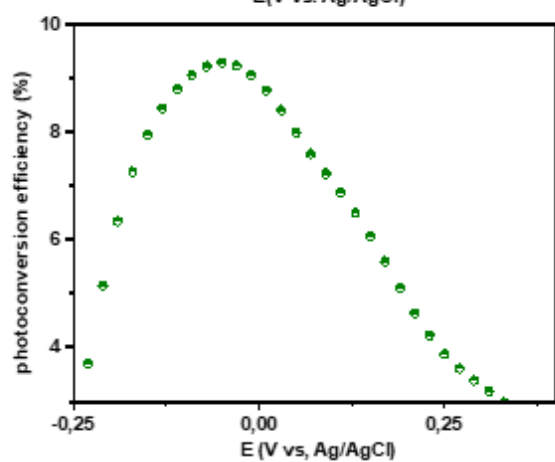
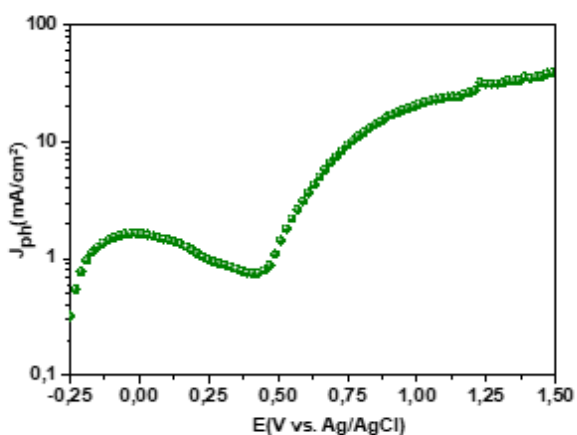
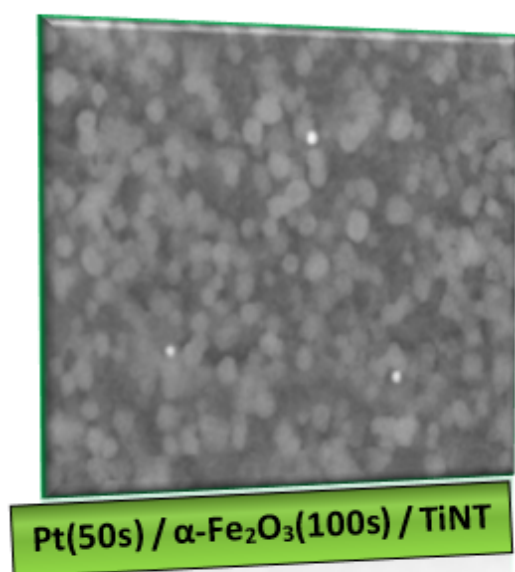
- [1] L. Aïnouche, L. Hamadou, A. Kadri, N. Benbrahim, D. Bradai, *Solar Energy Materials & Solar Cells*, 151(2016)179.
- [2] S. Ait Ali Yahia, L. Hamadou, M. J. Salar-García, A. Kadri, V. M. Ortiz-Martínez, F. J. Hernández-Fernández, A. Pérez de los Rios, N. Benbrahim, *Applied Surface Science*, 387(2016)1037.
- [3] G. Williams, B. Seger, and P. V. Kamat, *ACS Nano*, 2(2008)1487.
- [4] S. Bae, H. Kim, Y. Lee, X. Xu, J. S. Park, Y. Zheng, *Nature Nanotechnology*, 5(2010)574.
- [5] K. V. Emtsev, A. Bostwick, K. Horn, J. Jobst, G. L. Kellogg, L. Ley, J. L. McChesney, T. Ohta, S. A. Reshanov, J. Rohrl, E. Rotenberg, A. K. Schmid, D. Waldmann, H. B. Weber, T. Seyller, *Nature Materials*, 8(2009)203.
- [6] A.M. Abdelkader, A.J. Cooper, R.A.W. Dryfe, I.A. Kinloch, *Nanoscale* 7(2015)6944.
- [7] J. Zhang, J. Jiang, H. Li, X. S. Zhao, *Energy Environmental Science*, 4(2011)4009.
- [8] Q. Xiang, J. Yu, M. Jaroniec, *Chemical Society Reviews*, 41(2012)782.
- [9] H. Su, T. Wang, S. Zhang, J. Song, C. Mao, H. Niu, B. Jin, J. Wu, Y. Tian, *Solid State Sciences*, 14(2012)677.
- [10] K. Parvez, Z. S. Wu, R. Li, X. Liu, R. Graf, X. Feng, et al., *Journal of the American Chemical Society*, 136(2014)6083.
- [11] H. Lee, J. I. Choi, J. Park, S. S. Jang, S. W. Lee, *Carbon*, 167(2020)816.
- [12] N. T. Padmanabhan, N. Thomas, J. Louis, D. T. Mathew, P. Ganguly, H. John, S. C. Pillai, *Chemosphere*, 271(2021)129506.
- [18] G. Zhou, F. Li, H. M. Cheng, *Energy and Environmental Science*, 7(2014)1307.
- [13] V. H. Pham, T.D. Nguyen-Phan, X. Tong, B. Rajagopalan, J. S. Chung, J. H. Dickerson, *Carbon*, 126(2018)135.
- [14] X. Lu, G. Wang, T. Zhai, M. Yu, J. Gan, Y. Tong, Y. Li, *Nano Letters*, 12(2012)1690.
- [15] Y. Xie, D. Fu, *Materials Research Bulletin*, 45(2010)628.
- [16] M. S. Kim, T.W. Lee, J. H. Park, *Journal of the Electrochemical Society*, 156(2009)A584.
- [17] A. Viinikanoja, Z. Wang, J. Kauppi, C. Kvarnstrom, *Chemistry Physics*, 14(2012)14003.
- [18] J. Wang, X. Nie, W. Wang, Z. Zhao, L. Li, Z. Zhang, *Optik - International Journal for Light and Electron Optics*, 242 (2021)167245.
- [19] D. Zheng, Y. Xin, D. Ma, *Catalysis Science and Technology*, 6(2015)1892.

- [20] P. Dong, Y. Wang, L. Guo, B. Liu, S. Xin, J. Zhang, Y. Shi, W. Zeng and S. Yin, *Nanoscale*, 4 (2012)4641.
- [21] S. H. Othman, S. A. Rashid, T. I. Mohd Ghazi, N. Abdullah, *Journal of Nanomaterials*, 1(2012)2012.
- [22] G. D. Tarigh, F. Shemirani, N. S. Mazhari, *RSC Advances*, 5(2015)35070.
- [23] J. Laisney, A. Rosset, V. Bartolomei, D. Predoi, D. Truffier-Boutry, S. Artous, V. Bergé, G. Brochard, I. Michaud-Soret, *Environmental Science : Nano*, 8(2021)297.
- [24] T. Sakthivel, V. Gunasekaran S. J. Kim, *Materials Science in Semiconductor Processing*, 19(2014)174.
- [25] A. León, P. Reuquen, C. Garín, R. Segura, P. Vargas, P. Zapata, P. A. Orihuela, *Applied Science*, 7(2017)49.
- [26] C. Zhang, D.M. Dabbs, L.M. Liu, I.A. Aksay, R. Car, A. Selloni, *Journal of Physical Chemistry*, 119(2015)18167.
- [27] B. Qiu, Y. Zhou, Y. Ma, X. Yang, W. Sheng, M. Xing and J. Zhang, *Scientific Reports*, 5(2015)8591.
- [28] Y. Qiao, C. M. Li, S. J. Bao and Q. L. Bao, *Journal of Power Sources*, 170(2007)79.
- [29] J. Wei, L. Zhao, S. Peng, J. Shi, Z. Liu, W. Wen, *J. Sol–Gel Science and Technology*, 47(2008)311.
- [30] H. Zhang, X. Lv, Y. Li, Y. Wang, J. Li, *ACS Nano*, 4(2009)380.
- [31] N. S. Singh, F. Mayanglambam, H. B. Nemade, P. K. Giri, *RSC Advances*, 11(2021)9488.
- [32] J. Li, Z. Tang and Z. Zhang, *Chemistry of Materials*, 17(2005)5848.
- [33] M. Okubo, E. Hosono, J. Kim, M. Enomoto, N. Kojima, T. Kudo, H. S. Zhou, I. Honma, *Journal of the American Chemical Society*, 129(2007)7444.
- [34] T. Brousse, M. Toupin, R. Dugas, L. Athouël, O. Crosnier, D. Bélanger, *Journal of Electrochemical Society*, 153(2006)A2171.
- [35] V. Augustyn, P. Simon, B. Dunn, *Energy & Environmental Science*. 7(2014)1597.
- [36] R. Liu, W. Guo, B. Sun, J. Pang, M. Pei, G. Zhou, *Electrochimica Acta*, 156(2015)274.
- [37] L. Zheng, Y. Dong, H. Biana, C. Lee, J. Luc, Y.Y. Li, *Electrochimica Acta* 203(2016)257.
- [38] M. M. M. Mohammed, D-M. Chun, *Coatings*, 8(2018)302.
- [39] K. Sheng, Y. Sun, C. Li, W. Yuan, G. Shi, *Scientific Reports*, 2(2012)247.
- [40] P. Yadav, K. Pandey, P. Bhatt, B. Tripathi, M. K. Pandey, M. Kumar, *Materials Science and Engineering B* 206(2016)22.

- [41] J. R. Miller, R. A. Outlaw, B. C. Holloway, *Science*, 329(2010)1637.
- [42] Y. Meng, Y. Zhao, C. Hu, H. Cheng, Y. Hu, Z. Zhang, G. Shi, L. Qu. *Advanced Materials* 25(2013)2326.
- [43] J. P. Diard, B. Le Gorrec, C. Montella, *J. Electroanalytic Chemistry*, 471(1999)126.
- [44] C. Lei, F. Markoulidis, Z. Ashitaka, C. Lekakou, *Electrochimica Acta* 92(2013)183.
- [45] M. Kim, I. Oh, J. Kim, *Electrochimica Acta* 196(2016)357.
- [46] J. Zheng, S. S. Moganty, P. C. Goonetilleke, R. E. Baltus and D. Roy, *The Journal of Physical Chemistry C*, 115(2011)7527.
- [47] Y-R Nian, H. Teng, *Journal of Electroanalytical Chemistry* 540(2003)119.
- [48] Y. He, Y. Zhang, X. Li, Z. Lv, X. Wang, Z. Liu, X. Huang, *Electrochimica Acta*, 282(2018)618.
- [49] G.J. Brug , A.L.G. Van-Den-Eeden, M. Sluyters-Rehbach , J.H Sluyters, *The Journal of Electroanalytical Chemistry*. 176(1984)275.
- [50] A. Chenna, L. Hamadou, N. Benbrahim, A. Kadri, S. Boudinar, *Journal of Electroanalytical Chemistry*, 802(2017)118.
- [51] G. K. Veerasubramani, K. Krishnamoorthy, P. Pazhamalai, S. J. Kim, *Carbon*, 105(2016)638.
- [52] L. Fornasini, S. Scaravonati, G. Magnani, A. Morengi, M. Sidoli, D. Bersani, G. Bertoni, L. Aversa, R. Verucchi, M. Ricco, P. P. Lottici, D. Pontiroli, *Carbon*, 176(2021)296.
- [53] Y. Meng, Y. Zhao, C. Hu, H. Cheng, Y. Hu, Z. Zhang, G. Shi, L. Qu, *Advanced Material*, 25(2013)2326.
- [54] M. Z. Ge, S. H. Li, J. Y. Huang, K. Q. Zhang, S. S. Al-Deyab, Y. K. Lai, *Journal of Materials Chemistry*, 3(2015)3491.
- [55] H. Zhang, X. Lv, Y. Li, Y. Wang, J. Li, *ACS Nano* 4(2010)380.
- [56] J.S. Lee, K.H. You, C.B. Park, *Advanced Material*, 24(2012)1084.
- [57] X. Pan, Y. Zhao, S. Liu, C.L. Korzeniewski, S. Wang, Z. Fan, *ACS Applied Materials & Interfaces*, 4(2012)3944.
- [58] K. J. Williams, C. A. Nelson, X. Yan, L.-S. Li, X. Zhu, *ACS Nano*, 7(2013)1388.
- [59] Y. Masuda, G. Giorgi, K. Yamashita, *Physica Status Solidi B*, 251(2014)1471.

Chapter V

Fabrication of $\alpha\text{-Fe}_2\text{O}_3/\text{TiO}_2$, Pt/TiO_2 and $\text{Pt}/\alpha\text{-Fe}_2\text{O}_3/\text{TiO}_2$ nanotubes for efficient visible light photoelectrochemical water splitting



Graphical abstract

Introduction

Nowadays, energy sources from fossil fuels are restricted and cause environmental pollution, a common problem that can be remedied by renewable energies. Renewable energy sources are recognized as a promising technology to obtain energy from natural resources. Hydrogen (H_2) is an attractive alternative solution to provide energy in the future due to its high efficiency and cleanliness [1]. There are several methods of producing H_2 from sunlight, among them photoelectrochemical (PEC) water splitting is considered as a potentially more practical approach for harvesting solar energy. Many semiconducting materials have been researched as photoelectrodes in a PEC water splitting process. Nanostructured TiO_2 was the most widely studied photoanode material owing to its suitable band positions for photocatalytic H_2 production. To overcome the two major obstructions of TiO_2 and to improve PEC performances, combination of TiO_2 with narrower band gap semiconductor is regarded as an effective way [2-6]. Among different narrower band gap semiconductors, hematite ($\alpha-Fe_2O_3$) is regarded as a promising photoanode material because of the suitable band gap (~ 2.2 eV) for sunlight harvesting, excellent stability under ambient conditions. It is suitable for the collection of a large fraction of the visible photons with appropriately aligned energy levels at the boundary to perform the photoelectrochemical reaction of water oxidation [7, 8]. It has been the subject of intense research for several decades. In spite of these features, Fe_2O_3 suffers from slow carrier transport and short life time of charge carriers (~ 10 ps) [9], hindering the improvement of the PEC performance. In this sense, to further enhance carrier transport process, avoid recombination and extend the spectral response towards the visible spectral range of Fe_2O_3/TiO_2 photoanodes, decorating the system with noble metals (Au, Ag, Cu, Pd, Pt...) are the most common strategies utilized. Plasmonic metals may extend light absorption to visible region through localized surface plasmon resonance (LSPR) effects. Besides, the Schottky barriers that are formed when the noble metal comes into contact with the semiconductor promote the separation of electrons and holes, which significantly contributes to the reduction of electron-hole pair recombination rates. The commonly investigated nanoparticles are Au or Ag because of their LSPR excitations in the visible spectral window. Pt is the most uninvestigated due to its LSPR modes being in the UV spectral region. Pt nanoparticles display LSPR bands that are generally below 450 nm, which may be boosted in the vis-NIR region by modifying the shape, size, and interparticle distance as previously demonstrated in recent works [10, 11]. According to Bigall et al. [10], the maximum of plasmonic absorption may be adjusted from 400 to 494 nm by extending the size of the Pt nanoparticles from 73 to 107 nm. Moreover, for low interparticle distances, plasmonic coupling

results in a significant redshift (from 650 to 750 nm), enhancement and broadening of LSP peak [11].

Several methods have been directed toward the fabrication of α -Fe₂O₃/TiNT heterojunction, one can site atomic layer deposition (ALD) technique by Liu [12], vapor-phase process [13], hydrothermal method [14] and electrodeposition [15]. The commonly used synthesis methods toward the fabrication of plasmonic Pt photocatalysts, include photoreduction [16], sol-gel [17], atomic layer deposition technique [18] and electrodeposition [19].

Comparatively to other techniques, electrodeposition is an easy and environmentally friendly technique to synthesise materials with controllable morphology by adjusting electrochemical parameters, such as applied potential and time of exposition [20], which may impact on the photoelectrochemical activity of the heterojunctions.

Inspired by the multiple effects of both α -Fe₂O₃ and Pt on TiNT, in the present work we have investigated three types of systems for PEC water splitting applications on TiNT: (i) α -Fe₂O₃/TiNT, (ii) Pt/TiNT and (iii) Pt/ α -Fe₂O₃/TiNT composites. The size, distribution density and morphology of both α -Fe₂O₃ and Pt nanoparticles can be tailored by simply tuning the deposition duration. While there have been few reports on the synthesis of α -Fe₂O₃ films on TiNT, to the best of our knowledge no reports have been devoted on the synthesis of Pt/ α -Fe₂O₃ on TiNT by two-step electrodeposition. Herein, we demonstrated that Pt/TiNT and Pt/ α -Fe₂O₃/TiNT composites improved high PEC water splitting efficiencies under visible light irradiation compared to those of unmodified TiNT and α -Fe₂O₃/TiNT.

V. 1 Synthesis of TiNT based heterojunctions

V.1.1 Synthesis of α -Fe₂O₃/TiNT heterostructure

TiNT were synthesized by a two-step electrochemical anodization. α -Fe₂O₃/TiNT heterostructure was synthesized combining electrodeposition and thermal oxidation. γ -FeOOH was used as a starting precursor to produce α -Fe₂O₃ via thermal annealing. So, γ -FeOOH particles were first potentiostatically electrodeposited by applying a constant voltage of -1.2V for a duration of 25, 50 and 100s in an aqueous acidic solution (pH 3.4) containing 50 mM of FeSO₄ and distilled water. In the used pH, Fe²⁺ ions are soluble without the addition of complexing agents.

The schematic of the fabrication process of α -Fe₂O₃/TiNT electrode is illustrated in **scheme V.1(a)**. Firstly, TiNT were fabricated by the secondary anodization method. γ -FeOOH particles were electrochemically deposited onto the TiNT electrode. Then, the γ -FeOOH/TiNT electrode

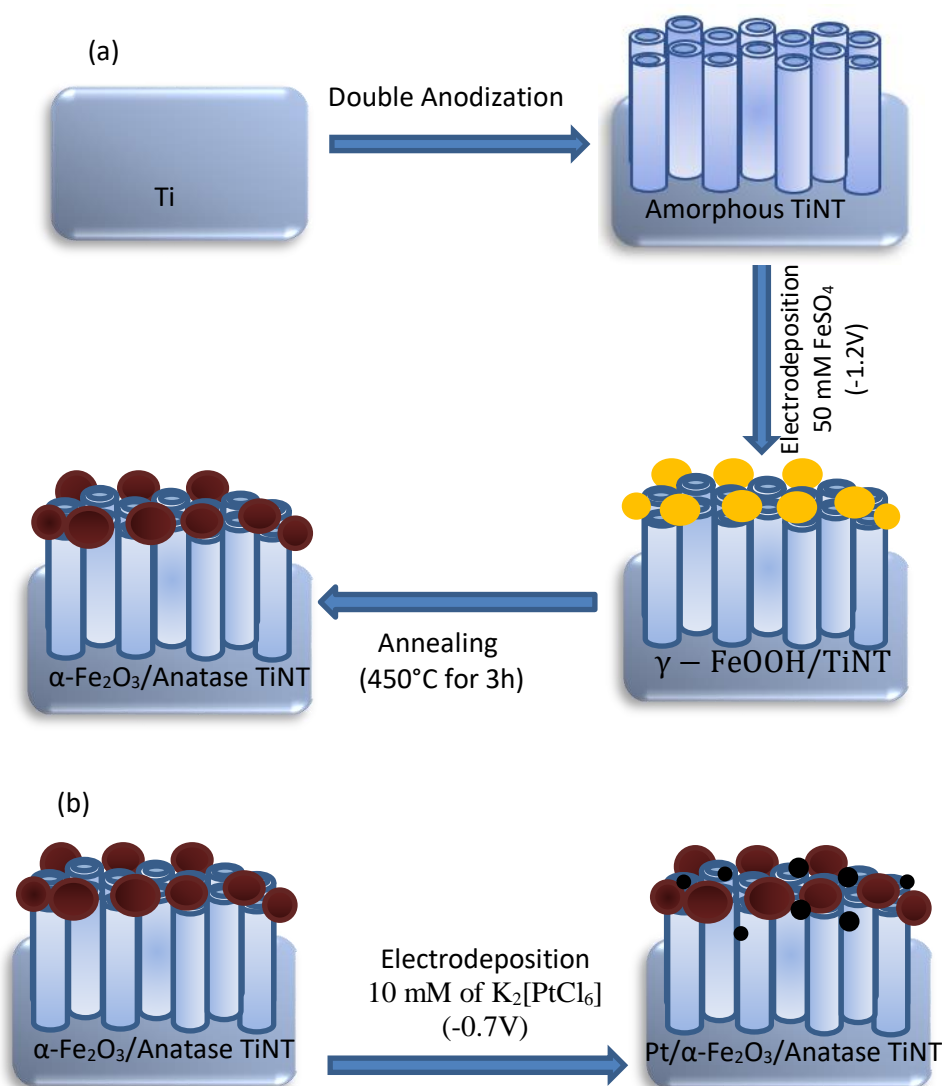
was adequately annealed, allowing the formation of anatase phase and the oxidation of γ -FeOOH nanoparticles into α -Fe₂O₃ particles.

The obtained samples were referred as: α -Fe₂O₃(25s)/TiNT, α -Fe₂O₃(50s)/TiNT and α -Fe₂O₃(100s)/TiNT.

V.1.2 Synthesis of Pt/TiNT and Pt/ α -Fe₂O₃/TiNT composites

Pt nanoparticles were electrodeposited onto TiNT and on the prepared α -Fe₂O₃(100s)/TiNT electrodes in the same three-cell configuration at a constant potential of -0.7 V in an electrolyte containing 10 mM of K₂[PtCl₆] for different durations: 25, 50 and 100s (Scheme V.1 (b)).

The obtained TiNT samples decorated with Pt were designated: Pt(25s)/TiNT, Pt(50s)/TiNT and Pt(100s)/TiNT.



Scheme V.1. Preparation procedure of α -Fe₂O₃/TiNT and Pt/ α -Fe₂O₃/TiNT systems.

V.2 Cyclic voltammetry and current-time transient analysis

Prior to electrodeposition, cyclic voltammetry measurements are required to recognize the oxidation and reduction processes occurring in the electrodeposition bath and to locate the suitable potentials for FeOOH and Pt depositions.

Figure V.1 (a) shows CV curve of TiNT substrate in the electrodeposition solution containing 0.05 M FeSO₄ solution and distilled water at a scan rate of 20 mV/s.

As can be seen from the voltammogram, starting from the open potential and sweeping towards the cathodic direction, the reduction current started to be perceptible at -0.7 V. Bivalent iron reduction starts at -0.8 V and a clear reduction peak at around -0.9 V was attained. A sharp increase in reduction current started at around -1 V. In the reverse potential scan, a well-defined anodic peak at -0.2 V is clearly visible, which is associated to the oxidative dissolution of the deposited material.

The formation of amorphous ferric oxyhydroxide (FeOOH) from aerated aqueous FeSO₄ solution can be described as an electrochemical reaction involving the starting precursor Fe²⁺ ions, which are oxidized to Fe³⁺ ions followed by precipitation of Fe³⁺ ions as amorphous γ -FeOOH on top of TiNT. The overall reaction mechanism can be represented by:

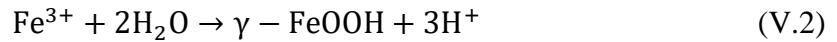


Figure V.1 (b) shows CV curve of α -Fe₂O₃/TiNT substrate in the electrodeposition solution containing 10 mM of K₂[PtCl₆] and distilled water at a scan rate of 20 mV/s. The potential scan starts from the open potential to more negative potentials. The cathodic current peak at -0.32V correspond to the reduction reaction from Pt⁴⁺ to Pt (Pt⁴⁺ + 4e⁻ → Pt). This peak is followed by an increase in the current due to the hydrogen evolution. In the reverse potential scan, an anodic peak at -0.29 V is noticeable, which is associated to the oxidative dissolution of the deposited Pt

CV curve of α -Fe₂O₃/TiNT substrate (**Figure V.1 (c)**) in 10 mM of K₂[PtCl₆] based electrolyte shows more negative reduction and oxidation current peaks. The reduction of Pt⁴⁺ began at around -0.4V and the oxidation at -0.44V.

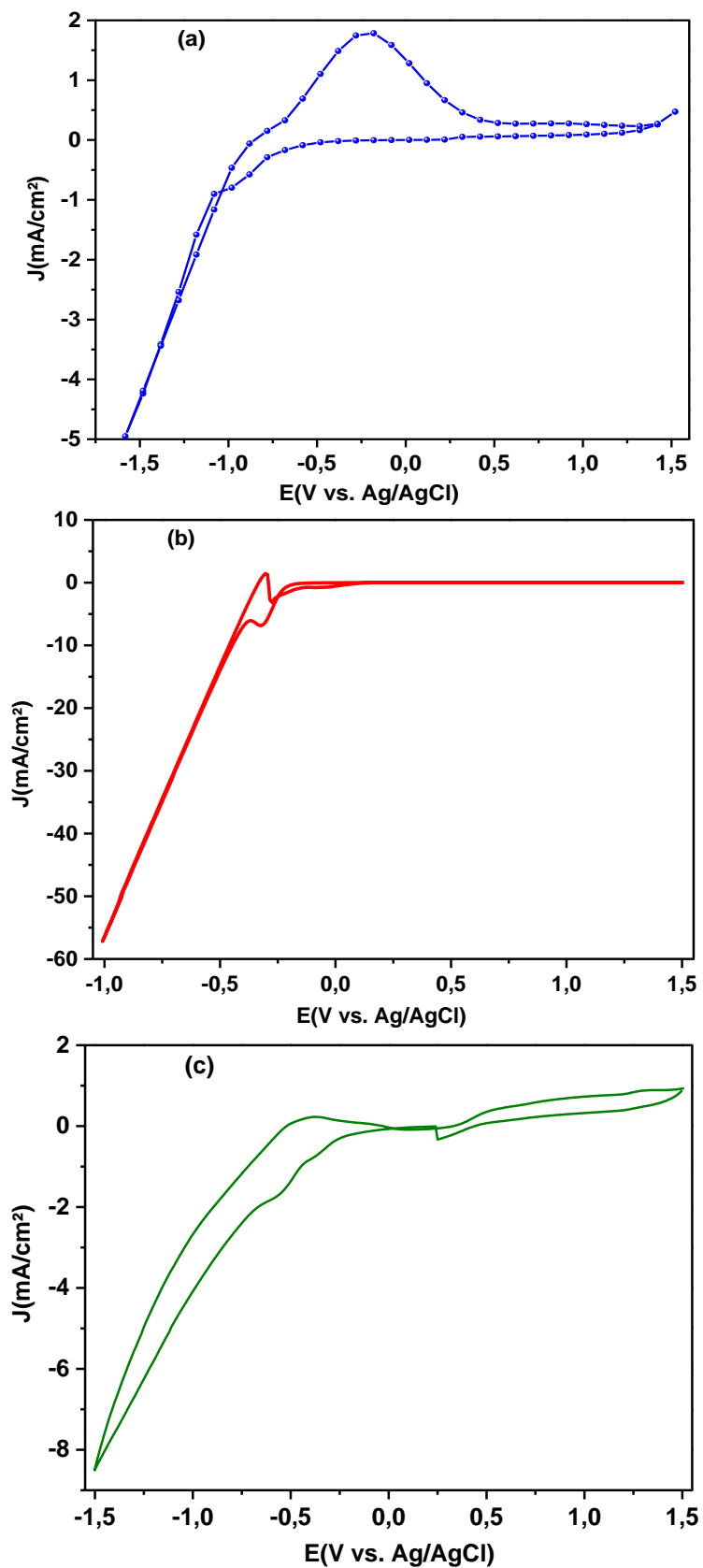


Figure V.1: Cyclic voltammograms of: (a) TiNT electrode in a solution containing 0.05 M FeSO₄ and (b) α -Fe₂O₃/TiNT electrode in a solution containing 10 mM of K₂[PtCl₆].

Based on the cathodic peak potentials of the cyclic voltammograms, the electrodeposition potentials for the formation of FeOOH on TiNT, Pt on TiNT and Pt on α -Fe₂O₃ were fixed. **Figure V.2** demonstrates the associated current-time transients for the electrodeposition of FeOOH on TiNT (**Figure V.2 (a)**) at different durations (25, 50 and 100s), Pt on TiNT (**Figure V.2 (b)**) during 25, 50 and 100s and Pt on α -Fe₂O₃/TiNT during 50s (**Figure V.2 (c)**). As can be seen, the current-time transients behave similarly, the current densities show fast rising during the early stage of the deposition process then reach a maximum for the nucleation and growth of the materials.

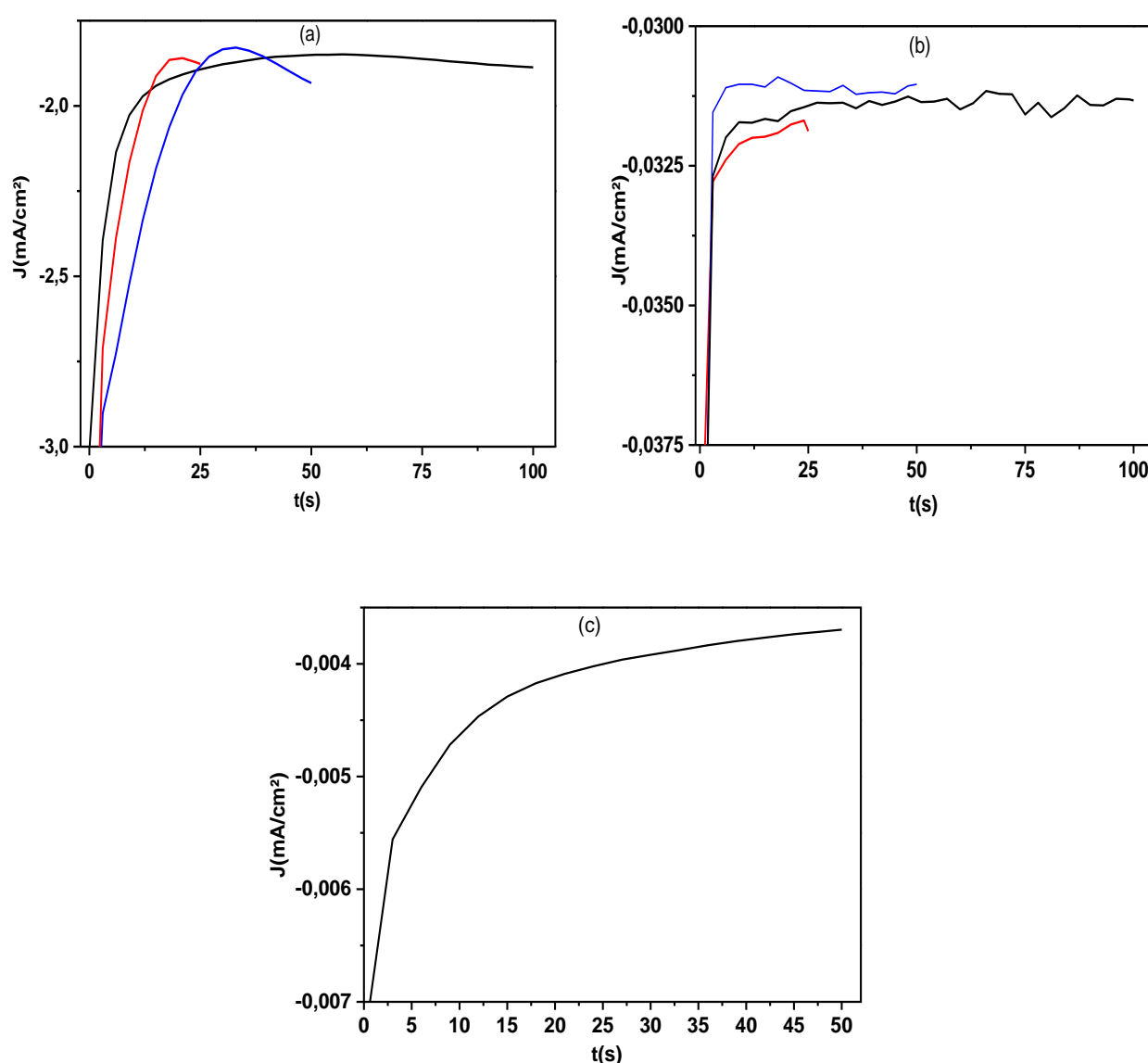


Figure V.2: Current densities recorded at different deposition times during potentiostatic electrodeposition of: (a) FeOOH on TiNT, (b) Pt on TiNT and (c) Pt on α -Fe₂O₃.

V.3 Morphological and structural characterizations of the systems

SEM micrographs in [figure V.3 \(a-c\)](#) show the top surface morphologies of the hematite particles deposited on the synthesized TiNT at different deposition durations: 25s, 50s and 100s. SEM images reveal nearly the same surface morphologies. Spherical and monodispersed particles were deposited on the TiNT surface. Various sizes of α -Fe₂O₃ particles are formed, the diameter and distribution density of these particles increased with increasing the electrodeposition duration. The particle size of α -Fe₂O₃(25s) varies between 30 and 40 nm. The average particle size is about 240 nm for α -Fe₂O₃(50s) and it ranges between 300 and 500 nm for α -Fe₂O₃(100s). Surface elemental compositions of α -Fe₂O₃(100s)/TiNT ([Figure V.3 \(d\)](#)) is carried out by using the energy dispersive X-ray spectroscopy (EDS) analysis. Characteristic peaks of Ti at 4.5 keV and 4.9 keV as well as O at 0.5 keV proves the presence of TiO₂ nanotubular layers. The peaks associated with Fe at 6.5 and 7.1 eV are clearly observed in the spectra. The atomic percentage of O in α -Fe₂O₃(100s)/TiNT is 53.52%, it is 37.55% for Ti and 8.93% for Fe. The EDS analysis of α -Fe₂O₃(50s)/TiNT (not presented here) reveals that the atomic percentage of Fe is highly reduced, it attained 0.56% only.

SEM micrographs of platinum deposited on TiNT during different times are shown in [figure V.3 \(e-g\)](#). As can be seen, the images reveal that well dispersed and quite uniform spherical Pt particles are formed. Pt particle size varies with deposition time. Particles diameters lower than 50 nm were found when the deposition time is 25s. By using 50s of electrodeposition, the TiNT surface is covered with Pt nanoparticles which exhibit a nanosized range of 50-90 nm. Larger Pt diameter spheres were obtained when increasing the deposition time. Diameters laying between 100 and 700 nm were measured by using 100s of electrodeposition.

However, after electrodeposition of Pt nanoparticles on α -Fe₂O₃/TiNT surface ([Figure V.3 \(h\)](#)), numerous spherical particles of both components (Pt) and α -Fe₂O₃ are visualized on the surface of TiNT. The film appeared denser and uniform with Pt nanoparticles as bright spots. Compared with EDS pattern of α -Fe₂O₃/TiNT, EDS of (Pt(50s)/ α -Fe₂O₃(100s)/TiNT) composite shows both Fe and Pt peaks suggesting that both elements are present in the sample ([Figure V.3 \(e\)](#)), confirming that Pt nanoparticles were successfully electrodeposited onto α -Fe₂O₃/TiNT electrode. The atomic percentage of O in Pt(50s)/ α -Fe₂O₃(100s)/TiNT is 51.42%, it is 47.85% for Ti, 0.67% for Fe and 0.06% for Pt.

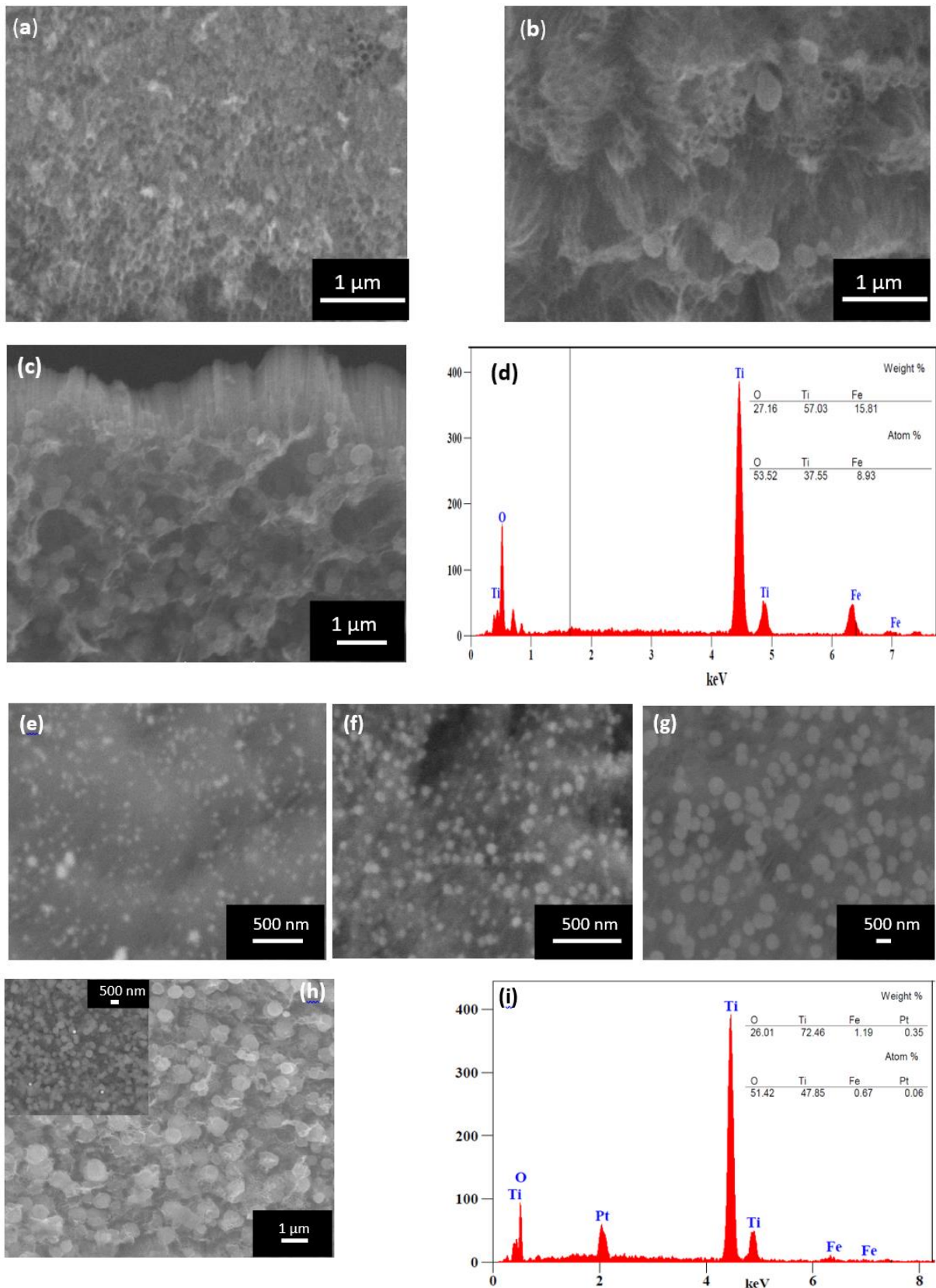


Figure V.3: SEM images of $\alpha\text{-Fe}_2\text{O}_3/\text{TiNT}$, Pt/TiNT and Pt/ $\alpha\text{-Fe}_2\text{O}_3/\text{TiNT}$ systems and corresponding EDS spectra.

X-ray diffraction measurements were achieved to characterize the crystal structure of the prepared samples. **Figure V.4 (a)** illustrates the XRD patterns of TiNT, $\alpha\text{-Fe}_2\text{O}_3(100\text{s})/\text{TiNT}$, Pt(50s)/TiNT and Pt(50s)/ $\alpha\text{-Fe}_2\text{O}_3(100\text{s})/\text{TiNT}$. Diffraction peaks of TiNT are ascribed to tetragonal TiO_2 anatase phase. In addition to the markedly strong diffraction peaks associated with Ti and TiNT, XRD pattern of $\alpha\text{-Fe}_2\text{O}_3/\text{TiNT}$ shows a small peak at $2\theta \sim 33.33^\circ$ corresponding to (104) diffraction plane of hematite, in agreement with the standard powder diffraction pattern of bulk $\alpha\text{-Fe}_2\text{O}_3$ (JPCDS No. 33-0664, $a = 5.036 \text{ \AA}$, $c = 13.749 \text{ \AA}$). The enlarged results of the XRD data obtained around this peak is shown in **figure V.4 (b)**.

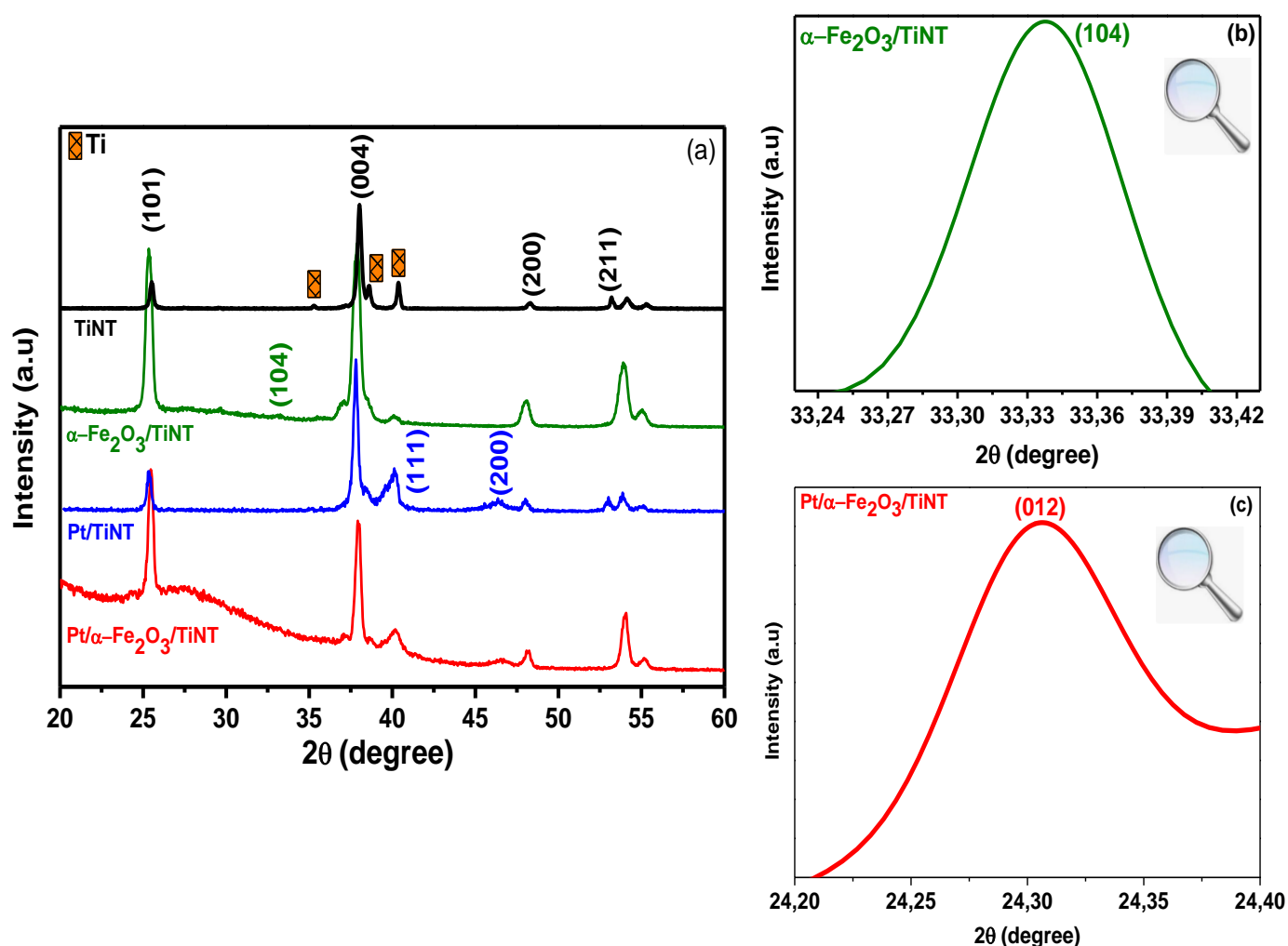


Figure V.4: (a) X-ray diffraction patterns of the films, (b) and (c) magnified views of the (104) and (012) diffraction peaks of $\alpha\text{-Fe}_2\text{O}_3$.

XRD pattern of Pt/TiNT displays diffraction peaks at nearly 40° and 46° , which can be indexed to the (111) and (200) reflections of face centered cubic crystal lattice of platinum, according to Pt (JCPDS No.04-0802). At $2\theta = 40^\circ$, Pt peak overlap with the Ti peak, resulting in peak

broadening. Peak broadening could be also related to the nanometer particle size of Pt(50s). From (200) diffraction peak of Pt, the average particle size according to the Debye–Scherrer formula was found to be about 15 nm.

When Pt was loaded on α -Fe₂O₃/TiNT film, no significant change was observed in the positions of Ti and TiO₂ peaks. The presence of α -Fe₂O₃ is indicated by diffraction peak appearing at 2θ value of 24.3°. The enlarged results around this peak (between 24.20 and 24.40) is shown in [figure V.4 \(c\)](#), it is assigned to the (012) plane. The observed peak at 33.33° is totally depleted, which may be caused by Pt deposition. Pt peaks are clearly shown at nearly 40° and 46° and are assigned to the (111) and (200) planes.

V.4 Optical characterization of the systems

The examination of absorption properties of α -Fe₂O₃/TiNT, Pt/TiNT and Pt/ α -Fe₂O₃/TiNT samples is very crucial for their potential applications. The optical properties of the samples were explored by the UV-vis diffuse reflectance spectroscopy. [Figure V.5 \(a\)](#) displays UV-visible spectra of TiNT and α -Fe₂O₃/TiNT films. As can be seen, all films display comparable absorption features. TiNT spectrum shows an absorption edge at ~ 400 nm. Whereas, those of α -Fe₂O₃/TiNT films shift towards higher wavelengths, indicating that α -Fe₂O₃ films absorb principally in the visible region of the solar spectrum. Note also that the absorption is improved with increasing the electrodeposition time. α -Fe₂O₃(100s)/TiNT have somewhat extended absorption in the region from 400 to 600 nm, which may be due to the higher distribution density of particles and greater particle size.

Optical band gaps of the systems were estimated from Tauc plots ([Figure V. 5 \(b\)](#)). The bandgap energy of TiNT is estimated to be 3.1 eV. Coupling TiNT with α -Fe₂O₃ causes a band gap reduction of α -Fe₂O₃/TiNT system. Estimated gap energy values are 3.03, 2.9 and 2.53 eV for α -Fe₂O₃(25s)/TiNT, α -Fe₂O₃(50s)/TiNT and α -Fe₂O₃(100s)/TiNT respectively. So for the extended deposition process, the band gap of TiNT can be narrowed down about 0.57 eV. The resulting band gap values are in good agreement with other reported values for Fe₂O₃ [[21](#), [22](#)]. The narrower band gap could be used for the visible light harvesting, which in turn will be very beneficial for enhancing PEC performances as we will see later. Consequently, in this series, 100s of deposition time was designated as optimum deposition condition.

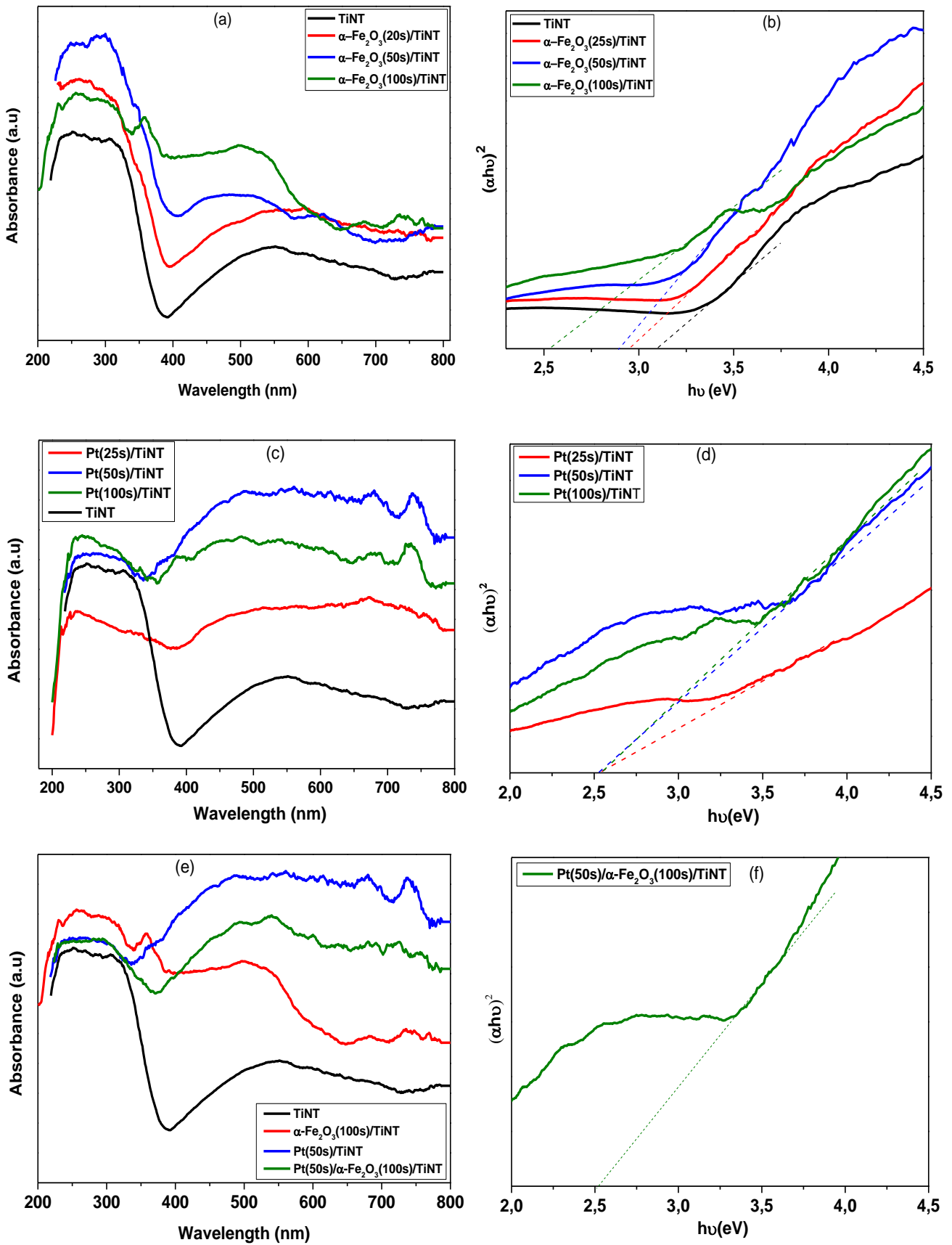


Figure V.5: UV-visible absorption spectra of the different materials and corresponding Tauc plots.

Pt-modified TiNT apparently display a pronounced optical absorption over the whole visible spectrum (Figure V.5 (c)). The optical absorption of Pt/TiNT is enhanced considerably at wavelengths between 400 and 800 comparatively to that of TiNT. The increase in the absorption intensity in the visible region with addition of platinum can possibly be related to the localized surface plasmon resonance (LSPR) of Pt nanoparticles. In Pt/TiNT system, the Pt nanoparticles are of different sizes. Therefore, the LSPR response of each Pt nanoparticle results in a high absorption over the entire wavelength range. Moreover, the nanoparticles are close enough to allow and induce significant plasmonic coupling between neighboring Pt nanoparticles, thereby enhancing optical absorption. So, because of the interparticle distances, the LSPR remains broad for all Pt/TiNT systems and masks the different hybridized modes within the total resonance. These results corroborate the theoretical investigation by Manchon et al. [11], predicting that for low interparticle distances, plasmonic coupling results in dramatic redshift, enhancement and broadening of LSP peak.

It is interesting to mention that the strongest visible light absorption is observed with Pt(50s)/TiNT. Indeed, the absorption of visible light by Pt nanoparticles is a function of the particle size. Smaller Pt nanoparticles (smaller than 70 nm) resonate well with UV irradiation [10], the peaks blue shifted to lower wavelengths. Two absorption peaks centered at about 216 and 264 nm were already found [23]. Higher Pt particle size (more than 500 nm) increases the light scattering, thus reducing the photon absorption.

Therefore, in this series, the optimal Pt nanoparticle size resulting in a stronger visible light absorption is within 50-90 nm.

Regarding the optical band gaps, Tauc plots as in figure V.5 (d) were obtained. Comparatively to the TiNT band gap, one may notice that there is a reliable band gap reduction with platinum loading. A constant band gap value of about 2.5 eV was found for all Pt/TiNT systems whatever the electrodeposition duration. The obtained band gap value is consistent with other reported values for Pt/TiO₂ systems [24, 25]. The band gap reduction of Pt/TiNT systems may be explained by the incorporation of Pt into the lattice of TiNT, generating new energy levels in the band gap of TiO₂.

Figure V.5 (e) compares the highest optical absorption spectra of the two series (α -Fe₂O₃(100s)/TiNT and Pt(50s)/TiNT) with those of TiNT and Pt(50s)/Fe₂O₃(100s)/TiNT. The results show that co-modification of TiNT by α -Fe₂O₃(100s) and Pt(50s) does not necessarily lead to a clear improvement of the optical absorption intensity. This intensity is facing below

that of Pt(50s)/TiNT. A constant band gap value of about 2.5 eV was also obtained for the ternary composite (Figure V.5 (f)).

V.5 Electronic characterization of the composites

In figure V.6 (a-g) are reported the M-S plots of the different electrodes at a frequency of 1 kHz. Since the M-S plots are difficult to discern in the same figure, the curves are plotted separately. As can be seen, all the samples exhibit positive slopes, indicating that TiNT, α -Fe₂O₃/TiNT, Pt/TiNT and Pt/ α -Fe₂O₃/TiNT samples are n-type semiconductors with electrons as the main carriers. From the M-S plots, two slopes are shown, related to the presence of both shallow and deep level donor species. The smaller slope reflects the higher electron donor density. The donor densities of the samples (N_D) at shallow levels are determined from the slopes of the first linear sections. The estimated values of N_D and U_{fb} are tabulated in Table V.1.

Donor density of $1.6 \times 10^{18} \text{ cm}^{-3}$ was found for TiNT, in agreement with our previously reported data [26, 27], which is increased up to $2.62 \times 10^{18} \text{ cm}^{-3}$ for α -Fe₂O₃(25s)/TiNT and attained 3.86×10^{18} for α -Fe₂O₃(100s)/TiNT. So, effect of α -Fe₂O₃ on N_D values is evidenced. Ti⁴⁺ titanium interstitials and oxygen vacancies are considered as a donor-type impurities and contribute to an excess of electrons in TiO₂. With α -Fe₂O₃ doping, donor density increased may be due to the substitution of Ti⁴⁺ by Fe³⁺ in the TiO₂ lattice. The flat band potential of all α -Fe₂O₃/TiNT electrodes shifted to a more negative potential compared to unmodified TiNT. The negative shift is indicative of a higher accumulation of electrons on the surface of TiNT.

Concerning Pt/TiNT electrodes, figure V.6 (e-g) demonstrates smaller slopes. The presence of Pt induced an increase in the carrier density of TiNT. Donor densities greater than $6 \times 10^{18} \text{ cm}^{-3}$ were found for Pt(50s)/TiNT and Pt(100s)/TiNT. These findings yield direct evidence that Pt acts as an electron donor and that the donor density increased with Pt loading. So, the electrical conductivity is improved. The values of U_{FB} of Pt/TiNT are more positive compared to unmodified TiNT. The positive shift in U_{FB} was already reported for Pt doped films [28, 29]. This positive shift, according to [29] indicates that the conduction band edge position in Pt-TiO₂ is slightly lowered. The increase of the U_{FB} promotes an increase in band-bending which can contribute to the charge separation process [30].

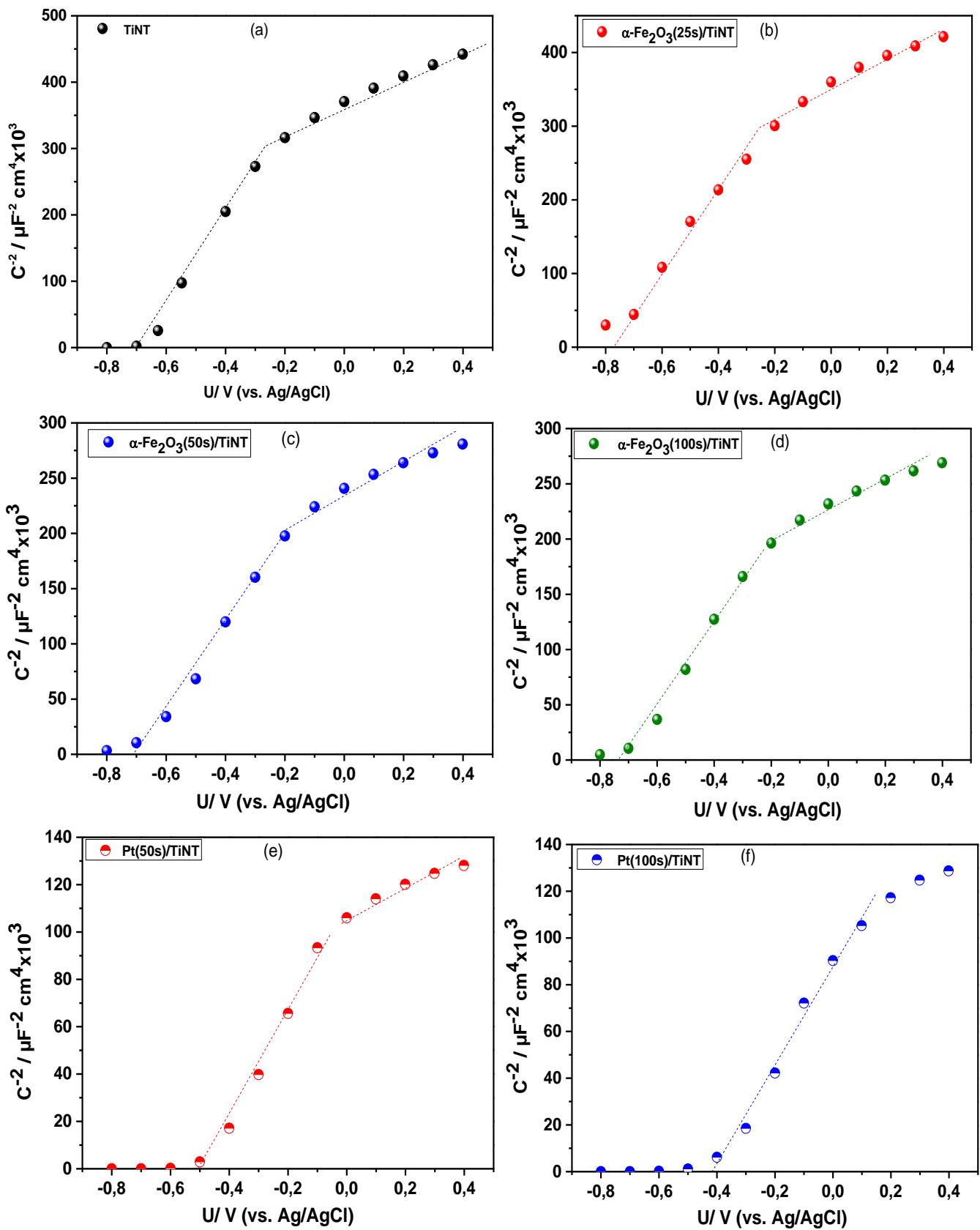


Figure V.6: M-S plots of the different electrodes.

Electrodes	slopes	N_D (cm^{-3})	U_{FB}
TiNT	8.81×10^{11}	1.6×10^{18}	-0.7
$\alpha\text{-Fe}_2\text{O}_3(25\text{s})/\text{TiNT}$	5.382×10^{11}	2.62×10^{18}	-0.75
$\alpha\text{-Fe}_2\text{O}_3(50\text{s})/\text{TiNT}$	3.78×10^{11}	3.73×10^{18}	-0.77
$\alpha\text{-Fe}_2\text{O}_3(100\text{s})/\text{TiNT}$	3.65×10^{11}	3.86×10^{18}	-0.8
Pt (50s)/TiNT	2.29×10^{11}	6.15×10^{18}	-0.5
Pt(100s)/TiNT	2.21×10^{11}	6.4×10^{18}	-0.41
Pt(50s)/ $\alpha\text{-Fe}_2\text{O}_3(100\text{s})/\text{TiNT}$	2.72×10^{11}	5.18×10^{18}	-0.68

Table V.1: carrier densities and flatband potentials evaluated from linear sections of the M-S plots of figure V.6.

V.6 Photoelectrochemical measurements

To identify the role of Pt and $\alpha\text{-Fe}_2\text{O}_3$ in charge transport process, EIS characterization under visible light illumination was carried out. **Figure V.7 (a and b)** shows the Nyquist plots of the different electrodes. As can be seen, Nyquist plots of $\alpha\text{-Fe}_2\text{O}_3/\text{TiNT}$ electrodes (**Figure V. 7 (a)**) provide a semicircle representation. The semicircle diameter in the Nyquist plot at high frequency is representative of the charge transfer resistance (R_{ct}). A wider diameter signifies a slower charge transfer process. In the present series of experiments, the TiNT electrode has the widest semicircle arc, corresponding to the highest charge transfer resistance and therefore poor conductivity under visible light. After $\alpha\text{-Fe}_2\text{O}_3$ was loaded, the arc radius reduces. This can suggest the enhancement of the interfacial charge transfer of TiNT by $\alpha\text{-Fe}_2\text{O}_3$. An equivalent-circuit model, a simplified Randles circuit ($R_s(R_{ct}C_{dl})$), is applied to represent an electrode/electrolyte interface, in which R_s represents the solution resistance in series with a parallel circuit of the charge transfer resistance R_{ct} and the double-layer capacitance C_{dl} , whose behavior is modelled by a CPE to account for the non-ideal behavior of the surface. **Table V.2** gives the calculated values of the electrical circuit parameters. The $\alpha\text{-Fe}_2\text{O}_3(100\text{s})/\text{TiNT}$ electrode exhibited the smallest R_{ct} among all the samples of this series, indicating its lowest charge transfer resistance. Accordingly, these resistances decreased in the order of $\alpha\text{-Fe}_2\text{O}_3(100\text{s})/\text{TiNT} < \alpha\text{-Fe}_2\text{O}_3(50\text{s})/\text{TiNT} < \alpha\text{-Fe}_2\text{O}_3(25\text{s})/\text{TiNT} < \text{TiNT}$.

Figure V.7 (b) shows Nyquist plots of Pt/TiNT and Pt(50s)/ α -Fe₂O₃(100s)/TiNT electrodes. Through forming the heterojunction with Pt, the charge transfer rate is improved. The smallest high frequency diameter in Pt/TiNT systems is observed on Pt(100s)/TiNT. Comparatively to all investigated systems, Pt(50s)/ α -Fe₂O₃(100s)/TiNT composite (Figure V.7 (c)) exhibits the smallest high frequency diameter, indicating that on this ternary composite, the electron transfer is much faster than that on all other electrodes. An equivalent-circuit model consisting of two (RCPE) units each containing a resistance in parallel with a CPE is applied to compare charge transfer resistances of Pt/TiNT and Pt/ α -Fe₂O₃/TiNT electrodes. In accordance with the objectives of the present work, values of the electrical circuit parameters relative to the high frequency region only are inserted in Table V.3.

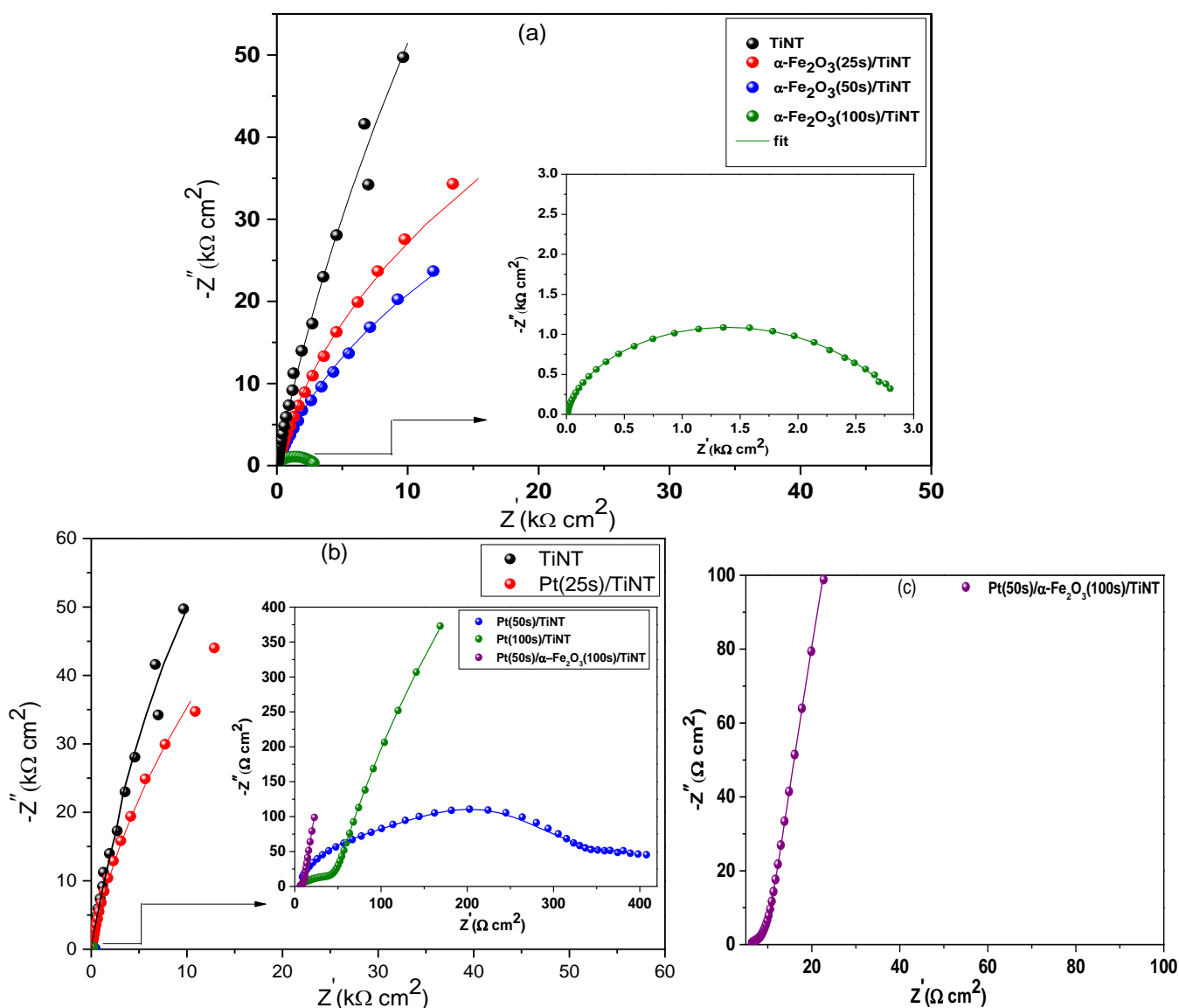


Figure V.7: Nyquist diagrams under visible light illumination of the different photoelectrodes at 0.2V vs. Ag/AgCl.

Electrode	R_s ($\Omega \text{ cm}^2$)	R_{ct} ($\text{k}\Omega \text{ cm}^2$)	$Q_{dl} \times 10^6$ ($\text{s}^n \Omega^{-1} \text{ cm}^{-2}$)	n_{dl}
TiNT	5.4	190.4	4.26	0.92
$\alpha\text{-Fe}_2\text{O}_3(25\text{s})/\text{TiNT}$	3.81	149.1	4.65	0.89
$\alpha\text{-Fe}_2\text{O}_3(50\text{s})/\text{TiNT}$	1.94	109.2	5.82	0.85
$\alpha\text{-Fe}_2\text{O}_3(100\text{s})/\text{TiNT}$	4.91	3.0	5.51	0.89

Table V.2: Circuit element parameters determined by fitting of the EIS spectra for $\alpha\text{-Fe}_2\text{O}_3/\text{TiNT}$ electrodes.

Electrode	R_s (Ωcm^2)	R_{ct} (Ωcm^2)	$Q_{dl} \times 10^5$ ($\text{s}^n \Omega^{-1} \text{ cm}^{-2}$)	n_{dl}
Pt(25s)/TiNT	3.84	1000.1	4.26	0.7
Pt(50s)/TiNT	3.91	300	11.2	0.86
Pt(100s)/TiNT	6	41.7	17.5	0.61
Pt(50s)/$\alpha\text{-Fe}_2\text{O}_3(100\text{s})/\text{TiNT}$	5.86	5.15	1040	0.5

Table V.3: Circuit element parameters determined by fitting of the EIS spectra for Pt/TiNT and Pt/ $\alpha\text{-Fe}_2\text{O}_3/\text{TiNT}$ electrodes.

R_{ct} reaches 300 Ω for Pt(50s)/TiNT electrode. It is about 42 Ω for Pt(100s)/TiNT electrode and only about 5.15 Ω for Pt(50s)/ $\alpha\text{-Fe}_2\text{O}_3(100\text{s})/\text{TiNT}$ composite. This tremendous lowering of a charge-transfer resistance in Pt(50s)/ $\alpha\text{-Fe}_2\text{O}_3(100\text{s})/\text{TiNT}$ composite is may be due to the synergetic effects of $\alpha\text{-Fe}_2\text{O}_3(100\text{s})$ and Pt which accelerate the charge transfer. This will be favorable to the transport and separation of photogenerated carriers in photocatalytic applications.

PEC properties were further examined by means of the linear sweep voltammetry (LSV) technique in 1M KOH solution under visible light. **Figure V.8 (a)** shows the photocurrent densities of TiNT and $\alpha\text{-Fe}_2\text{O}_3/\text{TiNT}$ photoanodes. Photocurrent indicates the rate of water splitting and the amount of charge carriers produced by the incident light and their participation in the hydrogen ion reduction and water oxidation reactions.

It is clearly observed that the photocurrents of $\alpha\text{-Fe}_2\text{O}_3/\text{TiNT}$ samples are higher than that of TiNT and increased as the electrodeposition time was extended. A significant enhancement of the photoresponses of $\alpha\text{-Fe}_2\text{O}_3/\text{TiNT}$ electrodes comparatively to that of TiNT indicates the reduced photogenerated pair recombination and the more efficiency of the carrier transport in

the α -Fe₂O₃/TiNT heterojunctions. In fact, due to the different work functions of α -Fe₂O₃ (5.88 eV) and TiO₂ (4.308 eV), the contact between TiO₂ and α -Fe₂O₃ leads to the equalization of their Fermi levels. Because the CB of TiO₂ is below the CB of α -Fe₂O₃, so under visible light irradiation, α -Fe₂O₃ is activated and excited electrons from α -Fe₂O₃ can overcome the barrier and migrate to the CB band of TiO₂. Whereas holes move from the VB of TiO₂ to that of α -Fe₂O₃ and thus effectively reduce the photogenerated pair recombination.

α -Fe₂O₃(100s) /TiNT photoanode shows a significantly enhanced photocurrent and presents much better PEC performance compared to the others. α -Fe₂O₃(100s)/TiNT photoanode reached photocurrent densities of 92 μ A/cm² and 1 mA/cm² at water oxidation potential (0.23 V/Ag/AgCl) and at 1 V/Ag/AgCl respectively. TiNT, α -Fe₂O₃(25s)/TiNT and α -Fe₂O₃(50s)/TiNT systems display photocurrent values of 20, 26 and 50 μ A/cm² respectively at water oxidation potential and values of 19, 138 and 425 μ A/cm² respectively at 1 V/Ag/AgCl. One can notice that these photocurrent results follow the trend of optical absorption, suggesting that its contribution is the determining aspect to boost photocurrent performance on α -Fe₂O₃/TiNT photoanodes. Compared to that of pristine TiNT photoanode, the photocurrent density at 1.23 V vs. RHE increased by more than 4 times. The significant photocurrent density of α -Fe₂O₃(100s)/TiNT is closely connected to the size and density of hematite particles on the surface of TiNT, which efficiently absorb visible light owing to their narrow band gap (2.5 eV) and efficient charges transport.

Figure V.8 (b) shows the photocurrent response of the prepared Pt/TiNT photoelectrodes. As can be seen, as the bias potential increases anodically, the photocurrent shows a significant increase. Pt(50s)/TiNT photoelectrode displayed a substantially superior photocurrent density at water oxidation potential. Compared to that of pristine TiNT photoanode, the photocurrent density at 1.23 V vs. RHE increased by more than 100 times and reached a notable photocurrent density value of 2.3 mA/cm², representing a higher activity for water oxidation. It also showed a cathodic shift in the onset potential. Lower photocurrent densities of 0.9 and 0.26 mA/cm² were attained by Pt(100s)/TiNT and Pt(25s)/TiNT. The trend of the photocurrent is similar to the result of the optical absorption. So better PEC performance of the Pt/TiNT samples comparatively to TiNT and α -Fe₂O₃/TiNT photoelectrodes may be associated with their better optical absorption.

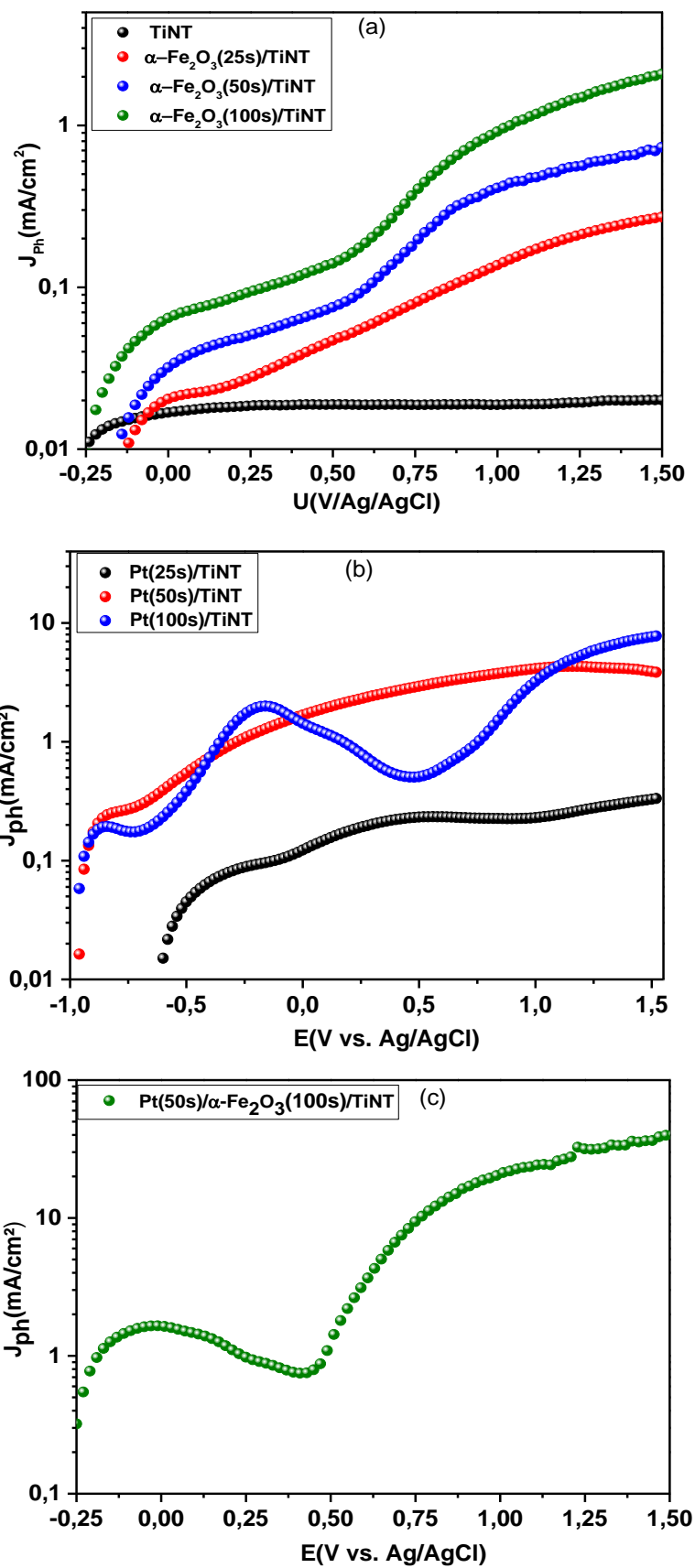


Figure V.8: LSVs of the photoelectrodes under visible light illumination.

The photocurrent improvement can be explained by the conjugated effects of LSPR and Schottky junction. In fact, Pt nanoparticles and TiNT are very close to each other and are simultaneously excited. Plasmonic Pt nanoparticles improve the light absorption, LSP created on a Pt nanoparticle generates a population of activated electrons that resonate with the incoming field. The work function of Pt (6.35 eV) is higher than that of TiO₂ (4.308 eV), so the energetic hot electrons can transfer across the Schottky barrier created through the contact of Pt with TiNT, thus extending the lifetime of the charge carriers and improving their separation. This considerably contributes to the reduction of electron and hole recombination rates. The electrons react with water to form H₂.

The Pt(50s)-doped α -Fe₂O₃(100s)/TiNT system (**Figure V.8 (c)**) displays at least two times improved photocurrent over the entire potential window. According to Shankar et al. [31], when the electron–hole separation process is superior, a property manifest in the slope of the potential–current plot. Much higher photocurrents at higher potentials are noticed, photocurrent density reaches an impressive value of 21 mA/cm² at 1 V vs Ag/AgCl. For comparison, **Table V.4** below shows the photocurrent values obtained in this work and those reported in the literature.

Photoelectrode	Method	Photocurrent density	electrolyte	Ref
Pt/TiO ₂ nanorods	Hydrothermal deposition	0.67 mA/cm ² at 1.23VRHE	0.1 M NaOH	[32]
α -Fe ₂ O ₃ /Pt	Deposition	0.78 mA cm ⁻² at 1.5 V vs. Ag/AgCl	/	[33]
Pt/ α -Fe ₂ O ₃	Coelectrodeposition	1.43 mA/cm ² at 0.4 V vs Ag/AgCl	1 M NaOH	[34]
Pt/ α -Fe ₂ O ₃	Anodization and photodeposition	220 μ A/cm ² at +0.4 V vs Ag/AgCl	0.1 M Na ₂ S + 0.1 M Na ₂ SO ₃	[35]
Pt/ α -Fe ₂ O ₃	Electrodeposition	0.56 mA/cm ² at 0.4 V versus Ag/AgCl	1 M NaOH	[28]
Pt@TiO ₂ nanotubes	Photodeposition	24.2 mA/cm ² at 0.9 VSCE	0.5 M KOH	[36]
Pt/ α -Fe ₂ O ₃	Magnetron sputtering	0.34 mA/cm ² at 1.23V RHE	1 M NaOH	[37]
Pt/TiNT	Electrodeposition	2.3 mA/cm ² at 1.23V RHE	1M KOH	This work
Pt/ α -Fe ₂ O ₃ /TiNT	Two-step electrodeposition	21 mA/cm ² at 1 V vs Ag/AgCl	1M KOH	This work

Table V.4: Photocurrent values of photoanodes in PEC water splitting from this and other works.

The total percent photoconversion efficiency of light energy under light illumination to chemical energy in the presence of an external applied potential (E_{app}) was calculated using the following equation [3]:

$$\text{photoconversion efficiency (\%)} = [j_p [1.23 - |E_{app}|] \times 100] / I_0 \quad (\text{V.3})$$

where I_0 is the power density of incident light (mW cm^{-2}), j_p the photocurrent density at the measured potential, E_{app} is the applied potential, $E_{app} = E_{meas} - E_{aoc}$, where E_{meas} is the electrode potential (vs. Ag/AgCl) of the working electrode at which photocurrent is measured under illumination, and E_{aoc} is the electrode potential (vs. Ag/AgCl) of the same working electrode under open circuit conditions, under the same illumination, and in the same electrolyte.

Figure V.9 (a-e) shows the photoconversion efficiencies of the different photoanodes. Among them, TiNT photoanode showed the lowest optimal photoconversion efficiency of about 0.05%. An impressive maximum photoconversion efficiency of about 9.7% was achieved by Pt(50s)/ α -Fe₂O₃(100s)/TiNT. The trend of photoconversion efficiencies mirrors perfectly that of the Nyquist plots, which follows the order: Pt(50s)/ α -Fe₂O₃(100s)/TiNT > Pt(100s)/TiNT > Pt(50s)/TiNT > Pt(25s)/TiNT > α -Fe₂O₃(100s)/TiNT > α -Fe₂O₃(50s)/TiNT > α -Fe₂O₃(25s)/TiNT > TiNT.

PEC water splitting requires four steps: (i) light absorption, (ii) charge carrier generation, (iii) charge carrier separation and (iv) charge carrier transport to the interface. Despite higher optical absorption of Pt(50s)/TiNT, higher photoconversion efficiency of Pt(50s)/ α -Fe₂O₃(100s)/TiNT compared to that of Pt(50s)/TiNT may be related to the enhanced charge transfer and transportation while decreasing carrier recombination. To check the reasonability of this conclusion, **figure V.10** shows photoluminescence spectra of both Pt(50s)/TiNT and Pt(50s)/ α -Fe₂O₃(100s)/TiNT monitored with excitation of 410 nm. The decrease of the PL intensity of Pt(50s)/ α -Fe₂O₃(100s)/TiNT demonstrates significant reduction of the charge carrier recombination rate and so an enhanced charge separation of electron hole pairs.

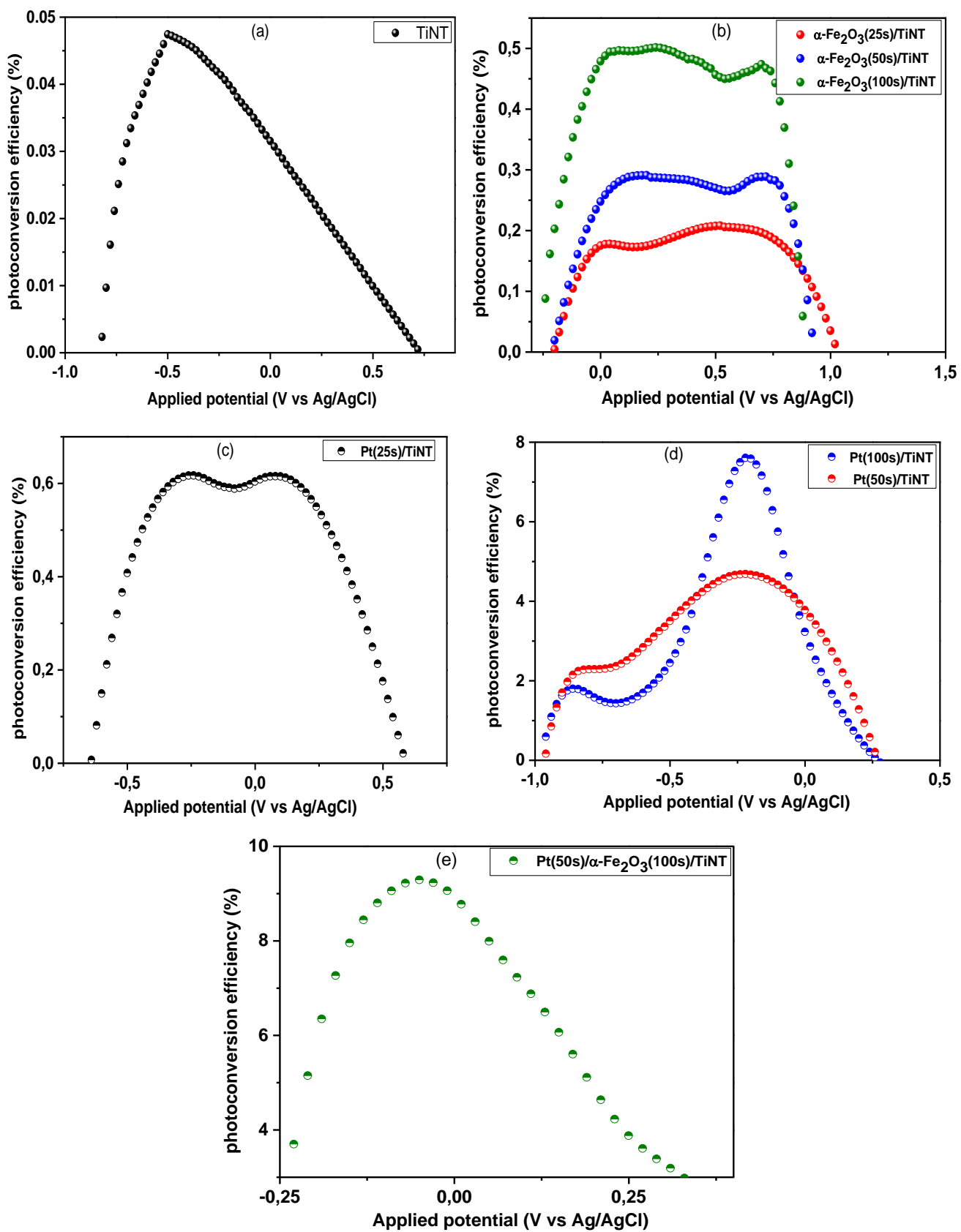


Figure V.9: Calculated photoconversion efficiencies of the photoanodes.

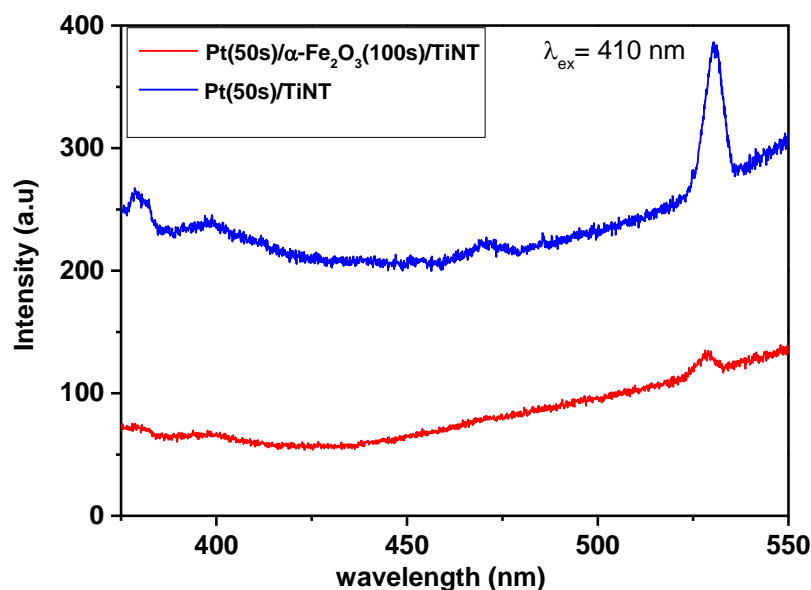


Figure V.10: Photoluminescence spectra of Pt/TiNT and Pt/ α -Fe₂O₃/TiNT photoanodes.

One of possible mechanisms for water splitting of Pt(50s)/ α -Fe₂O₃(100s)/TiNT is suggested in [figure V.11](#). Pt nanoparticles were excited under visible light irradiation. The surface electrons oscillate with a certain frequency and induce the SPR effect. Hot electrons from the SPR of Pt have enough energy to surmount the Schottky barrier formed at the Pt/ α -Fe₂O₃ interface and will then be transfer to the conduction band of α -Fe₂O₃. In addition, α -Fe₂O₃ is also activated under visible light, because the conduction CB band position of α -Fe₂O₃ is higher than that of TiO₂, so the excited electrons from the VB to the CB of α -Fe₂O₃ can overcome the Schottky barrier and migrate to the CB band of TiO₂ and holes of TiO₂ transfer to the VB of α -Fe₂O₃, resulting in more efficient separation. Under an external bias voltage, electrons can be transferred from the TiO₂ conduction band to the cathode (platinum foil) and then react with H⁺ ions to form H₂ on the platinum foil surface.

- Pt/TiNT and Pt(50s)/ α -Fe₂O₃(100s)/TiNT electrodes demonstrate very improved charge transfer rate.
- Pt(50s)/TiNT photoelectrode reached photocurrent density value of 2.3 mA/cm² at 1.23 V vs. RHE, which is more than 100 times that of pristine TiNT.
- The Pt(50s)-doped α -Fe₂O₃(100s)/TiNT system reached much higher photocurrent at higher potentials, photocurrent density reaches an impressive value of 21 mA/cm² at 1V vs Ag/AgCl, demonstrating significant reduction of the charge carrier recombination rate and so an enhanced charge separation of electron hole pairs.
- Photoconversion efficiencies follows the order: Pt(50s)/ α -Fe₂O₃(100s)/TiNT > Pt(100s)/TiNT > Pt(50s)/TiNT > Pt(25s)/TiNT > α -Fe₂O₃(100s)/TiNT > α -Fe₂O₃(50s)/TiNT > α -Fe₂O₃(25s)/TiNT > TiNT.

In summary, our work has demonstrated that loading with Pt and α -Fe₂O₃ can be used as a strategy to improve the performance of TiNT materials as photoanodes for PEC water splitting.

References

- [1] W. Bootluck, T. Chittrakarn, K. Techato, W. Khongnakorn, *Journal of Environmental Chemical Engineering*, 9(2021)105660.
- [2] L. Rekeb, L. Hamadou, A. Kadri, N. Benbrahim, *Electrochimica Acta*, 256(2017)162.
- [3] L. Rekeb, L. Hamadou, A. Kadri, N. Benbrahim, E. Chainet, *International Journal of Hydrogen Energy*, 44(2019)10541.
- [4] B. Ma, J. Kim, T. Wang, J. Li, K. Lin, W. Liu, S. Woo, *RSC Advances*, 5(2015)79815.
- [5] Z. Guanghonga, D. Hongyan, Z. Yufu, L. Yuebin, L. Peng, *Rare Metal Materials and Engineering*, 45(2016)1117.
- [6] S.Y. Moon, B.N. Jeong, Y. Park, *The Korean Journal of Chemical Engineering*, 33(2016)2325.
- [7] K. Sivula, F. le Formal, M. Grätzel, *ChemSusChem*, 4(2011)432.
- [8] R. Yin, M. Liu, R. Tang, L. Yin, *Nanoscale Research Letters*, 12(2017)520.
- [9] A.G. Joly, J.R. Williams, S.A. Chambers, G. Xiong, W.P. Hess, *Journal of Applied Physics*, 99(2006) 053521.
- [10] N. C. Bigall, T. Hartling, M. Klose, P. Simon, L. M. Eng, *Nano Letters*, 8(2008)4588.
- [11] D. Manchon, J. Lermé, T. Zhang, A. Mosset, C. Jamois, C. Bonnet, J-M. Rye, A. Belarouci, M. Broyer, M. Pellarin, E. Cottancin, *Nanoscale*, 7(2015)1181.
- [12] L. Liu, *Materials Letters*, 159 (2015)284.

- [13] H. J. Zhou, S.S. Wang, *ACS Nano*, 2(2008)944.
- [14] C. Su, H. Wang, X. Liu, *Crystal Research and Technology*, 46(2011)209.
- [15] R. S. Schrebler, L. Ballesteros, A. Burgos, E. C. Munoz, P. Grez, D. Leinen, F. Martin, J. R. Ramos-Barrado, E. A. Dalchiele, *Journal of The Electrochemical Society*, 158(2011)D500.
- [16] J. Lv, H. Gao, H. Wang, X. Lu, G. Xu, D. Wang, Z. Chen, X. Zhang, Z. Zheng, Y. Wu, *Applied Surface Science*, 351(2015)225.
- [17] A.Z. Jurek, J. Hupka, *Catalysis Today*, 230(2014)181.
- [18] H-M. Chiu, T-H. Yang, Y-C. Hsueh, T-P. Perng, J-M. Wu, *Applied Catalysis B: Environmental*, 163(2015)156.
- [19] T. Sptaru, M. Marcu, N. Sptaru, *Applied Surface Science*. 269(2013)171.
- [20] S. Boudinar, N. Benbrahim, B. Benfedda, A. Kadri, E. Chainet, L. Hamadou, *Journal of The Electrochemical Society*, 161(2014)D227.
- [21] F. Bouhjar, L. Derbali, B. Marí, B. Bessaís, *Results in Physics*, 17(2020)102996.
- [22] P. Luan, M. Xie, D. Liu, X. Fu, L. Jing, *Scientific reports*, 4(2014)6180.
- [23] E. Gharibshahi and E. Saion, *International Journal of Molecular Sciences*, 13(2012)14723.
- [24] J.F. Guayaquil-Sosa, B. Serrano-Rosales, P.J. Valadés-Pelayo, H. de Lasa, *Applied Catalysis B: Environmental* 211(2017)337.
- [25] J. Jiao, Y. Wei, K. Chi, Z. Zhao, A. Duan, J. Liu, G. Jiang, Y. Wang, X. Wang, C. Han, P. Zheng, *Photonic Energy Technol.* 5(2017)877.
- [26] S. Ait Ali Yahia, L. Hamadou, A. Kadri, N. Benbrahim, E.E.M. Sutter, *Journal of The Electrochemical Society*, 159(2012)1.
- [27] L. Ainouche, L. Hamadou, A. Kadri, N. Benbrahim, D. Bradai, *Electrochimica Acta*, 133(2014)597.
- [28] G. Rahman, O-S. Joo, *Materials Chemistry and Physics* 140 (2013)316.
- [29] S. Kim, S-J. Hwang, W. Choi, *The Journal of Physical Chemistry B* 109(2005)24260.
- [30] R. H. Gonçalves and E. R. Leite, *Energy & Environmental Science*, 7(2014)2250.
- [31] K. Shankar, G.K. Mor, H.E. Prakasam, S.Yoriya, M. Paulose, O.K.Varghese, C. A.Grimes, *Nanotechnology* 18(2007)065707.
- [32] T.S. Atabaev, M.A. Hossain, D. Lee, H.K. Kim, Y.H. Hwang, *Results in Physics* 6(2016)373.
- [33] X. Li, Z. Wang, Z. Zhang, L. Chen, J. Cheng, W. Ni, B. Wang, E. Xie, *Scientific Reports*, 5(2015)9130.
- [34] Y-S. Hu, A. Kleiman-Shwarsctein, A. J. Forman, D. Hazen, J-N. Park, E. W. McFarland, *Chemistry of Materials*, 20(2008)3803.

- [35] M. M. Momeni, Y. Ghayeb, A. Hallaj, R. Bagheri, Z. Songd, H. Farrokhpour, *Materials Letters* 237(2019)188.
- [36] Y. Lai, J. Gong, C. Lin, *International Journal of Hydrogen Energy* 37(2012)6438.
- [37] J. Lin, X. Zhang, L. Zhou, S. Li, G. Qin, *Materials Research Bulletin*, 91(2017)214.

General conclusion

The principal objective of this thesis was to synthesize a high performance TiNT based electrode through facet engineering and heterojunction engineering to improve solar energy utilization, conversion and storage. Three types of materials (graphene, Pt and hematite) were loaded on TiNT to develop heterostructures for improving their optical, electrical and electrochemical properties. Modification of TiNT aimed to enhance specific surface area, conductivity, light absorption, charge generation, separation and transport for various applications, including photocatalysis, PEC water splitting and supercapacitor for energy storage. The main conclusions are summarized in the following points:

- TiNT with high crystallinity and percentage of exposed {001} facets were synthesized using a two-step anodization processes in ethylene glycol based electrolytes. TiNT exhibiting higher ratio of exposed {001} facets, mainly consisted of shallow gap states with lower density, significantly improve photoelectrochemical water oxidation and photocatalytic efficiencies.
- Graphene was successfully electrodeposited on TiNT by electrochemical deposition from dispersed graphene. Graphene was produced by electrochemical exfoliation of pure graphite sheet and 5B pencil cores in sulfate-containing electrolytes. Graphene with high electrical conductivity, low amount of oxygen-containing functional groups and free impurities modified TiNT system was proven to be the best catalyst for achieving both higher capacitance and higher MB photocatalytic degradation. Gr/TiNT showed a long-term cycle stability, retaining ~98% specific capacitance after 1000 cycles and sustain both high energy and power densities.
- Hematite (α -Fe₂O₃) is deposited on TiNT via an electrodeposition process. The reduced band gap of α -Fe₂O₃ makes easier the photon energy absorption from sunlight and generates more photo-induced charges. The matching of the conduction bands of α -Fe₂O₃ and TiNT is favorable for the separation and transport of photoinduced charges. photocurrents of α -Fe₂O₃/TiNT samples are higher than that of TiNT and increased as the electrodeposition time was extended. Compared to that of pristine TiNT photoanode, the photocurrent density of α -Fe₂O₃(100s)/TiNT at 1.23 V vs. RHE increased by more than 4 times. The significant photocurrent density of α -

$\text{Fe}_2\text{O}_3(100\text{s})/\text{TiNT}$ is closely connected to the size and density of hematite particles on the surface of TiNT.

- Pt nanoparticles are loaded on TiNT by electrodeposition technique. Pt film consists of a collection of random connective nanoparticles and acts as a broadband visible light absorber. Pt/TiNT heterostructure leads to the absorption over the whole range of wavelengths and to the edge shifting to lower photon energy. The LSPR impact of each Pt nanoparticle sums up to raised absorption over the whole range of wavelengths.
- Pt plasmonic effects and Schottky junction between Pt and TiNT accelerate the separation of photo-induced charges. Pt nanoparticles with optimal sizes (50-90 nm) result in a stronger visible light absorption. Pt(50s)/TiNT photoelectrode displayed a noticeably larger photocurrent density at water oxidation potential. Compared to that of pristine TiNT photoanode, the photocurrent density at 1.23 V vs. RHE increased by more than 100 times and reached a notable photocurrent density value of 2.3 mA/cm², representing an excellent activity for water oxidation.
- Pt nanoparticles and $\alpha\text{-Fe}_2\text{O}_3$ particles are loaded on TiNT by two-step electrodeposition processes to form Pt(50s)/ $\alpha\text{-Fe}_2\text{O}_3(100\text{s})/\text{TiNT}$ heterostructure. Photoelectrochemical measurements have shown very strong photoresponses, exceeding by several orders of magnitude that of TiNT. Charge transfer resistance of only 5.15 Ω from Nyquist plot and an impressive maximum photoconversion efficiency of about 9.7% were achieved, demonstrating significant reduction of the charge carrier recombination rate and so an enhanced charge separation of electron hole pairs. So, optimized ternary photocatalyst improved the hydrogen generation rate. This fact could be attributed to both the strong LSPR induced effect of Pt nanoparticles and electron-hole separation at $\alpha\text{-Fe}_2\text{O}_3/\text{TiNT}$ heterojunction.

Future challenges and perspectives

Despite the good performance of modified TiNT in both energy conversion and storage applications, further work should be completed to further improve the current results. Recommendations for the future research work are listed as follows:

- Modified TiNT should be performed for photocatalytic degradation of real pollutants.
- The recyclability and durability of the photocatalysts must be addressed.

- Regarding energy storage applications, we have dealt with the supercapacitive performance of α -Fe₂O₃/TiNT heterojunction (section not included in this thesis), the obtained results are very promising. Nevertheless, it would be very interesting to combine in an asymmetric configuration both α -Fe₂O₃ as a pseudo-capacitive electrode and graphene as an EDLC to considerably improve the specific capacity and the energy and power densities.
- Use the two-electrode test for supercapacitor in order to replicates the physical configuration and charge transfer that occurs in a packaged cell.
- Numerical simulation may be conducted to further explore SPR effect of plasmonic Pt nanoparticles.
- Raman spectrum can be recorded to analyze the D and G bands of graphene and the corresponding defects.

List of schemes

Scheme III.1: A Two-step anodization to grow high-aspect-ratio TiNT.

Scheme III.2: The most probable emissions derived from photoluminescence analysis.

Scheme V.1: Preparation procedure of α -Fe₂O₃/TiNT and Pt/ α -Fe₂O₃/TiNT systems.

List of Tables

Table III.1: Ratios of peak intensities of (004) plane to (101) plane and (004) plane to (200) plane of the TiNT formed at different anodizing conditions.

Table III.2: gap states characteristics of TiNT electrodes after UV exposure.

Table V.1: carrier densities and flatband potentials evaluated from linear sections of the M-S plots of Figure V.6.

Table V.2: Circuit element parameters determined by fitting of the EIS spectra for α -Fe₂O₃/TiNT electrodes.

Table V.3: Circuit element parameters determined by fitting of the EIS spectra for **Pt**/TiNT and Pt/ α -Fe₂O₃/TiNT electrodes.

Table V.4: Photocurrent values of photoanodes in PEC water splitting from this and other works.

List of figures

Figure I.1: Crystal structures of (a) anatase, (b) rutile and (c) brookite.

Figure I.2: Equilibrium crystal shape of anatase TiO₂.

Figure I.3: (a) TiO₂ band structures for the rutile, anatase and brookite polymorphs and b) Total and partial DOSs of the three polymorphs of TiO₂.

Figure I.4: Different equilibrium situations at the n-SC/Electrolyte interface.

Figure I.5: n-SC/electrolyte interface behavior under voltage $U_{\text{appl}} = U_{\text{FB}}$ b) $U_{\text{appl}} > U_{\text{FB}}$ and c) $U_{\text{appl}} < U_{\text{FB}}$.

Figure I.6: n-type SC/electrolyte interface: a) in dark, b) under illumination and c) current vs. applied potential evolution in the dark and under illumination.

Figure I.7: The solar irradiance vs. wavelength and UV-Vis range of Solar spectrum. The absorption range of TiO₂ is also indicated.

Figure I.8: Single layer graphene, as a parent to other carbonaceous materials: 0D fullerenes, 1D nanotubes and 3D graphite.

Figure I.9: Schematic representation of three different heterojunctions between two semiconductors.

Figure I.10: Photo excited Semiconductor heterostructure.

Figure I.11: Diagrams of Different Mechanisms for LSPR-Enhanced Photoactivity of SCs.

Figure I.12: One of suggested mechanism of charge transfer in Ag/TiO₂ heterojunction under Visible light irradiation.

Figure I.13: Photocatalytic process mechanism.

Figure I.14: Fundamental principles of water splitting by photoelectrochemical cell.

Figure I.15: Ragone diagram that displays the power and energy densities of different energy storage devices.

Figure I.16: Supercapacitor cell.

Figure I.17: Classification of supercapacitors.

Figure I.18: Schematic representation of electrical double layer structures according to: (a) the Helmholtz Model (b) the Gouy-Chapman model, (c) the Stern model.

Figure II.1: Schematic set-up of anodization experiment.

Figure II.2: Schematic illustration of formation mechanism of a) TiO₂ compact layer and b) TiNT.

Figure II.3: Typical current–time ($j-t$) characteristics after a voltage step in the absence (----) and presence (____) of fluoride ions in the electrolyte.

Figure II.4: SEM photography.

Figure II.5: Illustration of Bragg's law for constructive interference.

Figure II.6: Schematic diagram of FTIR for the sample analysis process.

Figure II.7: Photoluminescence schematic. (a) promotion of the electron from VB to CB.

(b) The electrons cool down to the bottom of the conduction band. (c) The electron recombines with the hole resulting in the emission of light with energy $h\nu$.

Figure II.8: UV-Visible spectrometer (ISA-220) Photography, (b) aqueous solutions holder, (c) solids sample holder.

Figure II.9: A typical cyclic voltammogram showing anodic and cathodic peak currents.

Figure II.10: Electrochemical setup used for electrodeposition.

Figure II.11: a) Nyquit plot and b) Bode plot.

Figure II.12: Distinct shape of CV for (a) ideal and (b) pseudocapacitive type materials.

Figure II.13: GCD plots of: (a) an ideal supercapacitor, (b) and (c) non-ideal supercapacitors.

Figure II.14: Typical Nyquist plot representations for an EDLC, pseudocapacitive materials and battery.

Figure II.15: Scheme of the photoelectrochemical measurement setup.

Figure II.16: Schematic representation of the experimental set-up used for the photocatalytic tests.

Figure III. 1: SEM images of (a) TiNT grown at 50V, (b) TiNT grown at 50V/20V and (c) TiNT grown at 20V/50V in a solution containing Ethylene glycol + 0.27 M NH_4F + 2 wt% H_2O .

Figure III.2: XRD patterns of the different materials.

Figure III.3: M-S relationships of the different materials at a frequency of 1 kHz((a): 50V, (b): 20V/50V and (c): 50V/20V).

Figure III.4: Bode representation of TiNT electrodes after 3h of UV illumination ((a) TiNT grown at 50V (b) 20V/50V TiNT and (c) 50V/20V TiNT).

Figure III.5: Variations of the gap state capacitance (C_{ss}) as a function of the applied potential for TiNT electrodes after 3 hours UV illumination ((a): 50V, (b): 20V/50V and (c): 50V/20V).

Figure III.6: Photoluminescence spectra of the different materials.

Figure III.7: (a) UV-Vis spectra of TiNT electrodes and (b) the corresponding Tauc plots.

Figure III.8: (a) photocurrent densities of the electrodes under UV light, (b) photocurrent densities of the electrodes under visible light and (c) photocurrent transients under visible light, recorded at 0.2 V vs. Ag/AgCl.

Figure III. 9: Squared photocurrent versus electrode potential of (a) TiNT formed at 50V, (b) 20V/50V TiNT and (c) 50V/20V TiNT.

Figure III.10: (a) C/C_0 under UV light, (b) C/C_0 under visible light, (c) corresponding photocatalytic degradation efficiency under UV light and (d) corresponding photocatalytic degradation efficiency under visible light for the different photocatalysts.

Figure IV.1: Synthesis of graphene. (a) Photograph of pure graphite sheet (99.8%), (b) Photograph of black-marking pencil (5B), (c) Photograph show the condition after electrochemical exfoliation of pure graphite sheet in H₂SO₄ electrolyte, (d) Photograph show the condition after electrochemical exfoliation of 5B pencil core in H₂SO₄ electrolyte, (e) Photograph of dispersed graphene produced from pure graphite sheet in H₂SO₄ electrolyte, (f) Photograph of dispersed graphene produced from 5B pencil core in H₂SO₄ electrolyte.

Figure IV. 2: (a) Cyclic voltammograms of TiNT in solution containing 4 ml of dispersed Gr (from pure graphite sheet and 5B pencil core) and 35 ml of Na₂SO₄ (1M) and (b) Current transients recorded during electrodepositing.

Figure IV. 3: SEM images of Gr/TiNT and corresponding EDS spectra.

Figure IV. 4: (a) XRD patterns of TiNT and Gr/TiNT samples and (b) Enlarged XRD pattern around 25°.

Figure IV.5: Fourier transform infrared spectroscopy (FTIR) spectra of TiNT and Gr/TiNT.

Figure IV.6: (a) UV-visible absorption spectra of the different materials.

Figure IV. 7: Photoluminescence spectra of the different materials.

Figure IV. 8: (a) GCD curves of TiNT and Gr/TiNT at 30 μA/cm², (b) GCD curve of PGr)/TiNT at different current densities, (c) GCD curve of 5BGr/TiNT at different current densities and (d) Variation of areal specific capacitance at different discharge current densities.

Figure IV. 9: (a and b) Nyquist and Bode spectra at OCP of TiNT electrode, (c) Nyquist spectra of Gr/TiNT electrodes at OCP, (d) specific areal capacitance versus frequency response of Gr/TiNT electrodes and (e) phase angle versus frequency response of Gr/TiNT electrodes.

Figure IV. 10: Nyquist and Bode representations under different bias of: (a-b) TiNT, (c-d) PGr/TiNT and (e-f) 5BGr/TiNT.

Figure IV. 11: (a) interfacial resistance (R_{int}) evolution as a function of applied bias and (b) Warburg diffusion impedance evolution as a function of applied bias.

Figure IV. 12: M-S plots of (a) TiNT and (b) Gr/TiNT electrodes.

Figure IV. 13: CV curves of (a) PGr/TiNT electrode and (b) 5BGr/TiNT electrode at scan rates of 100, 250 and 500 mV/s. (c) Ragone plot of Gr/TiNT, (d) Capacitance retention behavior of Gr/TiNT electrodes for 1000 cycles. CV curves of (e) PGr/TiNT electrode and (f) 5BGr/TiNT electrode at a scan rate of 500 mV/s after extended time of 450 days.

Figure IV. 14: UV-vis absorption spectra of MB solution in the presence of: (a) TiNT, (b) PGr/TiNT and (c) 5BGr/TiNT, (e) C/C_0 under visible light and (f) corresponding photocatalytic degradation efficiency under visible light for the different photocatalysts.

Figure V.1: Cyclic voltammograms of: (a) TiNT electrode in a solution containing 0.05 M FeSO₄ and (b) α -Fe₂O₃/TiNT electrode in a solution containing 10 mM of K₂[PtCl₆].

Figure V.2: Current densities recorded at different deposition times during potentiostatic electrodeposition of: (a) FeOOH on TiNT, (b) Pt on TiNT and (c) Pt on α -Fe₂O₃.